HIGHLY SENSITIVE, MULTIPLEXED INTEGRATED PHOTONIC STRUCTURES FOR LAB-ON-A-CHIP SENSING

A Dissertation
Presented to
The Academic Faculty

by

Zhixuan Xia

In Partial Fulfillment
of the Requirements for the Degree
Doctor of Philosophy in the
School of Electrical and Computer Engineering

Georgia Institute of Technology
MAY 2015

COPYRIGHT©2015 BY Zhixuan Xia

HIGHLY SENSITIVE, MULTIPLEXED INTEGRATED PHOTONIC STRUCTURES FOR LAB-ON-A-CHIP SENSING

Approved by:

Dr. Ali Adibi, Advisor
School of Electrical and Computer Engineering
Georgia Institute of Technology

Dr. Wenshan Cai
School of Electrical and Computer Engineering
Georgia Institute of Technology

Dr. Gee-Kung Chang
School of Electrical and Computer Engineering
Georgia Institute of Technology

Dr. Kenneth Sandhage
School of Materials Science and Engineering
Georgia Institute of Technology

Dr. Stephen E. Ralph
School of Electrical and Computer Engineering
Georgia Institute of Technology

Date Approved: December 11, 2014

To my parents and wife Dong,

for their unconditional love and support

ACKNOWLEDGEMENTS

First and foremost, I wish to thank my advisor, Professor Ali Adibi, for his support and guidance during my study. Professor Adibi has always been a tremendous advisor. Not only is he intelligent and knowledgeable, Professor Adibi is also constantly willing to help and give his students the freedom to pursue their research interest.

I would also like to thank Professors Gee-kung Chang, Stephen Ralph, Kenneth Sandhage and Wenshan Cai for reviewing my thesis and serving on my PhD defense committee. They have been extremely supportive during the course of my study. Particularly, I am very fortunate to have the chance working closely with Professor Sandhage on the porous material related projects for the DARPA CIPhER program.

I am very grateful to Professor David Citrin, because of whom I could pursue my PhD degree at Georgia Tech.

I am indebted to Babak Momeni, Mohammad Soltani, and Siva Yegnanarayanan. They were a great help when I first joined the Photonic Research Group. Their knowledge, personality, and great devotion in academic research have set an excellent example for me to follow.

I deeply appreciate the fruitful collaboration with supportive colleagues in the School of Material Science and Engineering, including Stanly Davis, Ari Gordin, and Yunshu Zhang. Stan conducts the magnesiothermic reduction and we have failed countless times before making good samples that finally showed promising results. Ari has been working with me on many interesting projects, including the pSi film made by the porous alumina mask. Without his great contribution in the alumna anodization, this project would never be successful. Yunshu is the man behind the porous titania coating. He has always been very professional and responsive. It was a great pleasure working with all of them and I learned a lot from the experience.

I would like to express my gratitude to Ali Eftekhar, Murtaza Askari, Maysamreza Chamanzar, and Qing Li. I feel grateful to have worked closely with them on a variety of projects. They would always happily offer their hand whenever I needed help.

I am sincerely grateful to Dr. Gottfried in Institute for Electronics and Nanotechnology. He has taught me how to use the Inkjet printer and greatly helped me in the research on the multiplexed gas sensing.

My appreciation also goes to other former group members, including Chaoray Hsieh, Fengtao Wang, Ye Luo, Amir Atabaki, Saeed Mohammadi, Charles H. Camp, Ehsan S. Hossein, Ali Behrooz, and Payam Alipour. I also wish to thank all the current group members, including Farshid Ghasemmi, Reza Pourabolghasem, Majid Sodagar, Hossein Taheri, Amir H. Hosseinnia, Hesam Moradinejad, Hamed Shams Mousavi, Razi Dehghannasiri, Ahmad Usman, and many others. I have had a great time working in the Photonics Research Group.

I would like to thank my dearest friends in Atlanta. It is my honor to share those countless valuable moments with them, including Cheng Liu, Jing Xu, Tianyu Jiang, Min Na, Tianming Xu, Xiaohang Li, Bin Mu, Zhen Gao, Wei Jian, Claudio Estévez and many others.

Last but not least, this journey would be impossible without the love and support from my family. I am grateful to the endless sacrifice and encouragement from my parents, Zusen Xia and Bing Deng. My sincere appreciation goes to Dong Yang, my beloved wife, who has always been a great company, cheering me up during tough times. Her patience and love help me to come this far.

TABLE OF CONTENTS

LIST OF TABLES

LIST OF FIGURES

SUMMARY

The ever-lasting demand for knowing more information around human beings has led to the era of big data. Sensors are everywhere, monitoring, recording, and collecting all types of information for a variety of applications. Bio/chemical sensors, focusing on the information that is closely related to the health status of an individual, a family, a country, or even the whole world, prove to be of vital importance. An ideal sensing system needs to meet the requirement including excellent reliability, high performance, fast response time, low power consumption, low cost, and easy to work with. Therefore, a tremendous amount of effort has been devoted to developing necessary techniques and components enabling the miniaturization of otherwise bulky and expensive equipments. The focus of this Ph.D dissertation is to develop essential building blocks for the lab-on-a-chip optical sensing systems with high performance. In this work, the silicon-on-insulator platform is chosen because of its compatibility with the mature microelectronics industry for the great potential in terms of powerful data processing and massive production.

Despite the impressing progress in optical sensors based on the silicon photonic technologies, two constant challenges are larger sensitivity and better selectivity. To address the first issue, we resort to developing new processes to incorporate porous materials that are otherwise not available to the silicon photonic platform. By fabricating porous silicon using magnesiothermic reductions, we, for the first time, are able to integrate this interesting material with a large surface area to the silicon photonic platform. The demonstrated travelling-wave resonators with the porous silicon cladding have shown significant enhancement in the sensitivity. The process is then further optimized by replacing the thermal oxide with a flowable oxide for the magnesiothermic reduction. This optimization not only further improves the sensitivity, also simplifies the

fabrication process. A different approach of making porous silicon using porous anodized alumina membrane leads to better flexibility in controlling the pore size and porosity, such that the film can be tailored for various applications. Porous titania, another interesting material widely used in chemical sensors, is successfully integrated with silicon nitride operating at the infrared wavelength range. The travelling-wave resonator based sensors exhibit excellent sensitivity. Furthermore, this material platform can be readily extended to the visible wavelength range.

The problem of lacking selectivity is more severe in gas detection than in biosensing applications. To mitigate this issue, an array of integrated optical sensors are coated with different polymers, such that each incoming gas analyte has its own signature in the collective response matrix. The challenge of realizing such device is the selective polymer coating on a miniaturized sample with good accuracy and stability. Inkjet printing with an appropriate solvent is used to achieve this goal. A multiplexed gas sensor with four polymers has been demonstrated. It also includes on-chip references compensating for the adverse environmental effects.

On-chip spectral analysis is very critical for lab-on-a-chip sensing systems. For that matter, based on an array of microdonut resonators, we demonstrate an 81 channel microspectrometer on the silicon photonic platform. The key structure is the microdonut resonator realizing high quality factor and large free spectral range simultaneously. As a result, the demonstrated spectrometer leads to a high spectral resolution of 0.6 nm, and a large operating bandwidth of ~ 50 nm.

CHAPTER 1

INTRODUCTION

1.1 Lab-on-a-chip sensing

Small is good. In the area of sensing systems, small suggests compactness, light weight, minimal amount of sample analyte, and low power consumption. This is the motivation behind the trend of miniaturization of function modules for typical lab analysis, such as sample delivery and signal processing modules. In particular, a great deal of research has been dedicated to incorporating all the modules into a single chip for a Lab-on-a-chip (LOC) system. Because of its capability of performing rapid biological and chemical analysis on a single chip, LOC sensing is well suited for point-of-care testing for various military, industrial, environmental and medical applications [1-3]. For example, a hand held LOC test system has been operated aboard the International Space Station (ISS) [4] to monitor the ISS cabin surfaces for microbial contaminations, where testing results are obtained within 15 minutes without the need to return to earth.

A LOC system is comprised of two main modules: sample delivery module and signal processing module. The miniaturization of the sample delivery module is achieved by leveraging the advance in microfluidics [5]. Various sample delivery configurations allow for efficient sample transport, separation, mixing, and preconcentration on a chip-scale platform [6] for a very low amount of sample analyte (several picoliters). Versatile microfluidic configurations for sample manipulation have been realized in a variety of materials [7], including silicon, glass, elastomers, plastics, and paper. However, one remaining challenge is to develop a robust signal processing module that is scalable to cope with the elegant sample delivery architecture and, more importantly, maintain high

performance in terms of sensitivity, detection limit, and selectivity [2, 8]. The signal processing module in a LOC system are responsible for three major functions: signal generation, sensing, and signal detection (Figure 1.1). In this module, a certain type of signal (electrical, optical, acoustical, etc.) after generation is routed to pass through the sensor, picks up the information to test in the analyte, and is then received and decoded by the detector. Optical signal processing modules, fiber optical components in particular, have been very promising in biological and chemical analysis [9] because of their high sensitivity. However, the sensitivity of fiber optical components is dependent on the physical interaction length of the fiber probe [8]. Therefore, miniaturization of these components would inevitably degrade the performance.

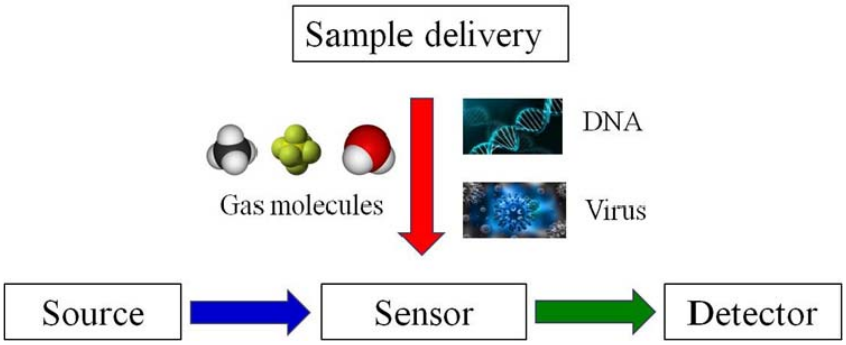

Figure 1.1 Components of a lab-on-a-chip system

On the other hand, chip-scale optical components including light sources [10, 11] and photodetectors [12, 13] have been enabled by recent advances in optoelectronics and semiconductor fabrication technology. Additionally, a variety of microresonators have been proposed for on-chip sensing on a silicon-on-insulator (SOI) substrate [14, 15]. These miniaturized structures perform as sensors to convert target analyte information (binding activity, existence, concentration, etc.) to the optical signal by refractive index detection. Because of the high quality factor (Q factor) of these devices, high sensing

performance is not sacrificed as the footprint decreases. Therefore, there is a great potential in realizing a LOC system with these photonic structures.

The research work in this thesis is to develop essential building blocks for a photonic LOC system, as is illustrated in Figure 1.2. Compact, high sensitivity and multiplexed sensors based on integrated photonic microresonators are thoroughly investigated. To achieve high sensitivity, we develop several processes to incorporate a variety of thin porous layers onto conventional photonic microresonators (silicon or silicon nitride). The additional porous material cladding provides high surface area, and thus increases the sensitivity. Despite of the rough porous material cladding, the proposed structures are still obtained with high Q factor and thus excellent sensing performance is attained. Another important figure of merit is selectivity. Because of the lack of a lock-and-key mechanism, it is very challenging to design a gas sensor that can recognize a certain analyte among a complex background. In this work, by coating an array of microresonators with various polymers, I propose and study a compact, sensitive, multiplexed sensor that enables selective gas sensing. The third task is to develop a compact on-chip spectrometer for the signal detection module. Formed by a large scale array of microresonators, a spectrometer with high resolution and large bandwidth is demonstrated.

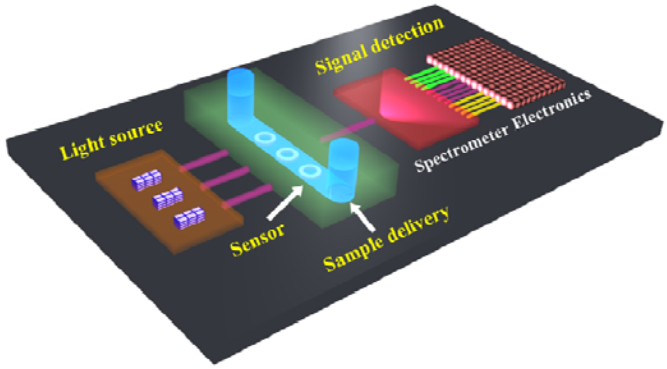

Figure 1.2 Schematic of a photonic lab-on-chip sensing system

1.2 Refractive index sensing

The optical sensors investigated in this thesis are based on resonant refractive index sensing. Refractive index sensing based optical sensors have attracted a lot of research recently [16, 17]. By using optical microresonators with a small footprint, these sensors convert target analyte information to the shift of effective refractive index experienced by the light propagating in the resonators, whose resonance wavelength varies accordingly [17] (see Figure 1.3). Compared to conventional fluorescence based optical sensors [18, 19], the refractive index sensing leads to label free detection and thus avoids the need of cumbersome sample preparation by experienced technicians. So far, optical microresonators have been realized by various configurations, including microspheres [20-22], microtoroids [23, 24], microdisks [25-27], microrings [3, 28-32], and racetracks [33, 34]. They are made by silicon (Si), silicon nitride (Si_xN_y), and silicon dioxide (SiO_2) with high refractive index contrast to enable compactness when they are integrated with other function modules on the same chip. More importantly, their fabrication processes are compatible with the mature semiconductor technologies and hence are very suitable for high-yield volume production [35]. Among the aforementioned configurations, optical resonators based on microrings and racetracks have gained the most interest in sensing applications. The reason is that they are planar structures that operate on a single radial mode, which makes the integration and light coupling much more straightforward than the other configurations.

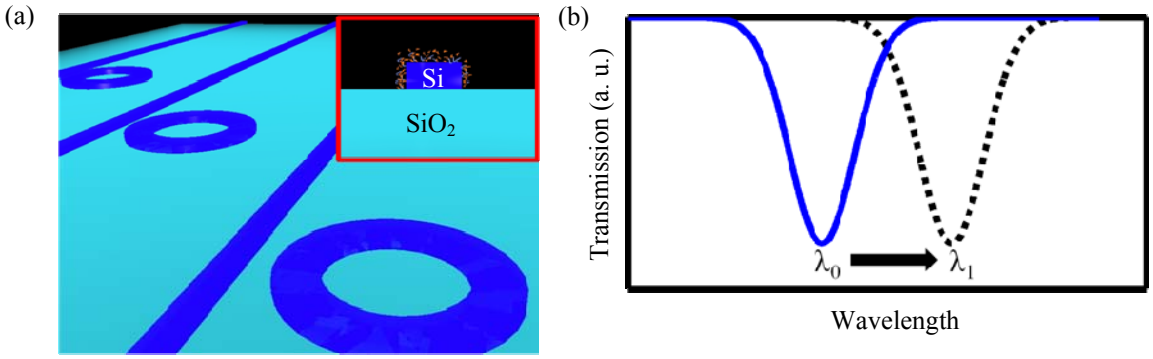

Figure 1.3.(a) Schematic of an array of SOI microring resonators coupled with bus waveguides for light input and output. The sensor operates based on the detection of the analytes adsorbed onto the surface of the optical waveguides (inset); (b) Adsorbed analytes causes a redshift in the resonance wavelength from λ_0 to λ_1.

The optical microresonator sensors are characterized by three important terms: sensitivity, detection limit, and selectivity. For an optical microresonator sensor based on the refractive index sensing, sensitivity is the shift of the resonance wavelength per a unit change in the cladding refractive index [16]. Detection limit refers to the minimal change in the cladding refractive index that can be reliably detected [17]. It is determined by the sensitivity and the spectral resolution of the detection system. Generally, higher signal-to-noise (SNR) and larger Q factor of a microresonator lead to a better spectral resolution. Recently, with proper interrogation configuration and sensor design, spectral resolutions of ~ 0.06 pm [36] and ~ 0.2 pm [30] have been demonstrated in microring resonators with Q factors of 14,000 and 40,000, respectively. The Selectivity is the capability of a sensor to reliably recognize a certain analyte among a complex background. It is highly dependent on the chemical and biological properties of the receptor used in the sensor [15, 37].

To increase the sensitivity of an optical microresonator sensor, one approach is to enhance the light-matter interaction by optimizing the waveguide structure. Optimal field

distribution can be obtained by systematically investigate the geometry of the waveguide and the light polarization [38]. The recently demonstrated slot waveguide, which confines the light and incoming analytes in the same area, has shown great promises in achieving high sensitivity [26, 28, 39, 40]. However, the Q factors of the slot waveguide based microresonators are limited (the highest reported Q factor from a slot microring resonator is ~7,000 [26]), making it challenging to achieve a high spectral resolution.

Since biomolecular interactions are limited to the surface of the waveguide, it is advantageous to use a waveguide structure possessing a large surface area to enhance the light-matter interaction [41]. Porous silicon (pSi) has been a promising candidate owing to its large internal surface area, remarkable morphological properties, and well-developed surface chemistry for label free detection of deoxyribonucleic acid (DNA) [42], enzyme [43], virus [44], bacteria [45], and gas [46]. However, starting from a single crystalline silicon wafer, current anodization method of making pSi leads to a solely slab-type structure with cylindrical pores [47]. Although a variety of sophisticated multilayer configurations [48] have been realized by carefully tuning fabrication parameters, the low refractive index contrast between each layer makes it very challenging for the integration with an on-chip photonic platform for other functionalities and further signal processing. More importantly, the anodized pSi optical microresonators have exhibited modest Q factors [49-52]. So far, the largest Q factor is 1,530 for a conventional multilayer resonator [52] and 3,380 with a free-standing resonator [50]. Moreover, there is a trade-off between the Q factor and the accessibility of anodized pSi multilayer resonator for sensing. High Q factor multilayer resonator requires a larger number of high/low

refractive index bilayers and thus it is challenging for the analyte to penetrate into the center active layer and be detected [51].

A shape-preserving, magnesiothermic reduction based process has recently been demonstrated to selectively convert thin silicon dioxide films into uniform pSi films possessing three-dimensionally-interconnected pores [53]. This process can be thermodynamically designed to allow for reaction only with silicon dioxide [54, 55] (Michael Haluska, Stan Davis, Ken Sandhage). The shape and size of the pSi structure is predefined by the silicon dioxide template, which can be made with standard semiconductor fabrication techniques. Therefore, this approach enables pSi film on a SOI platform that can accommodate on-chip optical resonators and other function modules for signal generation and detection. In addition, the thickness of the pSi film can be precisely controlled via adjustment of the silicon dioxide film thickness (tailorable to within 1 nm by thermal oxidation of silicon [56]). The large internal specific surface area (>500 m^2/g) associated with uniformly-distributed, micro/mesopores in pSi formed by this process provides for greater adsorption of small analytes for enhanced detection sensitivity, while the thin, uniform nature of the pSi films allows for low optical loss. Consequently, there is a great potential to integrate such magnesiothermically formed pSi with aforementioned microresonators to enable highly sensitive on-chip optical sensors. We will show in the following chapters on how this integration could be made and the corresponding benefits, as well as how to extend this idea to other material platforms.

In addition to the sensitivity, the selectivity of an on-chip optical sensor is of vital importance in the applications of biological and chemical sensing. For biological sensing, selectivity is achieved by using the 'lock and key' mechanism in the biomolecular

interactions [37]. With adequate surface modification, microresonator coated with biotins has shown a much greater response to avidins than to bovine serum albumin (BSA) [33]. Moreover, by using a large array of microring resonators, each of which is coated with a different biomolecular receptor, researchers have been able to demonstrate the multiplexed detection of DNAs [20], RNAs [57], antibodies [58], and protein biomarkers [59]. However, the target analyte in this work is volatile organic compounds (VOCs), strategy does not apply to gas sensing, particularly in detecting volatile organic compounds (VOC), which is an important gas of interest in biomedical and environmental applications [60]. There are two limitations: 1) some VOC analytes (e.g. hydrocarbons) are weakly interactive and do not have a specific molecule to pair with; and 2) even if a strong and specific binding exists, it usually means slow recovery and irreversibility, and thus makes it very challenging to enable rapid and real-time monitoring of the incoming gas analytes. Therefore, a widely accepted strategy is to use an array of cross-reactive sensing elements coated by polymer receptors with various properties [61-63]. Compared to another very common receptor, i.e., metal oxides [64-66], polymers are more advantageous in the sense that: 1) they are more flexible and can be readily engineered to work for a specific sensing application; 2) unlike some metal oxide gas sensors, no elevated operating temperature is needed for polymer coated sensors; and thus, improved reliability and lower power consumption is ensured.

To implement the array of cross-reactive sensing microresonators, one needs to achieve selective coating of polymer receptors with good positioning accuracy. A drop-on-demand (DOD), non-contact inkjet printing method can be used [67]. Inkjet printing allows for highly precise rapid deposition of small volume droplets down to ~ 1 picoliter

depending on the size of the orifice [67]. It is a versatile method that can be applied to a variety of solutions (including organic solvents) and substrates such as silicon, glass, plastic, etc.. Therefore, a variety of polymer receptors can be dissolved in compatible solvents and then delivered to the target microresonators. Drops containing polymer receptors are released from the printhead by applying a pressure pulse after moving the head to a desired location. This method exhibits very high positioning accuracy (a few μm).

The signal of interest in the aforementioned microresonators is the resonance wavelength. Therefore, an integrated spectrometer is needed to perform on-chip spectral analysis for the LOC sensing system. Motivated by this demand, there has been significant progress in the realization of integrated microspectrometers in different configurations such as arrayed-waveguide gratings [68, 69], grating spectrometers [70-72], superprism-based spectrometers [73, 74], and the diffractive grating spectrometer combined with the thermally tunable microring resonators [75]. However, the main challenge of the integrated spectrometers that rely on dispersive components is the trade-off between the spectral resolution and the size of the structure [76]. To break such trade-off, a filter array with Fabry-Perot cavities has been proposed to provide high spectral resolution (1.7 – 3.8 nm) in the near infrared region [77]. In this approach, different spectral components of the incoming signal are individually captured by their corresponding filters with a varying vertical cavity length obtained by multiple film deposition steps. An array of detectors is used to measure the output of all filtered spectral component simultaneously and sent the data to an electronic processing device in real time. However, the Fabry-Perot filter array suffers from the complexity of fabricating

highly reflective and parallel mirrors with a series of different cavity lengths, and its resolution is limited by the available reflectance of the cavity mirrors. In this proposal, I will address the trade-off issue with an array of miniaturized microdonut resonators that exhibit large FSR and high Q factor [78], to achieve a large bandwidth and high spectral resolution simultaneously.

1.3 Thesis organization

The remainder of this thesis contains four chapters. They are organized as follows.

Chapter 2 is dedicated to the techniques in improving device sensitivity by incorporating porous materials to conventional silicon or silicon nitride (SiN) platforms. Specifically, we propose and demonstrate porous silicon (pSi) clad microresonators on SOI platform and porous titania on the silicon nitride substrate. Integrated sensors are demonstrated with superior performance over conventional ones. Process optimizations and theoretical models are also presented.

Chapter 3 develops a process to develop a miniaturized, multiplexed gas sensor. The key challenge in this process is the ability to achieve selective polymer drop coating. By using a drop-on-demand inkjet printer, a reliable polymer coating process is realized and the multiplexed optical sensor for VOC detection is demonstrated.

chapter 4 deals with the challenge of developing a high resolution and large bandwidth spectrometer that can be realized on an SOI chip.

Chapter 5 summarizes the main contribution of this research work and discusses potential opportunities in the future.

CHAPTER 2

POROUS-MATERIAL-CLAD MICRORESONATORS

This chapter focuses on the sensitivity enhancement by introducing porous materials in the cladding for integrated microresonators. Three types of materials are discussed in this chapter. Section 2.1 deals with pSi films made via the magnesiothermic reduction. Section 2.2 presents the work on making pSi films with a porous alumina mask layer that can be compatible with the SOI platform. In Section 2.3, we demonstrate porous titania clad integrated microresonators on silicon nitride platform.

2.1 pSi-clad microresonators based on magnesiothermic reduction

2.1.1 motivation

pSi films for optical devices have been extensively studied for a wide applications including light emitting diodes, photodetectors, optical switches, lithium ion batteries, and label-free optical detection of numerous analytes. Conventionally, pSi films are fabricated by anodization of single crystal silicon wafers, leading to films possessing two-dimensional, cylindrical mesopores with thicknesses controlled by the anodization kinetics of doped silicon in HF-bearing solutions [79]. The use of applied currents with HF-bearing solutions makes integration with silicon-on-insulator platforms difficult. As is briefly stated in the previous sections, the anodized pSi optical microcavities to date have exhibited modest quality factors (Q-factors of ~ 1,530 for a multilayer resonator). Further, the tradeoff between the Q-factors and accessibility of pSi multilayer resonators for sensing applications needs to be addressed. A high Q-factor multilayer resonator requires a larger number of high/low refractive index bilayers. In such structures, it is

challenging for the incomings analyte to penetrate into the center defective layer and be detected.

In this work, we demonstrate a novel fabrication approach of integrating pSi with SOI microresonators using a modified magnesiothermic reduction process [53].

2.1.2 Magnesiothermic reduction

The motivation of using the magnesiothermic reduction based process to convert a silicon dioxide template into a pSi structure is that this conversion preserve the shape of

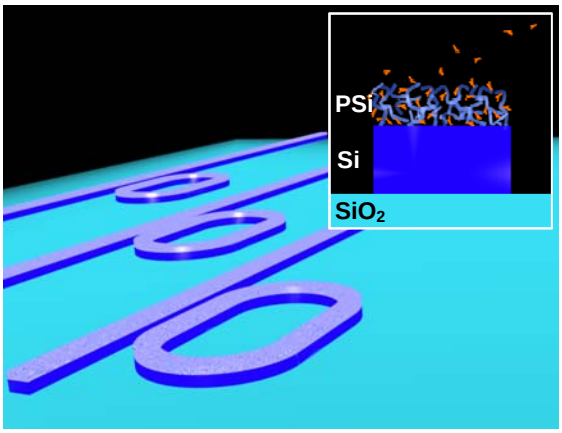

Figure 2.1 Schematic of a pSi-clad SOI travelling-wave resonator. A thin, uniform layer of pSi is generated via selective reactive conversion of a thin silica film present on dense silicon. (Inset) Cross section illustrating a pSi top cladding, possessing a three-dimensionally-interconnected pore network, to facilitate the adsorption and detection of analytes on a SOI waveguide.

the silicon dioxide template[53, 80]. Therefore, the geometric properties of the final pSi structure can be well controlled by tuning the silicon dioxide template. The magnesiothermic reduction was conducted (S. Davis, Sandhage group) by exposing the silicon dioxide films to pure magnesium gas at an elevated temperature ($\geq$ 650^{o}C). However, three reactions may occur:

$$2Mg(g) + SiO_2(s) \rightarrow 2MgO(s) + Si(s) \quad (2\text{-}1)$$

$$2Mg(g) + Si(s) \rightarrow Mg_2Si(s) \quad (2\text{-}2)$$

$$xMg(g) + Mg_2Si(s) \rightarrow Mg_{2+x}Si(l) \quad (2\text{-}3)$$

While reaction (2-1) leads to co-continuous mixtures of nanocrystalline MgO(s) and Si(s) at 650-850^{o}C, reactions (2-2) and (2-3) yields unwanted conversion of the silicon product of reaction (2-1), or the underlying silicon substrate, into Mg_2Si(s) or $Mg_{2+x}Si$(l). To address this issue, the magnesium partial pressure can be reduced by using Mg_2Si(s) itself as the gas source to minimize the undesired reactions (M. Haluska, KH. Sandhage).

To test this selective reaction process, SOI wafers were thermally oxidized at 1000^{o}C, followed by wet etching with buffered oxide etcher to produce silicon dioxide layers. The oxidized wafers were then sealed with Mg_2Si powder inside iron ampoules and heated to 750^{o}C for 1 h to yield MgO/Si-coated SOI samples (S. Davis, Sandhage group). After the conversion, the MgO/Si-coated SOI samples were immersed in 1 N HCl for 20 mins to allow for selective MgO

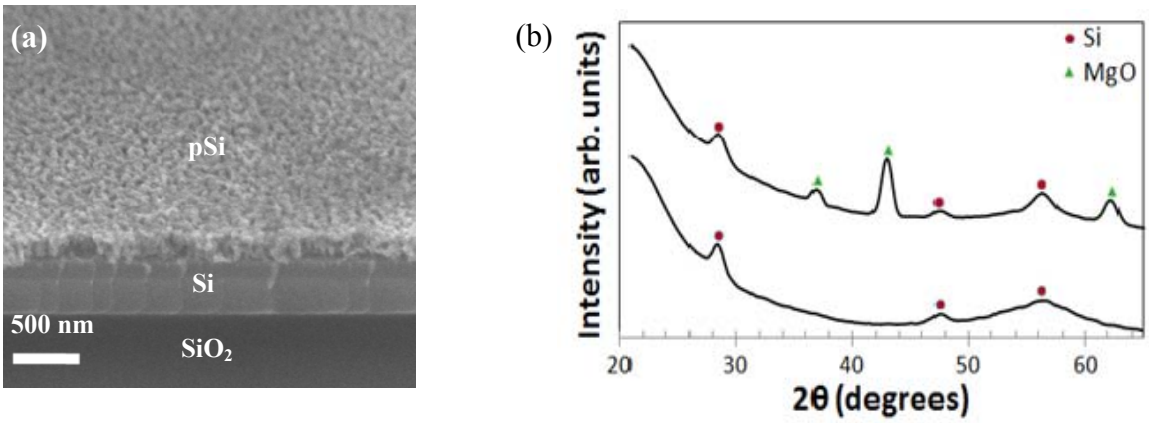

Figure 2.2 (a) SEM image of a particle-free pSi layer on an SOI substrate when the YSZ cloth is adopted; (b) Grazing incidence X-ray diffraction (GIXRD) analysis of converted blanked silica films on SOI: (top) MgO/Si film and (bottom) pSi film after selective MgO dissolution. (Provided by S. Davis)

Figure 2.2 (a) is a secondary electron (SE) image showing uniform, particle-free pSi layer comprised of co-continuous networks of mesopores and fine (< 20 nm) Si filaments. Figure 2.2(b) depicts X-ray diffraction analyses of the reacted specimens revealed diffraction peaks for MgO and Si, but not Mg_2Si. As is seen from Figure 2.3(a) and (b), the fabricated pSi possess three dimensional interconnected pores.

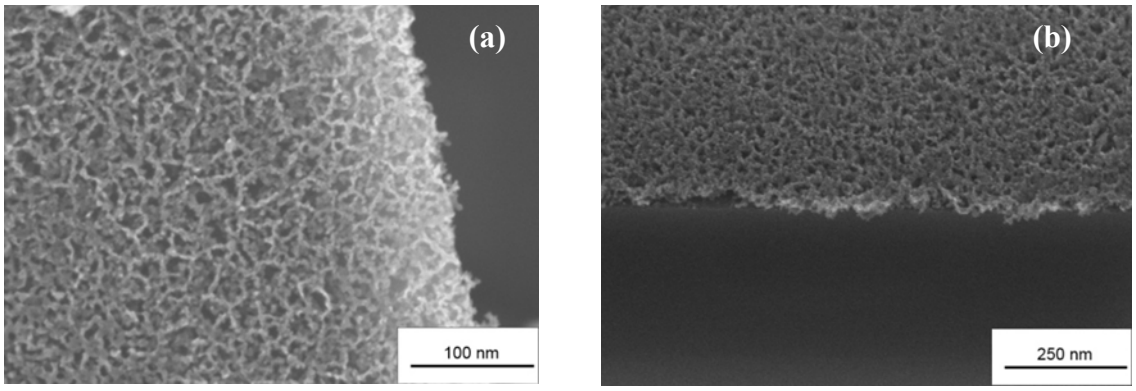

Figure 2.3 SEM images of cleaved pSi films dissolution to yield porous, nanocrystalline silicon films on the SOI substrates.

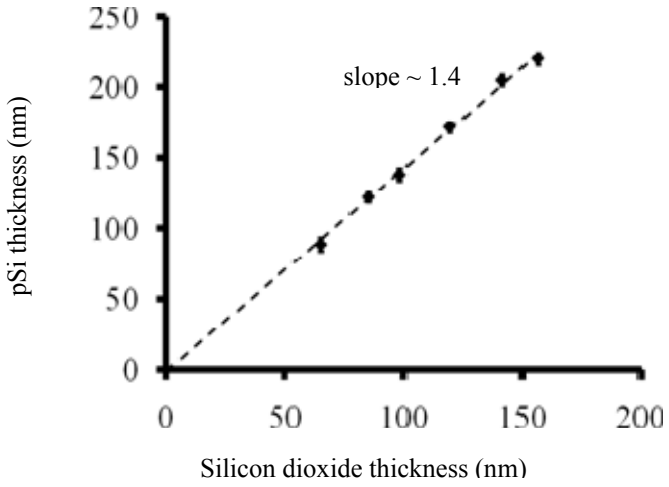

Figure 2.4 Thickness of magnesiothermically-formed pSi film versus the initial silica film thickness.

Samples with different initial top silicon dioxide thicknesses were converted and the

corresponding pSi layer thicknesses are plotted in Figure 2.4. The thickness of the silicon dioxide is determined by an Ellipsometer (Woollam M2000), while that of the final pSi film is by an SEM (Zeiss Ultra 60). The final pSi layers were found to be ~1.4 times thicker than the starting oxide layers, which is consistent with the 1.38-fold increase in solid volume associated with reaction (2-1) (The combined volume of 2 moles of MgO (V_m[MgO] = 11.25 cm^3/mol) and 1 mole of Si (V_m[Si] = 12.06 cm^3/mol) is 1.38 times larger than the volume of 1 mole of thermally-grown amorphous SiO_2 (for silicon dioxide formed by silicon oxidation at 1000°C, V_m[a-SiO_2] = 25.0 cm^3/mol). The well-behaved linear correlation observed in Fig. 2.4 allows for precise control of the pSi thickness by tailoring of the starting SiO_2 film thickness.

2.1.3 Fabrication process

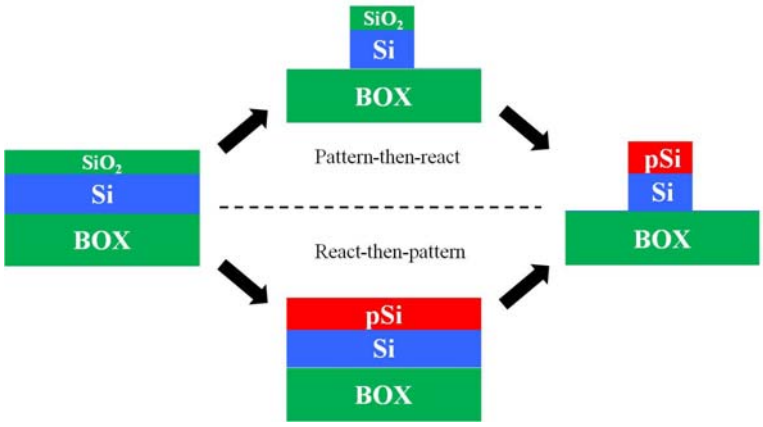

Figure 2.5 Schematics of the two approaches of fabricating pSi-clad SOI microresonators

Two methods have been studied to realize microresonators with pSi cladding: "pattern-then-react" and "react-then-pattern". As is illustrated in Figure 2.5, both methods start from an SOI wafer with a silicon dioxide layer on top. In the first approach, the

syntheses of pSi-clad SOI microresonators are conducted by first preparing SOI microresonators capped with a thin silicon dioxide strip cladding, followed by the magnesiothermic reduction to convert the silicon dioxide strip into a porous silicon strip on top of the silicon waveguide. On the other hand, the "react-then-pattern" method first converts the silicon dioxide layer into a thin pSi film, followed by microfabrication processes to pattern the device.

The "pattern-then-react" method is simple. However, after the conversion, appreciable macrocracking were observed in the trenches (Figure 2.6(b)), which was attributed to the reaction of the magnesium with the underlying thick buried oxide layer. To address this issue, a Si pedestal layer was used to protect the underneath silicon dioxide layer. Figure 2.6(c) is the SEM image of the cross section of a waveguide with ~ 140 nm thermal oxide

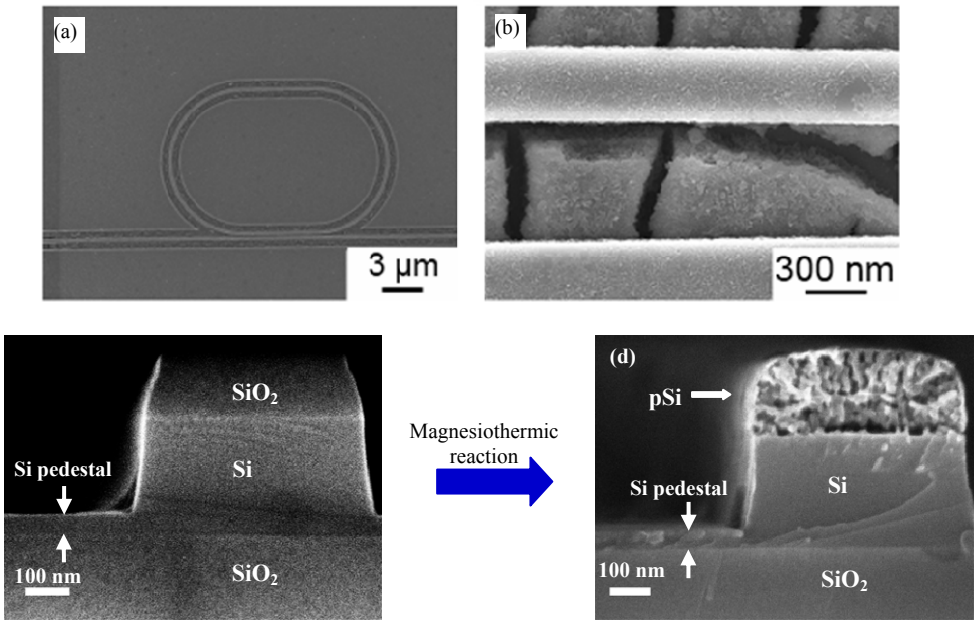

Figure 2.6 (a) Low-magnification and (b) high-magnification top-down SEM images of a device prepared by the "pattern-then-react" method. (Provided by S. Davis, Sandhage group) (c) SEM image of a strip SOI waveguide with a ~ 140 nm thick silicon dioxide cladding on top before magnesiothermic reaction. A pedestal layer of ~ 40 nm in the trench was used to avoid reaction and cracking of the buried silicon dioxide layer. (d) SEM image of the reactively-formed pSi cladding of ~ 200 nm thickness on the SOI waveguide.

strip on top. The thickness of the silicon waveguide is ~ 250 nm, with a 40 nm thick pedestal layer for the protection of the silicon dioxide underneath. After the conversion, as is shown in Figure 2.6 (d), the silicon dioxide on top was successfully converted to a pSi strip cladding. The thickness of the strip was measured to be ~ 200 nm, which confirms the expansion factor of ~ 1.4 that was mentioned above. As was expected, the underneath silicon dioxide remained intact during the conversion thanks to the silicon pedestal on top. However, the optical transmission through the crack-free pSi-clad silicon microresonators was very poor. This is possibly due to donor doping of silicon with magnesium [81] that significantly increases the optical loss in the waveguide.

The failure of the first approach leads to the "react-then-pattern" method, which

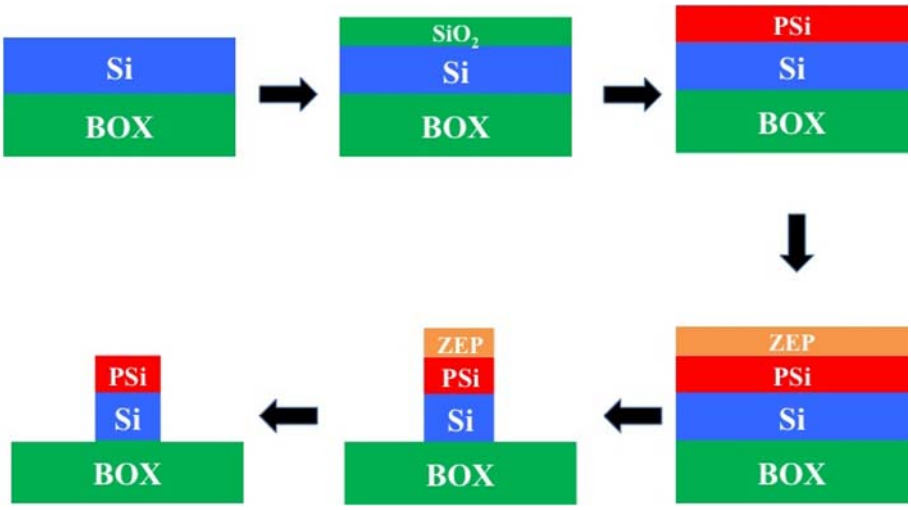

Figure 2.7. Fabrication flow of "react-then-pattern" method for pSi-clad microresonators

avoids direct exposure of patterned silicon microresonators to Mg(g). Unpatterned SOI substrates with predefined silicon dioxide thickness were magnesiothermically converted into MgO/Si films. After selective MgO dissolution, the resulting pSi-clad SOI substrates

were patterned into pSi-clad resonators. The complete fabrication flow is shown in Figure 2.7 and described as follows.

Step 1: Define the silicon dioxide layer on top of an SOI piece

Silicon dioxide is thermally grown by dry oxidation at an elevated temperature of 1000°C using Tystar Furnace. Buffer oxide etchant (BOE, NH4F:HF=6:1) is adopted to reduce the silicon dioxide to a desired thickness. The etch rate of silicon dioxide at room temperature is ~ 102 nm/min.

Step 2: Conversion from silicon dioxide to pSi

The cleanliness of the sample proves to be extremely important to minimize the contamination of the converted sample. Prior to the conversion, the samples were rinsed by acetone, methanol, and isopropanol (IPA) in an ultrasonic bath (5 mins each).

The cleaned samples are then sealed with Mg_2Si powder inside iron ampoules and heated to 750 ^oC for 1 hour to yield MgO/Si-coated SOI samples. After the conversion, the MgO/Si-coated SOI samples are immersed in 1 N HCl for 20 mins to allow for selective MgO dissolution to yield porous, nanocrystalline silicon films on the SOI substrates. Figure 2.8 shows the reaction chamber formed by a sealed iron ampoule. It is worth noted that a yttria-stabilized zirconia (YSZ) cloth is needed to avoid physical contact of the sample with the Mg_2Si powder, while allowing for Mg(g) migration from the Mg_2Si powder through the porous cloth to the SiO_2-coated SOI substrate at 750^oC. Otherwise the pervasive cube-shaped Mg_2Si particles would bond onto SOI wafers and form defects that introduces significant optical loss. (Protocol developed and conducted by S. Davis, Sandhage group)

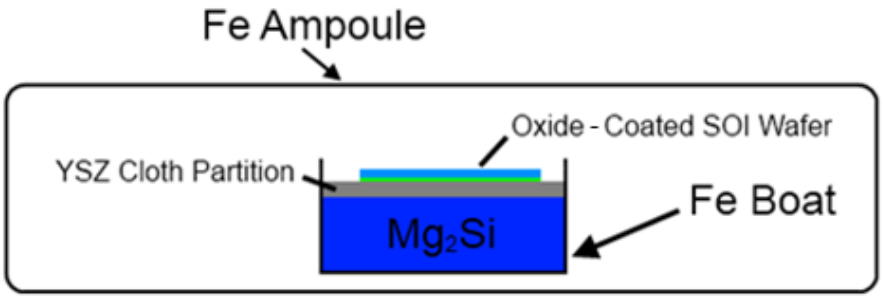

Figure 2.8. Schematic illustration of the experimental reaction setup used for uniform conversion of the SiO_2 layer on SOI substrates into pSi. (Provided by S. Davis, Sandhage group)

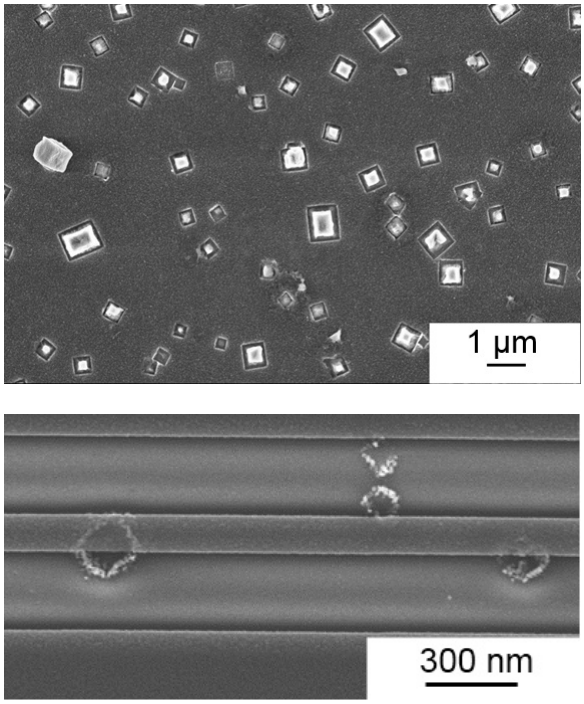

Figure 2.9 Cube-shaped defects formed in the pSi generated without use of the YSZ barrier to physically separate the Mg_2Si powder from the SiO_2-coated SOI substrate. (Top) SEM image of pervasive cube-shaped Mg_2Si particles diffusion bonded onto SOI wafers after magnesiothermic reaction at 750^{o}C for 1 h (Provided by S. Davis, Sandhage group), and (bottom) cubic (light scattering) defects (pits) retained after selective dissolution of the adhering Mg_2Si, along with MgO, from a react-then-patterned waveguide.

Step 3: Device pattern writing with lithography

Electron beam lithography (JEOL JBX-9300) is employed to pattern the pSi-clad SOI sample using ZEP 520 as the resist with a dosage of 260 C/cm^2. The spin speed for ZEP 520 is 700 RPM, leading to a thickness of around 730 nm measured by a Nanospec reflectometer (Nanospec3000). After the exposure, the sample is developed by 2 mins immersion in Amyl Acetate followed by 30 secs rinse under IPA.

Step 4: Pattern transfer by dry etching

Etching is conducted by plasma-therm ICP under the condition as follows: Cl_2 – 50 sccm, pressure – 5 mtorr, platen/coil power – 75/125 W. The DC bias is ~ 500 V after the plasma stabilized. Etch rate for silicon and pSi are typically measured to be ~ 75 nm/min and 82 nm/min, respectively. Etch selectivity for ZEP 520A is ~ 0.46, i.e., 100 nm of ZEP 520 is needed to etch 46 nm of silicon.

Step 5: Resist Removal

To remove the remaining ZEP 520A, the sample is soaked in 1165 remover (n-methyl pyrrolidinone) at 80 ^{o}C for 2 hours. An extra rinse by acetone, methanol, and IPA is needed to ensure complete removal.

Figure 2.10 is a react-then-patterned pSi-clad SOI racetrack microresonator, consisting of a ~ 120 nm thick pSi cladding on a ~520 nm wide by ~ 230 nm tall silicon waveguide. The radius and the length of the straight portion are both 10 μm. This geometry was chosen to ensure single-mode operation under transverse electric (TE) polarization (electric field in the device plane) at 1550 nm, while maintaining a reasonably high Q factor and wide FSR.

For this specific design, the fabrication started from an SOI wafer comprised of a 300 nm silicon device layer sitting on a 1 μm thick buried oxide. Dry thermal oxidation was conducted at 1000°C for 6 h to generate a 160 nm thick silicon dioxide cladding on top of a 230 nm thick silicon layer. Wet etching was conducted to reduce the thickness of the surface silicon dioxide layer to 85 nm. After the conversion, device pattern writing and transfer were performed as described above.

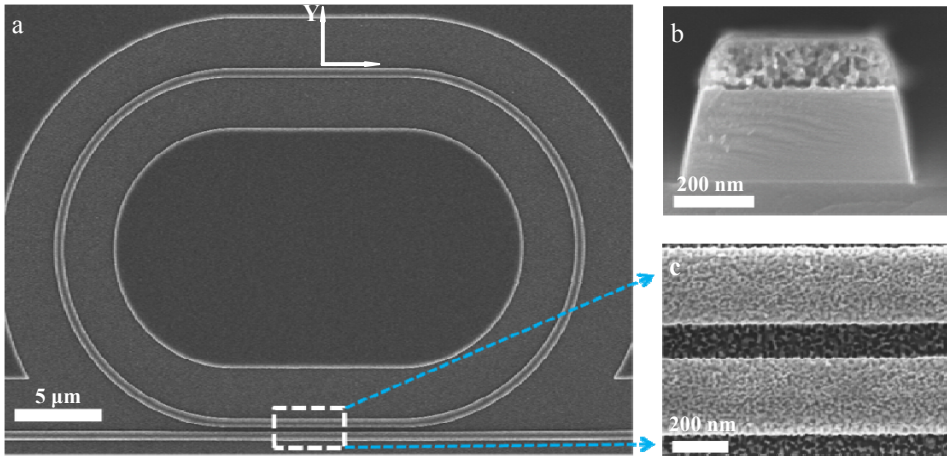

Figure 2.10 pSi-clad SOI racetrack resonator generated by the react-then-pattern method. (a) Top-down SEM image of the racetrack resonator. (b) SEM image of a cross-section of the pSi-clad SOI waveguide. (c) Top-down SEM image of the coupling region of the racetrack resonator and the waveguide.

After thorough cleaning, the device is optically characterized with a tunable laser (81640A, Agilent Technologies) as the light source. A pair of tapered fibers was employed to couple light into and out of the device. The output signal was detected by an InGaAs photodetector (Thorlabs PDB 150C). A thermal stage (Thorlabs TED 200C) was used to keep the temperature fixed at 24 °C during the analyses. The data was recorded and saved for later processing through a Labview interface. An illustration of the characterization setup is shown in Figure 2.11.

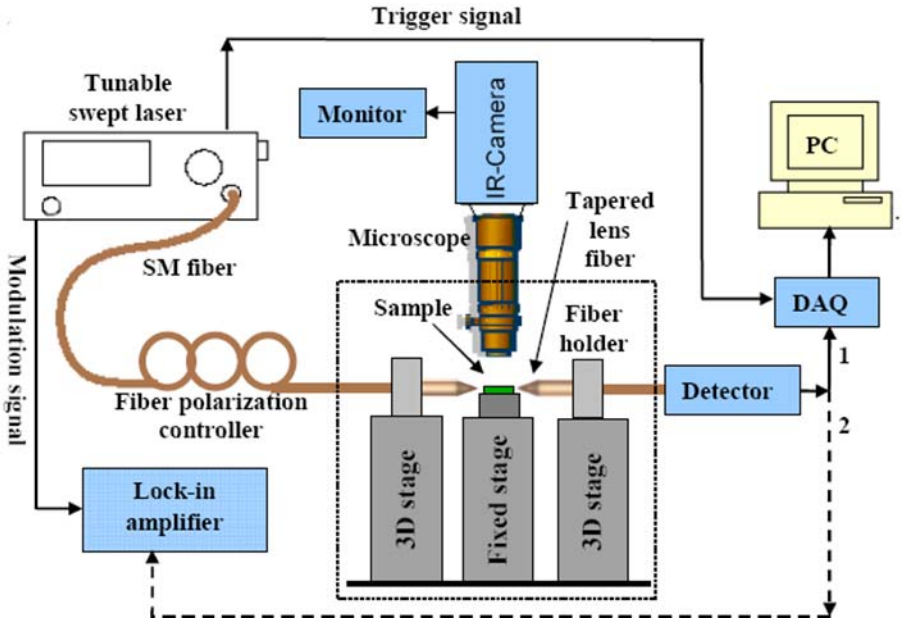

Figure 2.11. Fiber-based Characterization setup for the pSi-clad microring resonators

The TE transmission spectra of a reference racetrack resonator lacking pSi (but otherwise identical to the pSi-bearing resonator) and a pSi-clad racetrack resonator and are shown in Figure 2.12(a) and Figure 2.12 (b), respectively. The full-width-at-half-maximum (FWHM) of the resonance at 1550 nm for the pSi-clad and reference resonators were ~ 70 pm and ~ 65 pm, respectively, which corresponded to loaded Q-factors of 22,000 and 24,000, respectively. FSR values of the pSi-clad and reference resonators were 6.84 nm and 6.67 nm, respectively.

Comparison of the measured FSR value for the pSi-clad resonator with a simulation using a three-dimensional finite element method yielded an equivalent refractive index value for the pSi layer of ~1.7 at 1550 nm. This value was also obtained by using Bruggeman's effective medium model with the assumption that the pSi cladding possessed a porosity of 65.1 vol% (i.e., the volume percentage of MgO in the MgO/Si product of reaction (2-1) prior to selective MgO dissolution). The Q-factor and FSR

values for the pSi-clad microresonators were quite reproducible. A total of nine pSi-clad racetrack resonators, generated in three separate fabrication runs with three structures formed on each SOI substrate, achieved loaded Q-factors of 22,770 ± 2,483 (Figure 2.13) and FSR values of 6.832 ± 0.017 nm.

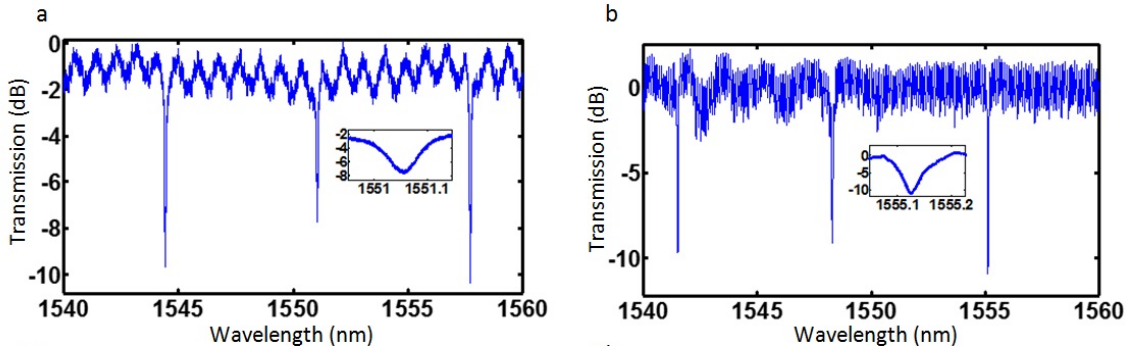

Figure 2.12. Optical characterization of the reference resonator and pSi cladded resonator under TE polarization. (a) Transmission spectrum of the reference resonator. (Inset) close-up of the resonance dip around 1550 nm, with a measured FWHM of ~ 65 pm. (b) Transmission spectrum of the pSi cladded resonator. (Inset) close-up of the resonance dip around 1550 nm, with a measured FWHM of ~ 70 pm.

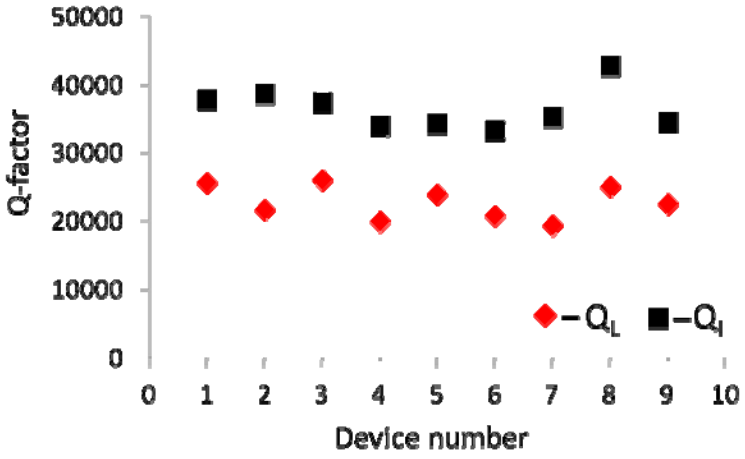

Figure 2.13. Q-factors of the pSi-clad SOI travelling-wave resonators. Loaded Q-factors, Q_L, of pSi-clad resonators in different fabrication runs were consistently around 22,770 in the 1550 nm wavelength region. The intrinsic Q-factors, Q_I, were extracted and found to be centered about 36,000, corresponding to a propagation loss of ~ 19.4 dB/cm at 1550 nm.

2.1.4 Biomolecule detection

To quantitatively evaluate the enhanced analyte adsorption resulting from the increased surface area of the pSi cladding, (3-aminopropyl)triethoxysilane (APTES) [82-84] monolayers were deposited on pSi-bearing and reference resonators. Thermal oxidization at 550 °C for 3 min was first conducted to create a thin oxide layer on the porous silicon internal surfaces to promote covalent attachment of 3-aminopropyltriethoxysilane (99%, Sigma Aldrich). The samples were then soaked in a mixture comprised of 4 parts (by volume) APTES, 46 parts methanol, and 50 parts deionized water (DI water) for 20 min at room temperature. After such incubation, the samples were sequentially washed in methanol (≥ 99.9%) and DI water before drying with flowing N_2. Before the characterization, the samples were then heated at 100 °C for 10 min. Consistent with previous reports using the same well-characterized monolayer deposition protocol and using a reported refractive index of 1.46 for APTES [82, 84], ellipsometric analysis indicated that the deposited APTES thickness was ~ 9.2 ± 1 Å (Table 2.1, where the ellipsometry measurement was conducted to monitor the progressive increases in thickness to verify successive molecular layers). Further, a fresh porous silicon was oxidized for 3 min at 550 C to grow a thin native oxide layer for hydroxyl groups before confirming silanization and NHS-biotin binding using x-ray photoelectron spectroscopy (XPS).

Table 2.1 Ellipsometer measurement of the thickness of surface functionalized sample. A plain silicon sample was treated by oxidation, silanization, and NHS-Biotin binding and the corresponding increase in thickness was determined by ellipsometry after each coating step. The spectroscopic data was obtained from 370 nm to 1690 nm at three angles of 60°, 65°, 70°, respectively.

Layer	Name	Thickness	Name
5	Cauchy	0.35 ± 0.01	NHS-Biotin,
4	Cauchy	0.92 ± 0.01	APTES, n~1.46
3	SiO2_JAW	1.11 ± 0.01	Oxide layer
2	INTR_JAW	1.00	Interfacial layer
1	Si_JAW	N/A	Substrate

Chemical composition of the sample after each coating step was obtained by XPS analysis (K-Alpha X-ray photoelectron spectrometer, Thermo Fisher Scientific, Inc., US). Survey spectra were collected from 0 to 1100 eV with a pass energy of 160 eV and 400 μm spot size. As shown in Figure S8, carbon and nitrogen were absent for the oxidized sample, but observed after APTES coating and NHS-Biotin binding. The peak of carbon is at ~ 285.0 eV, whereas the peak at ~ 400.0 eV was assigned to N1s [85]. The XPS data with the above ellipsometry measurement verify the working protocol of the surface treatment.

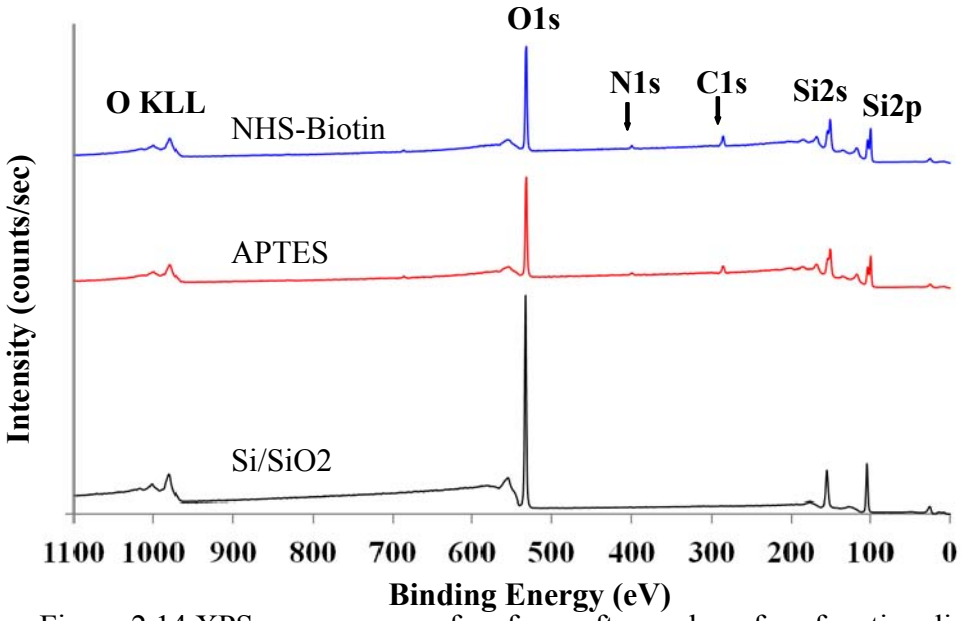

Figure 2.14 XPS survey scans of surfaces after each surface functionalization step.

After the APTES deposition, the redshift in resonance wavelength (Figure 2.15(a) and Figure 2.15(b)) for the pSi-clad resonator (~ 679.6 pm) was ~ 6 times larger than for the reference resonator (~ 112.9 pm). The APTES-induced redshift for the pSi-bearing resonator corresponded to a sensitivity of ~ 0.8 pm/(pg/mm^2). With the Q-factor of the pSi-clad microresonator being 22,000 and a reasonably assumed spectral resolution of ~

1 pm, the detection limit of the present pSi-clad sensor, in terms of deposited molecule thickness, was estimated to be ~ 0.01 Å.

As a further test of enhanced sensitivity with the pSi cladding, a layer of N-hydroxysuccinimidobiotin (NHS-Biotin) was applied via succinimide-crosslinking to the amine-terminated APTES monolayer on both devices. A layer of N-hydroxysuccinimidobiotin (NHS-Biotin, Thermo Scientific, Rockford, IL USA) was applied to the silanized sample by incubation in the mixture of NHS-biotin and anhydrous dimethyl sulfoxide (DMSO, ≥ 99.9%, Sigma Aldrich) at a concentration of 1 mg/ml for 15 h at room temperature. The samples were thoroughly washed with DMSO and DI water before characterization. Again, the measured resonance wavelength

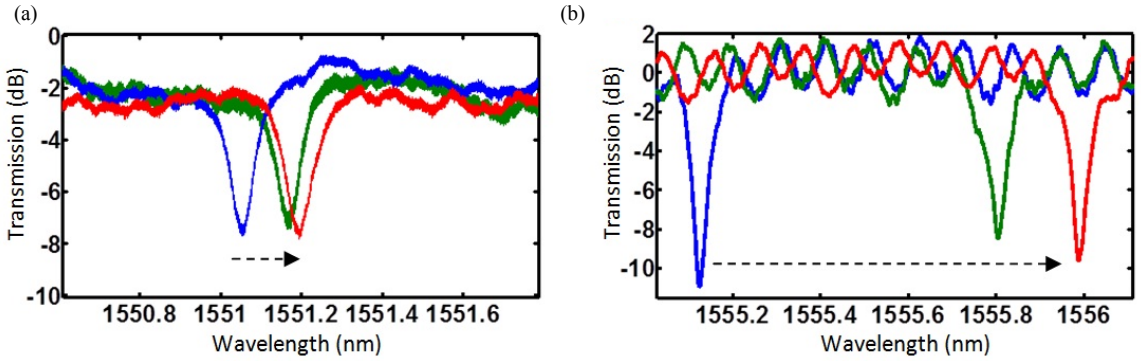

Figure 2.15 (a) Transmission spectrums of the reference resonator when no coating is applied (blue), with an APTES coating (green), and with NHS-biotin applied (red). (b) Transmission spectrums of the pSi cladded resonator when no coating is applied (blue), with an APTES coating (green), and with NHS-biotin applied (red).

redshift for the pSi resonator (~ 183.9 pm) was about ~ 6 times greater than for the reference resonator (~ 28.8 pm).

Then both samples were incubated in 5 ug/ml streptavidin (FITC conjugated streptavidin, Pierce) in phosphate buffered saline (PBS) for an hour before thorough rinsing using DI water. Interestingly, the strepavidin induced wavelength shift is ~ 0.40 nm and ~ 1.25 nm for reference and pSi-clad resonators, respectively. The corresponding sensitivity enhancement factor is ~ 3, half of the enhancement factor based on the APTES

and NHS-Biotin test. To further verify the true sensitivity enhancement factor using the pSi-clad microresonator, we took an SOI piece, part of which has a pSi cladding while other area is bare SOI, and coated in the sequence of APTES, NHS-Biotin, and streptavidin using the above mentioned protocols. In this experiment, the streptavidin is a dye conjugated streptavidin (Alexa660, Pierce). The sample was then taken to a fluorescence microscope to monitor the intensities between pSi-cladded and bare SOI regions. Figure 2.16 shows the image captured by the microscope, clearly showing a much stronger signal from the areas where a pSi cladding is present. Quantitative measurement of the intensity indicates, again, an enhancement factor of ~ 6 (232 and 39 for pSi-clad area and plain silicon area, respectively), for the pSi-clad area. This value agrees well with the result obtained in the ATPES/NHS-Biotin experiment. Therefore, we concluded that the addition of the pSi cladding indeed lead to about 6 fold increase in the surface area and the sensitivity. The relatively lower enhancement factor when detecting the streptavidin, is attributed to the size dependence of the analyte infiltration [86]. Note that the molecular weight for APTES, NHS-Biotin, and streptavidin are ~ 221 Da, 341 Da, and 60,000 Da, respectively.

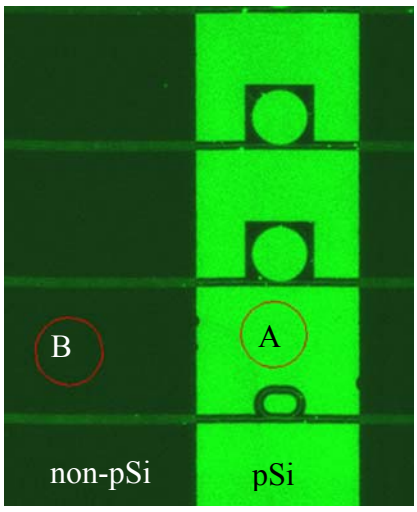

Figure 2.16 Fluorescence microscopic image of the pSi clad region (A) and bare Si region (B) after surface treatment with dye conjugated streptavidin.

2.1.5 Gas sensing test

In addition to the biosensing experiment, we further compared the gas sensitivity between pSi-clad microresonators and reference resonators using IPA vapor at different concentrations. In this test, saturated IPA from a bubbler was mixed with pure N_2 (UHP Grade, Airgas) through a Y-connector. The concentration of the IPA vapor was controlled by varying the flow rates of the saturated IPA and the carrier gas. The total flow rate of the vapor sample is kept as 100 ml/min. As is shown in Fig 2.17, the vapor was delivered to the sample via a transparent tubing (Tygon FEP-lined tubing with 0.25 inch inner diameter, Cole Palmer) that is inert to IPA. In the experiment, the concentration of the incoming IPA was set to 10 ppth (parts per thousand), and the wavelength shift for the reference resonator and pSi resonator were 140 pm and 65 pm, respectively.

Unlike the case for biosensing, use of an additional layer of pSi in the cladding reduce the sensitivity for gas sensing. This phenomenon agrees well with the demonstration reported by Yebo et. al., [87] where the vapor sensitivity is decreased upon the coating of a porous ZnO cladding. This is because of the mechanism of gas sensing, which is dominated by the free volume filling. The gas molecules are detected after they replace the air in the vicinity of the optical waveguide. When an addition pSi cladding exists, the

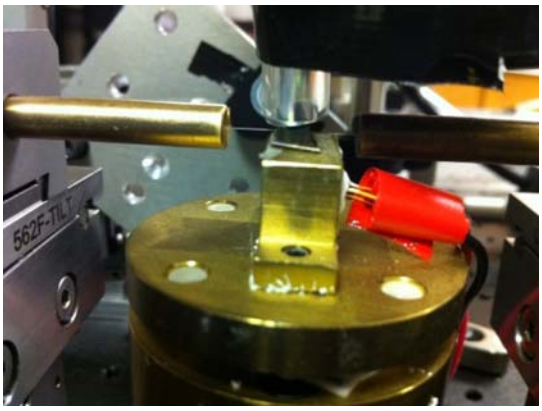

Figure 2.17 Image of gas sensing experiment setup

available volume that can be taken by the incoming gas analytes is significantly reduced. Therefore, the sensitivity is decreased.

2.1.6 Optimization with flowable-oxide (FOx)

By the "react-then-pattern" approach descrbied above, the pSi cladding only convers the top of the silicon waveguide, while both sides of the silicon waveguide are still bare silicon.Here, we propose a new approach by which the silicon waveguide is fully surrounded by a pSi film with larger surface area. This way, a device with better sensitivity is expected.

For a microresonator-based bio/chemical sensor, the adsorption of incoming analytes change the effective refractive index of the cladding and hence varies the propagation constant of the optical mode circulating in the microresonator. The sensitivity is proportional to the shift of the propagation constant upon a unit change in the cladding effective refractive index. According to the variational theorem for dielectric waveguides [88], the wavelength shift $\Delta\lambda$ is represented as equation (2-4) shown below

$$\Delta\lambda = \frac{\Delta n_{eff}\,\lambda}{n_g} \tag{2-4}$$

where λ is the operating wavelength, n_g the group index, and Δn_{eff} the change of the effective modal refractive index upon the adsorption of the incoming analyte. For the small refractive index perturbation introduced by the analyte adsorption, Δn_{eff} is written as[88]

$$\Delta n_{eff} = \frac{1}{4}\frac{\iint \Delta(n^2)|E|^2}{\eta_0 P} = \frac{1}{4}\frac{\Delta(n^2)\Gamma_P \iint_{All}|E|^2}{\eta_0 P} \tag{2-5}$$

where the confinement coefficient, Γ_P, is defined as $\Gamma_P = \iint_{Porous}|E|^2 ds / \iint_{All}|E|^2 ds$, η_0 is the impedance of vacuum, P and E are the time averaged transported power and electric field of the optical mode, respectively.

The larger the confinement factor Γ_P, the stronger the light-matter interaction and hence better sensitivity is achieved. To evaluate the sensivity of the pSi-clad microresonators, Γ_P is evaluated with various waveguide designs and geometrical parameters. In the simulation, the waveguide mode profile is investigated by full vectorial 2D finite element method (FEM). A homogeneous material with a refractive index of 1.7 is used to represent the pSi. For the initial waveguide design (520 nm by 230 nm, same as the previously fabricated device) with the strip pSi cladding ("Strip", Figure 2.18(a), top), Γ_P is calculated as a function of pSi thicknesses varying from 80 nm to 240 nm (selected to account for the selectivity of the available photoresist) for both TE and TM (transverse magnetic) polarizations. As is shown in Figure 2.18(b), Γ_P increases monotonically as the pSi cladding becomes thicker. Γ_P of TM modes is larger than that of TE modes, but it is more sensitive to the pSi thickness than that of TE modes. The previously demonstrated sensitivity of 0.8 pm/(pg/mm^2) is obtained with a 120 nm thick pSi cladding under TE polarization, corresponding to a confinement factor of 7.6%. Γ_P is 31.0% for a 240 nm thick pSi cladding under TM polarization, indicating that the sensitivity can potentially be increased by a factor of four by increasing the pSi thickness and using TM polorization.

To further increase Γ_P, we propose a new waveguide design ("wrap"), where the pSi cladding also covers both sides of the waveguide (Figure 2.18(a), bottom). Γ_P of the "wrap" waveguide is consistently larger than that of the "strip" configuration, particularly under TE polarization, indicating a much better sensitivity with the "wrap" waveguide configuration. Highest Γ_P achieved in simulation is 32.6% with a 240 nm thick pSi under TM polarization, leading to a very promising sensitivity of ~ 0.2 pm/(pg/mm^2).

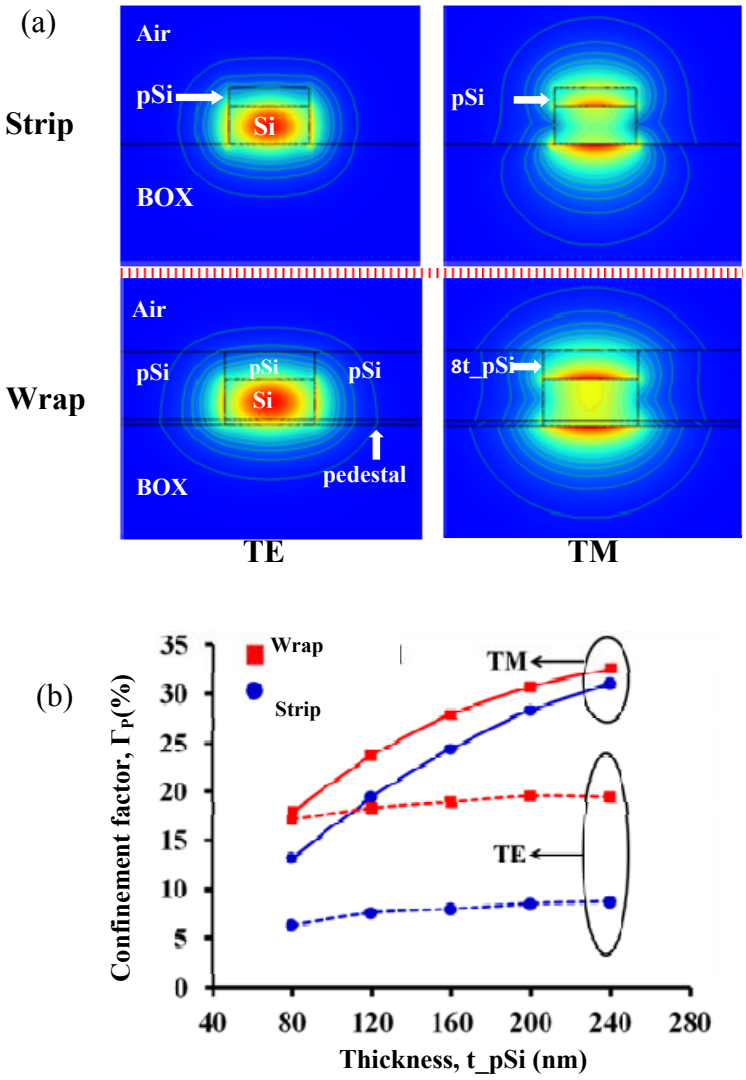

Figure 2.18 (a) E-field profiles for "strip" and "wrap" waveguide configurations under TE and TM polarizations; (b) Confinement factor varying as a function of pSi thickness for "strip" and "wrap" waveguide configurations for both polarizations.

Figure 2.19 Fabrication of FOx-based pSi clad microresonators.

The fabrication process is shown as Fig. 2.19, and explained as follows:

Step 1: Fabrication of SOI microresonators with a pedestal layer.

The fabrication of the SOI microresonators is similar to the process described above. However, it is worth noting that the pedestal layer is very critical because of its capability of protecting the buried oxide layer from reaction with the magnesium at high temperature.

Step 2: FOx coating and annealing.

After thorough clean the sample with acetone, methanol, and IPA, a layer of FOx is applied to the surface of the sample via spin coating at 2000 rpm for 1 min. Then, heat the sample on three consecutive hot plates at 150 ^{o}C, 250 ^{o}C, and 350 ^{o}C for 1 min each, to reflow the FOx and fill the narrow gaps in the film.

Prior to converting the sample into pSi-clad microresonators, it is of vital importance to first anneal it in the furnace (oxygen ambient) at 800 ^{o}C for 1 hour. This annealing step is critical to converts the FOx to silicon dioxide. Fig 2. 20(a) shows the result after conversion if this annealing step is absent, clearly shows the stress that leads to a pSi film coil. However, this issue could be well resolved if the annealing is adopted in the process.

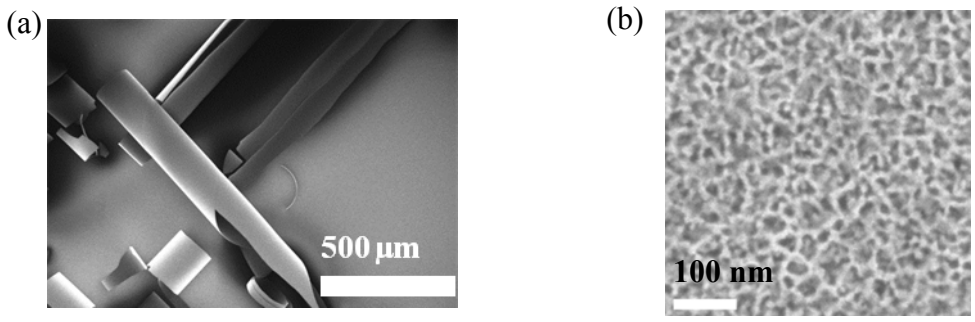

Figure 2.20 (a) SEM of the cross section of a "wrap" pSi-clad waveguide. (b) Transmission of a 20 µm radius microring resonator with the "wrap" waveguide configuration.

Step 3: Conversion from silicon dioxide to pSi.

Same as the process described above, extreme care needs to be taken to ensure the cleanliness of the sample prior to the conversion (S. Davis, Sandhage group).

Fig 2.21 shows a fabricated "wrap" waveguide in a 20 µm radius microring resonator. The thickness of the silicon waveguide is ~ 250 nm, while the thickness of the pSi is ~ 120 nm. The loaded Q-factor is ~ 5,000 under TE polarization, lower than the previously reported Q-factor of 22,000 for a 120 nm thick "strip" cladding waveguide. It suggests that the increased Γ_P is achieved at the expense of a larger optical loss because of the increased scattering loss. However, deposition of a monolayer of APTES according to the previously described protocol leads to a wavelength shift of ~ 1.28 nm, almost a factor of two improvement over the case of the "strip" pSi cladding waveguide, and more than an

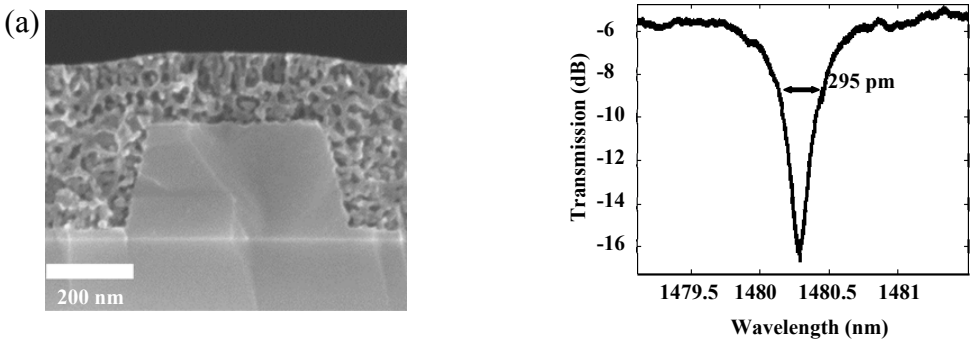

Figure 2.21 (a) SEM of the cross section of a "wrap" pSi-clad waveguide. (b) Transmission of a 20 µm radius microring resonator with the "wrap" waveguide configuration.

order of magnitude larger than the bare SOI microresoantors.

In addition to the further improved sensitivity, this method eliminates the need of etching the pSi and silicon films after conversion. Therefore, the thickness of the pSi cladding is no longer limited by the available thickness of the resist and etching selectivity.

2.2 pSi-clad microresonators based on porous alumina membrane

2.2.1 Motivation

While the magnesiothermic reduction approach described in Section 2.1 yields uniform pSi films with a large surface area for significant improvement of sensitivity, one challenge of this method is the ability to reliably tune the pore size and porosity in the produced film. Based on the reaction (2-1), the porosity is fixed at 65.9%. Meanwhile, the small feature size in the pSi film and the interwoven nature of the film make it only suitable of detecting small molecules. When the size of the target molecule is relatively large (length of ~ 5.5 nm for the streptavidin with molecular weight of ~ 66 kDa), it is observed that the sensitivity enhancement factor is reduced from a factor of ~ 6 to ~ 3. Therefore, to gain the maximal benefit from these porous films, it is desired to realize a structure whose pore size and porosity can be well controlled.

In this work, a method is described (protocol developed and conducted by Dr. Ari Gordin, Sandhage group) which allows for the fabrication of thin, uniform pSi films on SOI travelling-wave microresonators, with the ability to tune both the size of the pores in the pSi cladding as well as the thickness of the pSi cladding. This approach is based on pattern transfer of a porous anodized alumina membrane (PAAM) into a SOI substrate. While reports of pattern transfer of PAAM into silicon substrates have been published previously [89-91], such method has never been demonstrated with the fabrication of pSi-clad SOI microresonators. In the remainder of this chapter, the fabrication, characterization and modeling of these devices will be described.

2.2.2 Fabrication process

The fabrication process is schematically shown in Figure 2.22 and described as follows:

Step 1: Evaporation of aluminum layer

An unpatterned SOI wafer with 300 nm silicon device layer is coated by ~ 800 nm Al with ebeam evaporation (CHA E-beam Evaporator) at a speed of ~ 0.3 nm/s.

Step 2: Anodization of aluminum

The Al-coated SOI substrates are subject to standard two-step anodization procedure (A. Gordin, Sandhage group). In the first step, coated wafers are anodized in either sulfuric acid (0.3M, 10°C, 25V) or oxalic acid (0.3M, 20°C, 40V) for 7 minutes, after which the Al_2O_3 layer was etched in a solution of chromic and phosphoric acid. The remaining Al was anodized under identical conditions as those used in the first step, and the anodization was allowed to proceed until a sharp drop in current density was

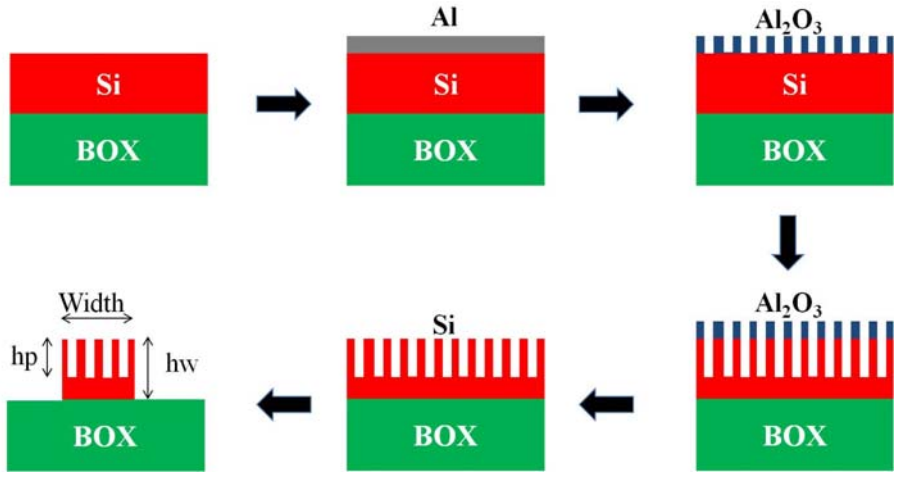

Figure 2.22 Fabrication of pSi-clad SOI microresonators based the PAAM approach.

observed, indicating that the entire Al coating had been converted into porous alumina. The two-step anodization method is known to yield a more uniform pore distribution than

single-step anodization and further serves to reduce the thickness of the PAAM mask to only a few hundred nanometers to allow for its use as a mask during reactive ion etching. Following complete anodization, pore widening was carried out in phosphoric acid (5 wt%) in order to achieve the desired pore diameters.

Unlike anodization of silicon to form pSi, in which the applied current passes through the thickness of the wafer (i.e., the electrode is applied to the back of the Si substrate in order to achieve pore formation on the front-side of the substrate), during anodization of aluminum the applied current passes through the substrate laterally (i.e., in order to achieve pore formation on the front-side of the substrate, the electrode is also placed on the front side of the substrate). Anodization of Si cannot be carried out on SOI substrates since the buried oxide layer of SOI substrates breaks electrical contact between the front and back sides of the wafer. However, since anodization of Al occurs via lateral movement of electrical current across the conductive aluminum layer, the buried oxide presents no similar difficulty for anodization of aluminum. The pitch length, defined as the distance from the center of one pore to the center of an adjacent pore, is determined by the voltage and electrolyte used during anodization, while the pore diameter is determined by the etching time and etchant concentration used during pore widening. Figure 2.23 (a)-(c) show the effect of varying both anodization voltage and pore widening time on PAAM masks fabricated on Si-wafers. Anodization at 25V with no pore widening results in very small pore diameters (<20 nm, Figure 2.23(a)). After 40 minutes of pore widening in phosphoric acid (5%), the average pore diameter was approximately 30 nm (Figure 2.23(b)). Increasing the anodization voltage to 40V and the pore widening time of 80 minutes, the pore diameter increased to ~60 nm (Figure 2.23(c)) (A. Gordin, Sandhage group).

Step 3: pattern transfer to silicon device layer

Once the desired PAAM is finished. It is used as a mask to etch the underneath silicon device layer forming cylindrical porous silicon structure replicating that of the

PAAM. Before etching the silicon using Cl_2 (plasma therm ICP), it is very important to remove the barrier layer with CF_4 (Oxford Endpoint RIE) [91]. Figure 2.24 (a) is the result after silicon etching, indicating that the pSi pattern is a replicate of that of the PAAM. The use of aluminum anodization allows for substantial control over pore geometry and size. Therefore, this approach enables good control over the pore size and porosity of the yielded pSi film.

Step 4: PAAM removal

The PAAM is removed via immersion in a chromic acid (1.7 wt%) / phosphoric acid (5.3 wt%) mixture for 1 hour. The resulting pSi layer consisted of a uniform layer of cylindrical pores directly inherited from the PAAM . As the kinetics of Si-etching in

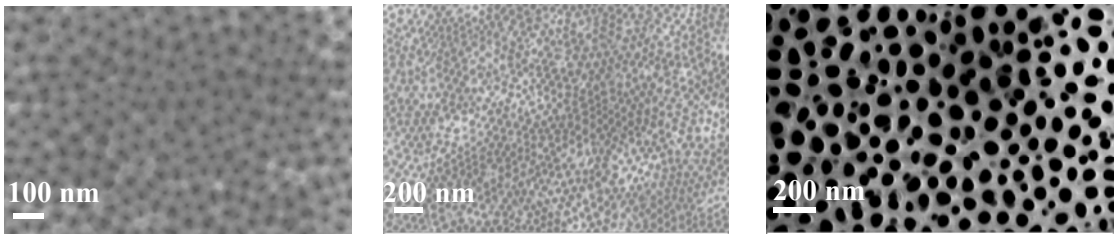

(a) (b) (c)

Figure 2.23 Porous anodized alumina membranes (PAAM) fabricated via (a) anodization at 25V with no pore widening (average pore size <20 nm; (b) anodization at 25V with 50 minutes of pore widening (average pore size ~30 nm); (c) anodization at 40V with 80 minutes of pore widening (average pore size ~60 nm) (Provided by A. Gordin).

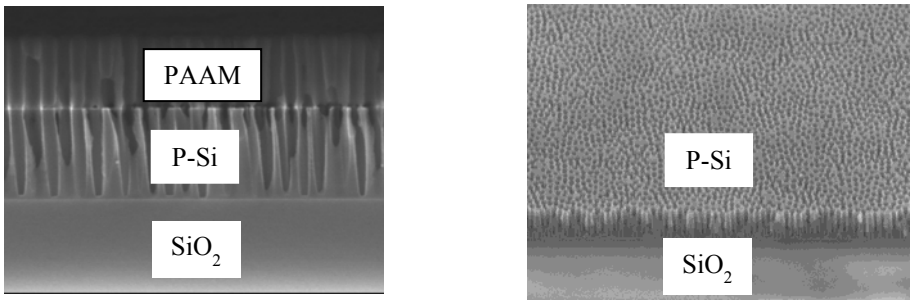

(a) (b)

Figure 2.24 Porous anodized alumina membranes (PAAM) on SOI after (a) pattern transfer to silicon layer; (b) after dissolution of PAAM.

chlorine gas are well known, the depth of the porous layer can be controlled precisely.

Step 5: Device fabrication

The resulting pSi-clad SOI substrates are patterned into microresonators using electron beam lithography with ZEP520 as the resist. However, due to the additional loss introduced by the pSi cladding, it is necessary to first pattern a window which has pSi cladding everywhere, while the outside is still regular SOI configuration with low optical loss (Figure 2.25 (a)). Figure 2.25 (b) are the SEMs of the pSi clad waveguides. The

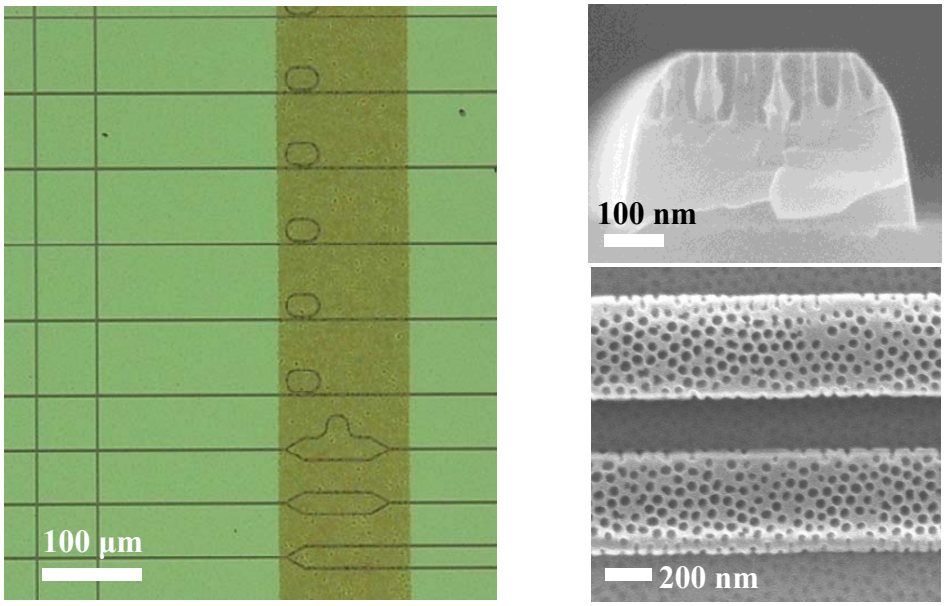

(a) (b)

Figure 2.25 (a) Illustration of the pSi window (dark yellow) inside which the devices possess pSi, while it is regular SOI configuration; (b) SEMs showing the cross section and the top-view of a pSi-clad waveguide.

thickness of the pSi portion is ~ 120 nm, while it is ~ 180 nm for the dense silicon base.

2.2.3 Characterization

The use of a porous silicon cladding derived from anodized alumina yields highly uniform cylindrical pores with and allows for significant control over pore size, potentially allowing for development of sensors designed specifically for a range of

biological agents. Previously published sensors based on pSi-clad, SOI microresonators relied on pSi derived from magnesiothermic reduction of SiO_2, for which no control over pore size has even been reported. The cylindrical nature of the pores further provides facile access of the analytes to the surface area of the pores, especially when compared to the complex 3D pore geometry which results from magnesiothermic reduction of SiO_2.

The transmission spectra of a microresonator containing the 120 nm thick pSi cladding under transverse electric (TE, electric field in the plane of device) polarization is shown in Figure 2.26. The FWHM of the resonance at 1561 nm was approximately 310 pm, corresponding to a loaded quality factor of 5,000 for the pSi-clad sample. The propagation loss at 1550 nm is estimated to be around 60 dB/cm. The moderate Q factor is because of the roughness introduced by the cylindrical pores in the waveguides. To quantitatively evaluate the impact of the pSi cladding on the analyte adsorption capacity and the sensitivity of the microresonator sensors, the pSi clad microresonators were functionalized with APTES and NHS-Biotin using standard protocols [80, 84]. As is seen in Figure 2.26, the resonance wavelength is shifted by ~ 610 pm when the APTES is coated on the resonator, and another ~ 230 pm after the deposition of NHS-Biotin.

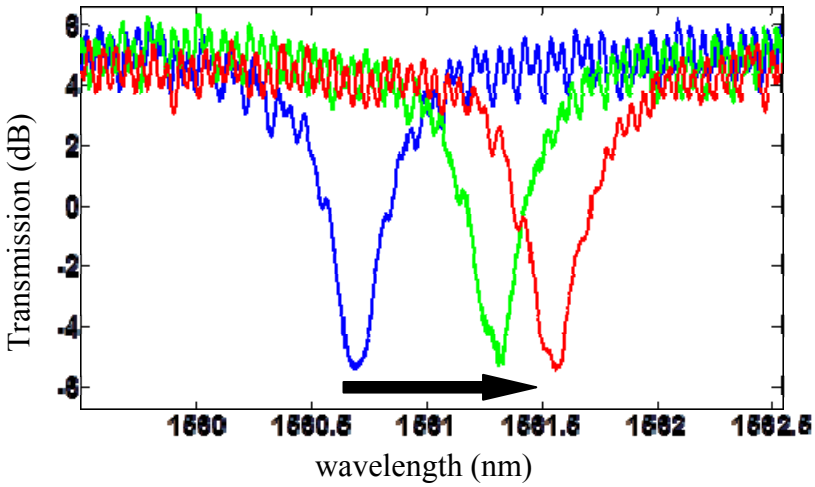

Figure 2.26 (Blue) Transmission spectrum of a pSi-clad racetrack resonator under TE polarization. The radius and the length of the straight portion are both 10 μms; (Green) Transmission spectrum of the same resonator after APTES coating; (Red) Transmission spectrum after NHS-Biotin coating.

Compared to the ~ 113 pm for the reference SOI microresonator in the last section, a sensitivity enhancement factor of ~ 5.5 is achieved, which is comparable to the results obtained with the magnesiothermic reduction approach.

2.2.4 Modeling of the PAAM based pSi-clad microresonator

A model was built to study the relationship between the wavelength shift upon

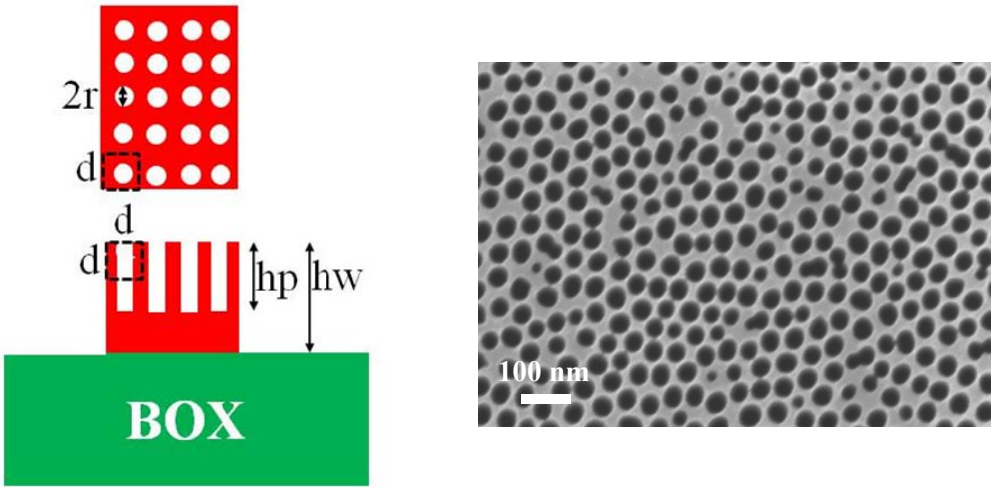

(a) (b)

Figure 2.27 (a) Illustration of the modeling of PAAM based pSi clad optical waveguide; (b) SEM of top view of a PAAM based pSi film.

analyte adsorption and the geometric parameters of the pSi-clad microresonators. The analyte adsorption induced Δn_{eff} can be related to the geometrical parameters shown in Figure 2.27 (a) as

$$\Delta n_{eff} = \frac{t}{2\eta_0 P} \frac{\rho \Delta(n^2) \iint |E|^2}{r} \tag{2-6}$$

where r is the average pore radius, ρ is the porosity and t is the thickness of the adsorbed biolayer. Combining equations (2-3) and (2-6) leads to the wavelength shift Δλ of a pSi-clad microresonator as follows:

$$\Delta\lambda = \frac{\lambda}{n_g} \cdot \frac{t}{2\eta_0 P} \frac{\rho\Delta(n^2)\iint |E|^2}{r} \tag{2-7}$$

Finite element method was adopted to obtain the group index n_g, power P and electric field E. The equivalent refractive index of the film for different porosity can be obtained by the parallel model under TE polarization [92]. A MATLAB code was written to estimate the porosity using Figure 2.27(b), and the result is ~ 0.51. Figure 2.28 is the simulation results showing the wavelength shift upon a 0.92 nm thick of APTES (n=1.46)

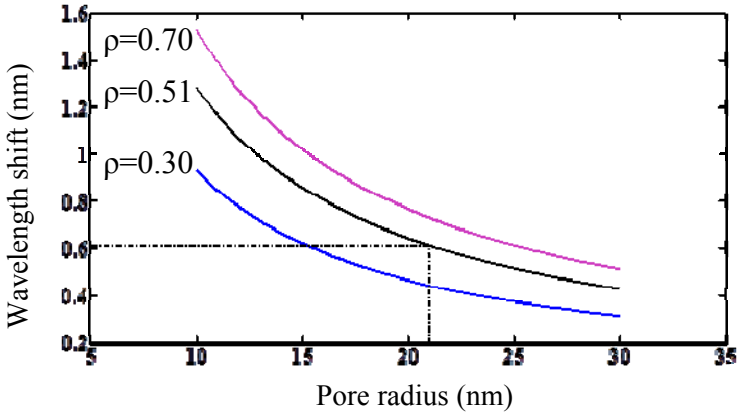

Figure 2.28 Wavelength shift as a function of average pore radius for varying porosities. Pore radius of ~ 21 nm and 0.51 porosity lead to ~ 616.2 pm redshift in the resonance wavelength for 0.92 nm APTES coating, which agrees well with the ~ 610 pm experimental result.

is adsorbed by the pSi-clad resonator whose pSi clad consists of varying pore radius and porosities. It suggests that higher porosity and smaller pore radius lead to larger wavelength shift. For the special case of pore radius of ~ 21 nm and ~51% porosity, the calculated wavelength shift is 616.2 pm, which is consistent with the experimental wavelength shift of ~ 610 pm.

Further, the influence of the pSi cladding thickness on the wavelength shift is investigated and represented in Figure 2.29. In this study, the total thickness of the waveguide *hw* and pSi cladding *hp* is kept to be at 300 nm. When the pSi becomes thicker, the surface area is increased, and hence the wavelength shift increases. However,

the sidewall roughness induced by the pSi cladding would also lead to scattering loss. Therefore, the pSi cladding thickness can not be increased arbitrarily. In fact, we have fabricated optical waveguides consisting of 300 nm thick pSi by etching all the way down to the buried oxide layer. No light output was observed in those experiments.

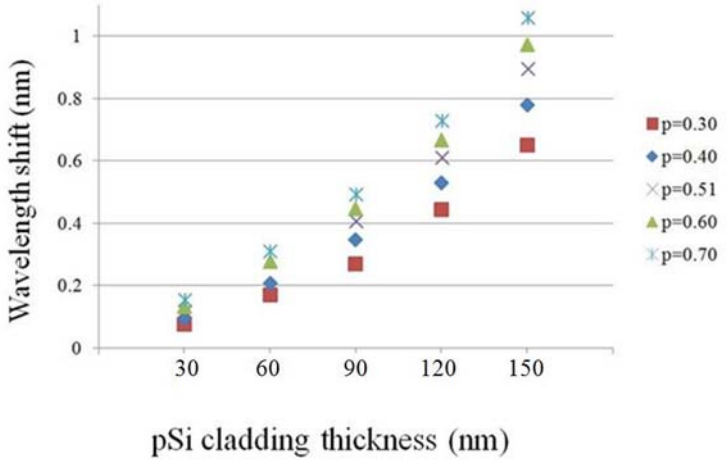

Figure 2.29 Wavelength shift as a function of PAAM based pSi cladding thickness at varying porosities.

2.2.5 Gas sensing test

In this test, the response of four racetrack resonators to IPA vapor at varying concentrations are measured. The four racetrack resonators share the same geometric design parameters. However, their waveguide structures are different (Figure 2.30). They are standard SOI waveguide with 300 nm thick of silicon device layer, 180 nm thick silicon waveguide with 120 nm PAAM based pSi cladding, standard waveguide with polymer cladding, and the pSi clad waveguide covered by polymer coating. The polymer used in this test is 4-vinyl-phenol (PVP, Sigma Aldrich).

Figure 2.31 are the measured transmission spectrums of the four racetrack resonators under TE polarization. Microresonators consisting of standard SOI waveguides show larger Q factor: intrinsic Q-factors of ~60,000 and ~35,000 for SOI and SOI with polymer coating, respectively. The addition of the PVP coating does not significantly reduce the Q factors. However, when a pSi waveguide is incorporated, the Q factor will

drop dramatically. The intrinsic Q-factors are ~7,000 and ~6,000 for pSi and pSi with polymer coating. The FSRs for the four resonators are measured to be 6.56 nm, 6.57 nm, 6.54 nm, and 6.86 nm, respectively.

Figure 2.32 represents the resulted wavelength drifts for the four resonators at varying IPA concentrations. Adding polymers and porosification of the structure both contribute positively to the increase of the sensitivity. When comparing the cases between standard 300 nm SOI and 120 nm thick pSi with polymer coating, the sensitivity enhancement factor is ~ 2.5. However, the price to be paid is a dramatic reduction of Q factor, from 60,000 for SOI and 6,000 for the latter case.

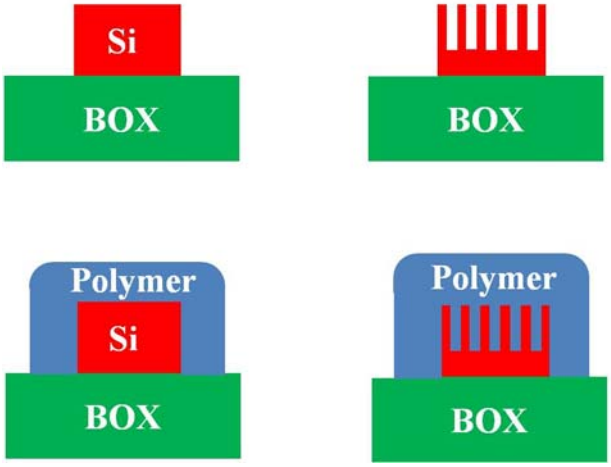

Figure 2.30 Four types of waveguide structure in the IPA sensing test.

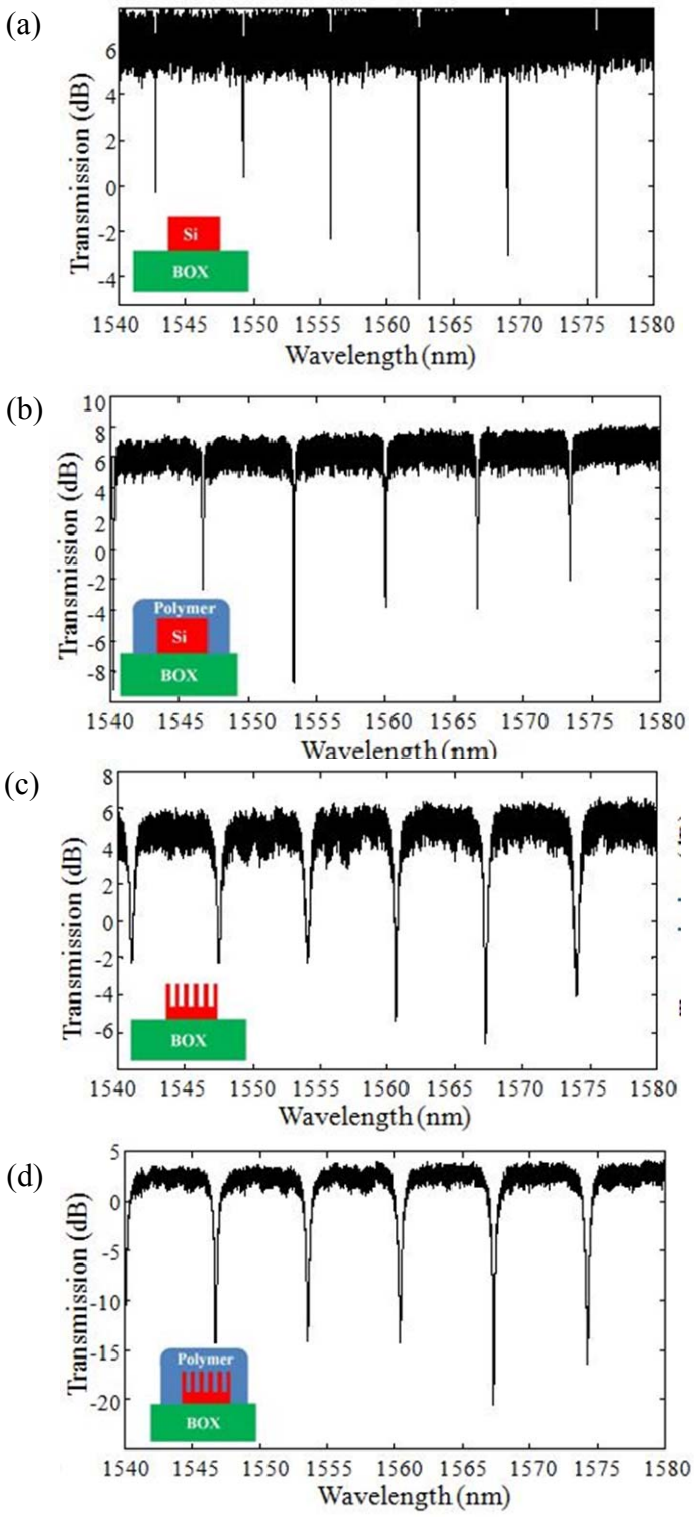

Figure 2.31Transmission spectra of the four racetrack resonators consisting of four different waveguide configurations: (a)standard SOI (b)standard SOI+Polymer; (c) PAAM pSi (d)PAAM pSi+Polymer. The thickness for standard SOI is 300 nm. pSi waveguide consists of a 180 nm dense silicon with 120 pSi cladding.

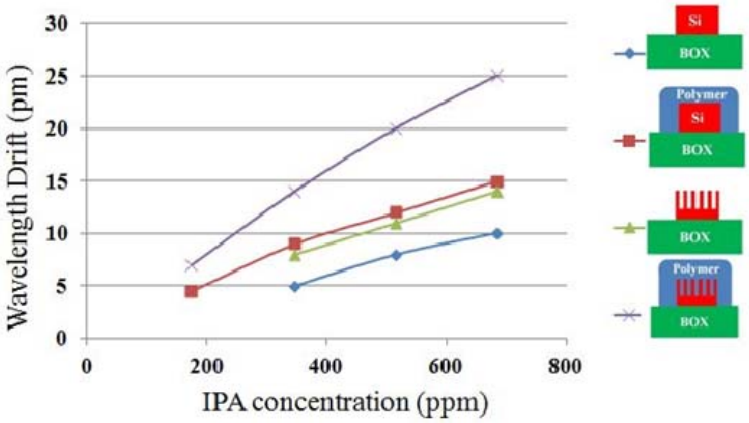

Figure 2.32 Resonance wavelength drift of the four resonators versus varying incoming IPA concentrations.

2.3 Porous titania clad SiN microresonator sensors

2.3.1 Motivation

Besides porous Si/SiO_2 [43, 44, 48, 51, 93], other porous materials such as porous TiO_2 [94-96] and porous Al_2O_3 [97, 98] have also gained widespread interest in various biosensing applications. The large surface area provided by the porous matrix enables enhanced biomolecular interactions that are often bounded at the receptor-functionalized surfaces. Although porous Si/SiO_2 has been the most prominent candidate in label-free optical sensors because of the ease of fabrication and versatile surface modification. However, despite the impressing progress in pSi biosensors, one fundamental limitation in using pSi is the poor stability [94, 99]. Oxidation and carbonization help to remove the unstable Si-H groups on the sensor surface, but the pSi suffers corrosion and dissolution under physiological and higher PH range (PH>8) and may lead to a biased measurement [94]. Titania, on the other hand, exhibits excellent chemical stability at a much wider PH range (from 2 to 12) [94]. It is an excellent optical material with low loss and high refractive index (~ 2.4 at anatase phase). More importantly, being capable of forming surface hydroxlys, the approach to functionalization of titania resembles that of silica,

whose surface functionalization has been extensively investigated and applied to various sensing scenarios [100]. These properties render titania a very promising material in the label free optical sensing.

A variety of approaches have been investigated to make porous titania films [101-104]. Among these methods, the protamine-mediated layer-by-layer process has proven to be a straightforward approach to synthesize continuous and conformal porous titania films on various substrates [103, 104]. Conducted in aqueous solutions, this approach does not need time-consuming and multistep silica surface functionalization protocols. However, this method only leads to films possessing monosize pores of less than 5 nm in diameter. The lack of tunability of the pore size makes it very challenging to allow for biomolecules with various sizes [86, 105]. To address this issue, we introduce carboxyl spheres as transient pore-forming agents in the process to tune the pore size in the film (Dr. Yunshu Zhang, Sandhage group). The spheres can be burned away to yield conformal anatase titania coatings with controlled mesopore sizes predefined by the spheres. This novel process enables to engineer the pore sizes in the porous titania coatings to allow for easy access of various biomolecules and analytes, while maintaining a high surface area. Using this method, we demonstrate a compact, high Q factor silicon nitride microring resonator coated with uniform porous titania whose pore size is ~ 30 nm. The advantage of using SiN as the substrate is that it possesses a much lower thermal optic coefficient than silicon and is thus less vulnerable to adverse environmental variations. The proposed SiN microring resonator enables for high sensitivity in bio/chemical sensing because of two contributions: 1) resonance-based field enhancement, and 2) increased surface area for analyte adsorption and for maximizing the interaction of the optical field with the incoming analyte.

2.3.2 Design and fabrication

SiN microring resonators are designed to ensure single mode operation with high Q factor at 1550 nm wavelength region. The fabrication flow is shown in Figure 2.33. They were fabricated on wafers with a LPCVD SiN (Tystar Nitride) deposited on a 4-μm-thick oxide layer. The SiN growth was optimized for low optical loss and low stress to enable 400 nm of SiN device layer [106]. To pattern the SiN devices, a JEOL JBX-9300FS electron-beam lithography (EBL) system was used with ZEP520A (by Zeon cooperation) as the e-beam resist. The pattern was then transferred to the SiN layer using the plasma etching with a CF_4/CHF_3 gas mixture in Oxford Endpoint RIE. Afterwards, the samples were coated with mesoporous anatase titania as shown in Figure 2.34.

To coat the SiN microring resonators with porous titania, the sample was first soaked in 100 mM Tris-HCl buffer solution (pH=8, prepared from 1 M Tris-HCl, Teknova, Hollister, CA) before incubation in 1 mg/ml protamine solution (prepared from protamine sulfate salt from salmon, Sigma-Aldrich, St. Louis, MO) for 5 minutes. After rinsing with buffer solution three times, the sample was immersed in 1 mg/ml carboxyl sphere solution (prepared from P(S/V-COOH) solution, Bang Laboratories, Fisher, IN) for 5 minutes followed by three times of rinsing with buffer solution to remove unbound molecules. Then the sample was incubated in protamine solution for 5 minutes, and in 5 mM Ti(IV)bis-ammonium-lactato-dihydroxide (TiBALDH, Sigma-Aldrich, St. Louis, MO) solution for 15 minutes and washed in buffer solution three times. In this process, the pore size and thickness of the porous titania are determined by the size of the carboxyl spheres and the number of cycles repeated in the procedure. The diameter of the monosized carboxyl spheres was chosen to be ~ 26 nm (Figure 2.35 (a)). The above process was conducted three times to achieve a thickness of ~ 70 nm. The pore size and thickness of the porous titania film were chosen to maintain low loss operation at the wavelength of 1550 nm and assure the porous titania is well covered by the evanescent

tail of the optical mode for large light-matter interaction. Finally, the sample was washed with de-ionized (DI) water thoroughly and dried with flowing nitrogen, and fired at 500 ^{o}C for 4 hours in air to obtain anatase titania coatings (Figure 2.35 (b)) (Protocol developed and conducted by Y. Zhang, Sandhage group).

The radius of the fabricated SiN microring resonator is 40 μm, as is illustrated in Figure 2.36(a). The feature size of the void space in the porous titania matrix is ~ 30 nm (Figure 2.36(b)), which agrees well with the 26 nm carboxyl spheres. After three cycles of deposition, the final thickness of the porous titania after firing is ~ 70 nm.

2.3.2 Sensing demonstration

Similar to the previous section, the characterization of the devices was conducted with a tunable laser (81640A, Agilent Technologies) as the light source. A pair of tapered fibers was employed to couple light into and out of the device. The output signal was detected by an InGaAs photodetector (Thorlabs PDB 150C). A thermal stage (Thorlabs TED 200C) was used to keep the temperature fixed at 24 °C during the characterization. The transverse electric (TE) transmission spectra of a reference microring resonator and a porous-titania-clad microring resonator are shown in Figure 2.37 (a) and Figure 2.37(b), respectively. The loaded Q factors of the reference SiN resonator and porous-titania-clad resonator are ~ 230,000 and 51,000, respectively.

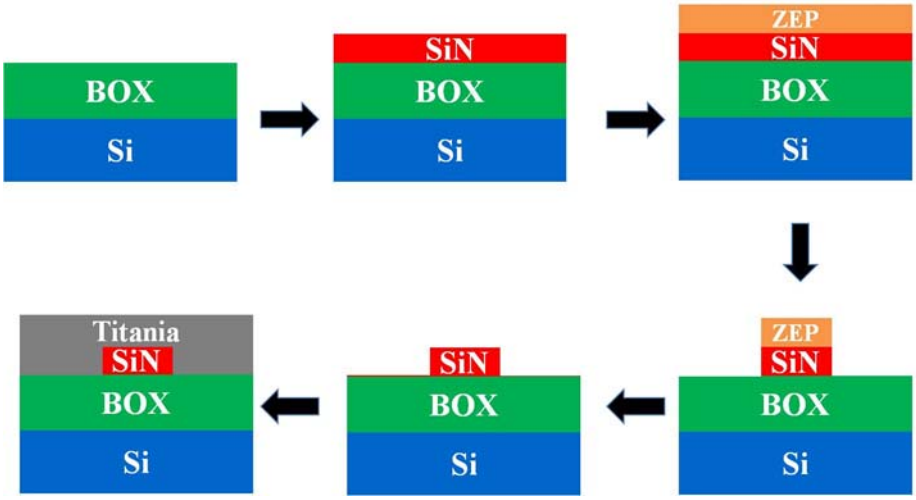

Figure 2.33 Fabrication flow of the porous titania clad SiN microresonator

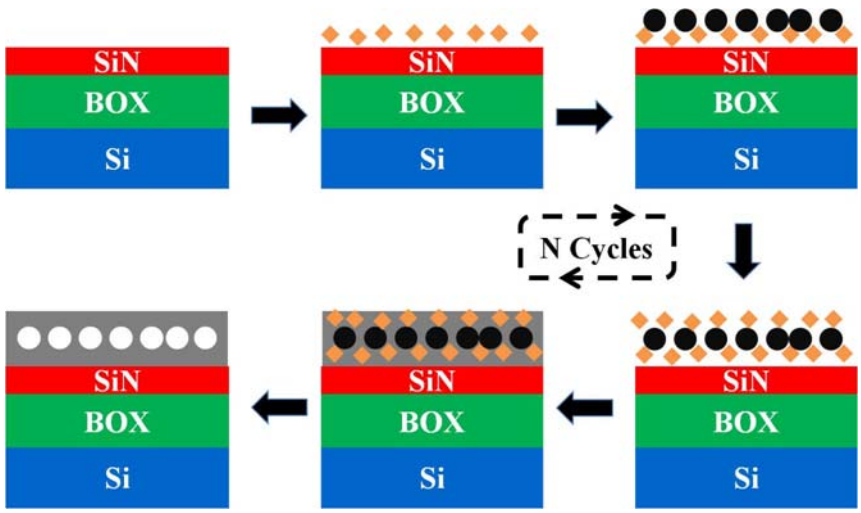

Figure 2.34 Deposition procedure of protamine-enabled porous titania with carboxyl spheres.

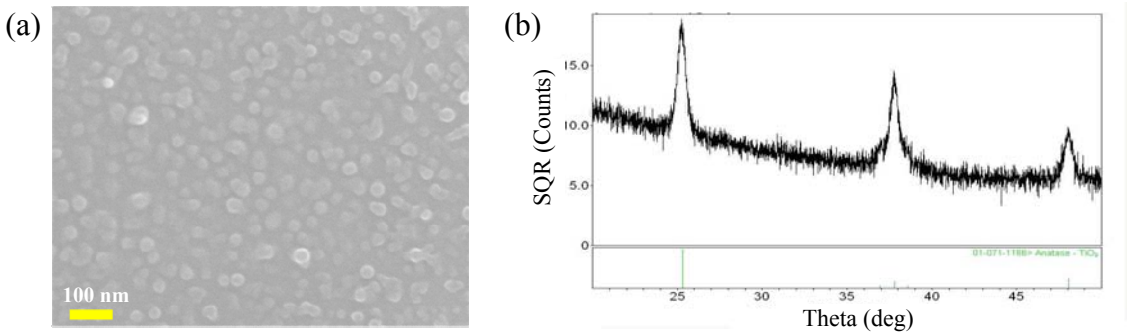

Figure 2.35. (a) Protamine mixed with carboxyl spheres of size ~ 26 nm; (b) Grazing XRD pattern of titania coating with 26 nm carboxyl spheres after fired at 500 ^{o}C for 4 hours. (Provided by Y. Zhang, Sandhage group)

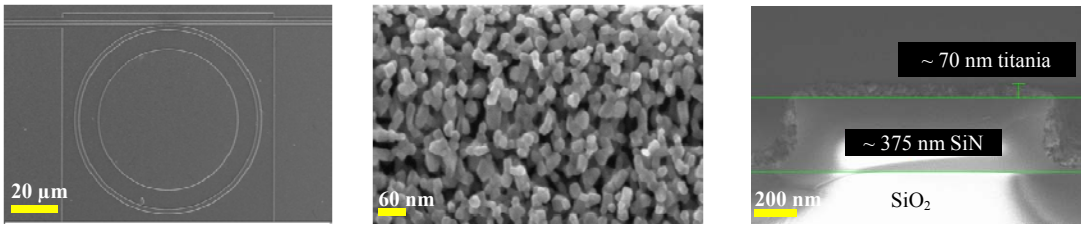

(a) (b) (c)

Figure 2.36 Scanning electron microscopic images of (a) 40 µm radius SiN microring resonator coated with porous titania; (b) close-up of porous titania with feature sizes of ~30 nm; (c) cross-section of the porous titania coated SiN waveguide, showing a ~ 70 nm thick porous titania on top of the SiN waveguide.

Again, to quantitatively evaluate the enhanced analyte adsorption resulting from the increased surface area of the porous titania cladding, (3-aminopropyl)triethoxysilane (APTES) and N-hydroxysuccinimidobiotin (NHS-Biotin) monolayers were deposited on the porous titania cladding and reference resonators. Since the functionalization of titania resembles that of silica, the procedure is similar to that reported in [80]. Briefly, the samples were first thermally oxidized to promote covalent attachment of 3-aminopropyltriethoxysilane (99%, Sigma Aldrich), and then were soaked in a mixture comprised of APTES, methanol, and deionized water (DI water) for 20 min at room temperature. After incubation, the samples were thoroughly cleaned with methanol and DI water prior to the characterization. After the 9.2 Å APTES deposition, the redshift in resonance wavelength (Figure 2.37(a) and Figure 2.37(b)) for the porous-titania-clad

resonator (~ 2.36 nm) was more than an order of magnitude larger (by a factor of ~ 12.5) than for the reference resonator (~ 187.5 pm). As a further study of the enhanced sensitivity, a layer of NHS-Biotin was applied to the silanized samples. Again, the measured resonance wavelength redshift for the porous titania resonator (~ 810.2 pm) was an order of magnitude greater than for the reference resonator (~ 71.2 pm).

Considering the APTES density of 0.946 g/mL [107], the redshift for the porous titania microring resonator corresponds to a sensitivity of ~ 2.8 pm/(pg/mm^2). Although the demonstrated Q factor of the porous titania (~ 51,000) is less than the reference SiN resonator (~230,000) and other reported work [106, 108, 109], it is reasonable to assume a spectral resolution of 1 pm [30, 36]. Therefore, the detection limit of the presented porous-titania-clad SiN microring resonator, in terms of areal mass density, is ~ 0.4 pg/mm^2, better than the previously described magnesiothermic reduction based pSi-clad SOI microring resonator by a factor of two.

Also, we tested its gas sensing performance using the setup similar as that in Section 2. 1. Here, toluene vapor at varying concentrations was injected to the tubing and brought to the vicinity of the sample. Figure 2.38 shows the real time wavelength shift at varying toluene concentrations. The response was reversible and fast. It took the device

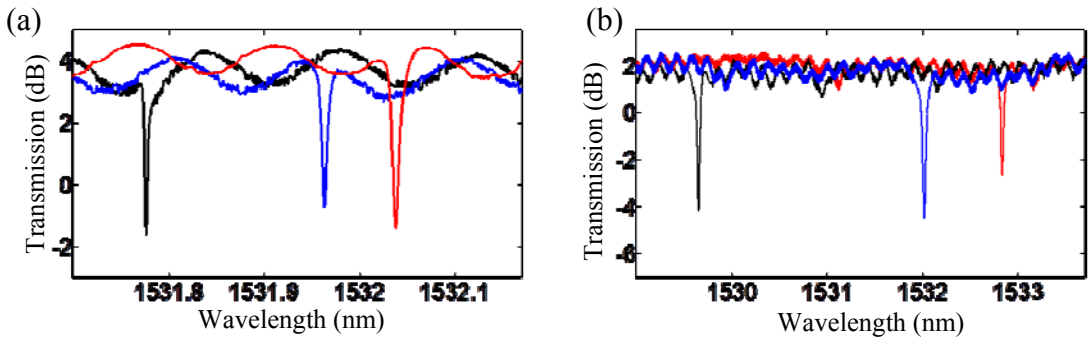

Figure 2.37 (a) Transmission spectrums of the reference resonator when no porous titania coating is applied (black), with an APTES coating (blue), and with NHS-biotin applied (red). (b) Transmission spectrums of the porous titania cladded resonator when no coating is applied (black), with an APTES coating (blue), and with NHS-biotin applied (red).

less than a minute to respond to the variation in the toluene concentration. Figure 2.39 plots the wavelength shift versus the concentration of the incoming toluene. A good linearity was observed. Based on the slope in the curve, an estimated detection limit for toluene is ~ 6 ppm at room temperature.

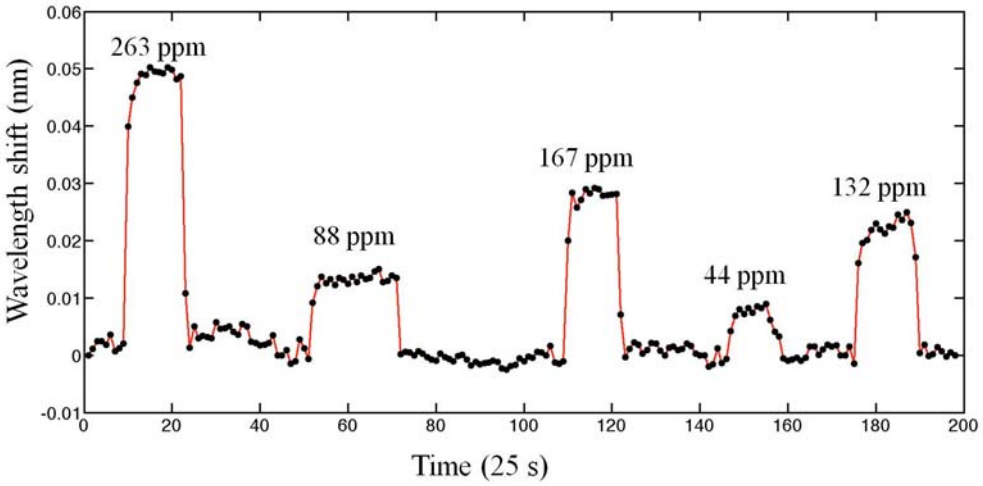

Figure 2.38 Real time response of the porous titania clad SiN microring resonator exposed to vapor toluene at varying concentrations.

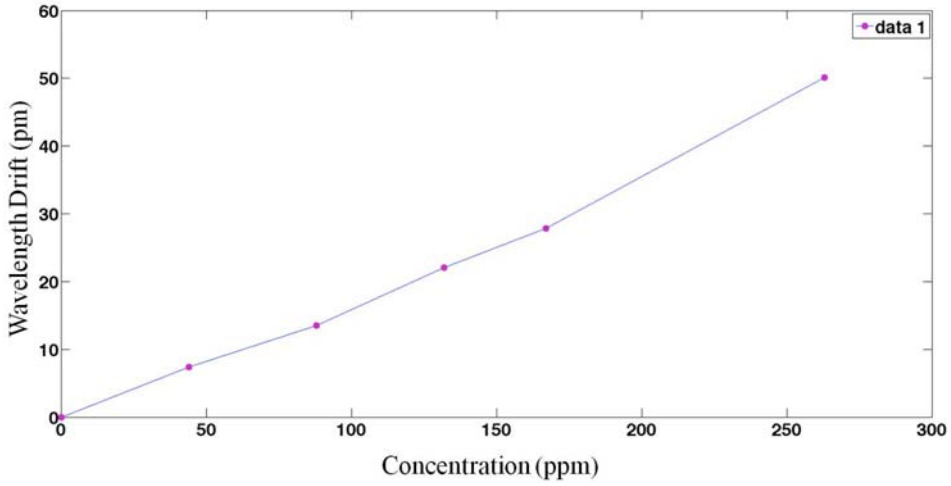

Figure 2.39 Wavelength shift of the porous titania clad SiN microring resonator as a function of the incoming toluene concentration.

CHAPTER 3

MULTIPLEXED GAS SENSING WITH ARRAYED SOI MICRORING RESONATORS

In this chapter, the design, fabrication and characterization of a multiplexed gas sensor coated with four polymers are described. Selective coating of polymers on an SOI substrate with good positioning accuracy and reliability is presented.

3.1 Motivation

Integrated photonic microresonator gas sensors have attracted a lot of attention for their high sensitivity, fast response, and ease of implementation [28, 87]. Typically, the optical sensors are coated with a layer of polymer whose refractive index will be changed upon the diffusion and adsorption of the incoming gas molecules. This change of refractive index is then transferred to the drift of resonance wavelength of the optical sensor, from which the information of the target analyte can be retrieved. While the polymer coated sensors afford satisfactory sensitivity, one drawback is the lack of selectivity and specificity. To resolve this issue, an array of different polymers must be used to form a response matrix, as is widely done in the electronic nose technology [98, 110] and recently demonstrated in micro-gas chromatography [111]. The key is to form a response matrix, each row of which corresponds to a unique signature for a certain analyte. By using a set of polymers with diverse properties, such response matrix can be obtained after data calibration. The purpose of this response matrix is to identify a single unknown incoming analyte and to potentially quantify a mixture of gas analytes.

In this work, we propose a gas sensor consisting of an array of microring resonators that are used to simultaneously and rapidly obtain the response from different polymers, by coating each microresonator with a different polymer. There are two requirements for this sensor: 1) large sensitivity for individual sensing element in the

array; 2) large number of resonators in the array such that more polymers can be incorporated in the device, leading to a high rank of the response matrix and hence good

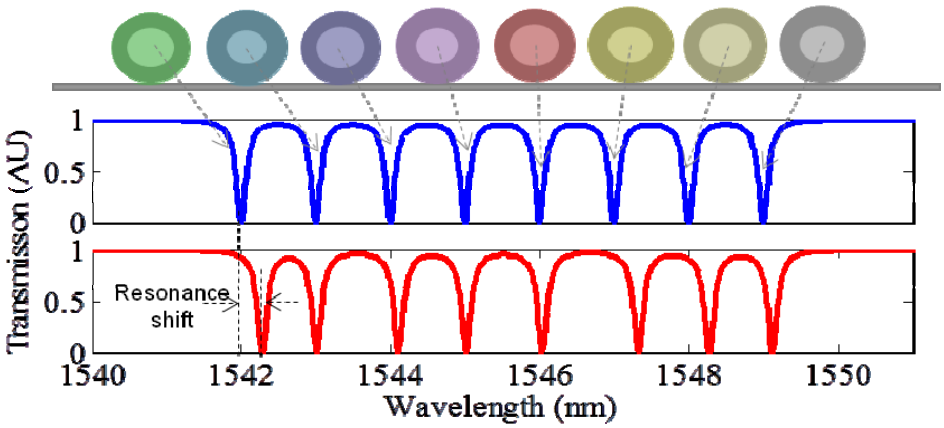

Figure 3.1 Illustration of multiplexed sensing using an array of resonators.

selectivity of the integrated sensor. This chapter is dedicated to the design, fabrication, and characterization of an integrated optical sensor for multiplexing sensing.

3.2 Design rationale of the multiplexed gas sensor

To obtain large sensitivity, microring resonators operating under TM polarization was chosen to form the array. As it is desired to include a large number of microring resonators in the sensor, the radius of each microring resonator has to be small to reach a wide free spectral range (FSR) while maintaining high Q-factor for reasonable spectral resolution. To ensure a single mode operation at TM polarization, the height and width of the microresonators are 250 nm and 700 nm, respectively. Radiation Q-factor is calculated to be ~ 477,000, which will not limit the fabrication Q-factor. The width of the straight waveguide is 500 nm.

Figure 3.2 (a) is an SEM of the designed microring resonators, whose inner radius is kept at 3.6 μm. The outer radii of the resonator are design to start from 4.3 μm and increase by at a step of 3 nm. This design ensures a single mode operation for TM polarization. Numerical simulation using COMSOL indicates that for a 250 nm thick

silicon microring resonator, every 3 nm variation in the outer radius leads to ~ 1.5 nm

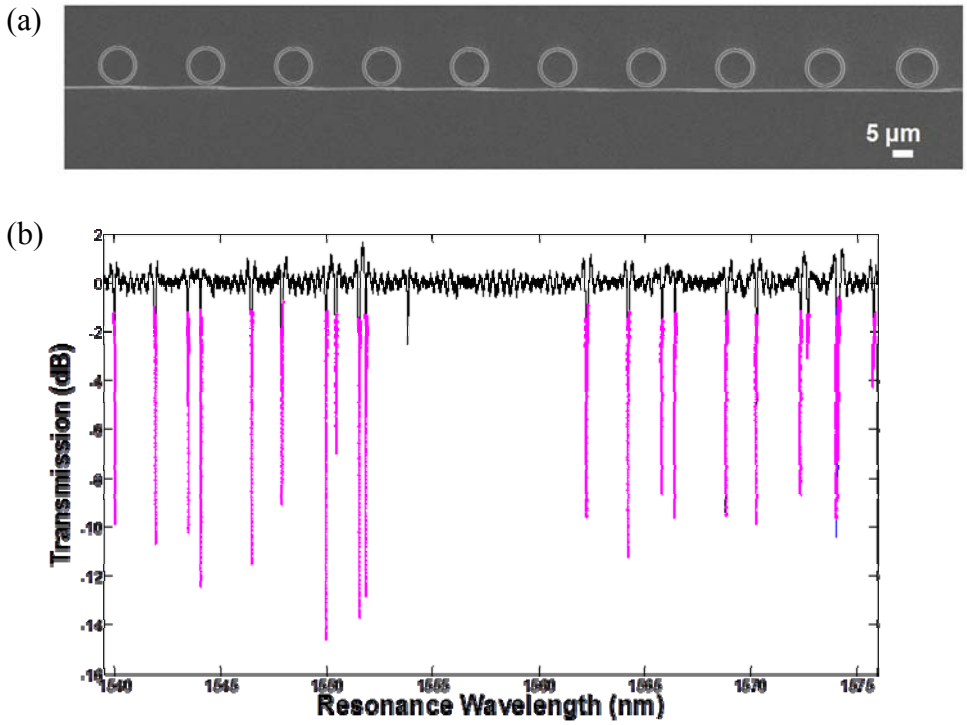

Figure 3.2 (a) SEM of an array of ten resonators; (b) Transmission spectrum of the resonator array under TM polarization.

difference in the resonance wavelength. Figure 3.2 (b) is the transmission spectrum of the resonator array, showing a large FSR of ~ 22.3 nm. The calculated FSRs are ~ 22.8 nm and ~ 25.5 nm for TM and TE polarizations, respectively. Therefore, it is confirmed that the device is working under the TM polarization. The spacing between neighboring resonators are not exactly the same as the designed values (~ 1.5 nm), due to the inevitable fabrication randomness. However, although the current array incorporate ten resonators, it still has a great potential to include even more resonators in the device. The measured Q-factors are ~ 35,000 at 1550 nm wavelength region, which is a reasonably good number to enable high spectral resolution.

Besides the resonator array for high Q-factor and large FSR, two other challenges are remaining. Firstly, to achieve the purpose of multiplexed sensing, one needs to coat

each resonator with a different polymer. Considering the small distance between the

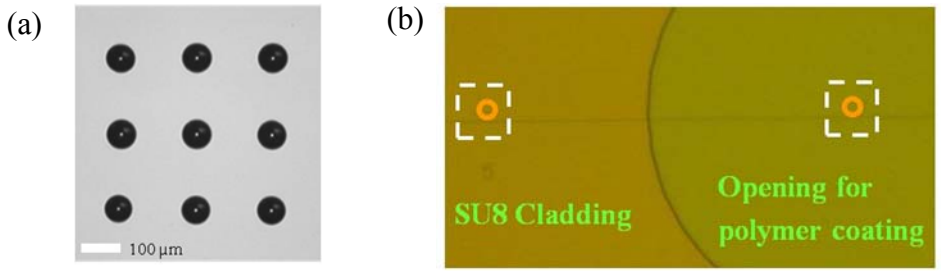

Figure 3.3 (a) A 3 by 3 array of solution drops made on a silicon substrate by the inkjet printing. The average diameter of the drops is ~ 70 µm, while the pitch is 200 µm; (b) Micrograph of two resonators, where one of them is covered by SU-8 for on-chip referencing, while the other for gas sensing.

neighboring resonators (a few hundred microns), it is very challenging to conduct the required selective coating using either spin coating, spray coating, or dip coating. To address this issue, a drop-on-demand coating approach using a commercialized inkjet printer (JetlabII, Microfab Inc.) is used. This method enables the delivery of solvent droplets containing desired polymers to a targeted position with satisfactory accuracy (± 3 µm). The formation of solvent droplets is achieved piezoelectrically, i.e., an applied voltage leads to the droplet, which will eventually drop onto the substrate at a predefined location. It is a non-contact approach, and therefore the droplets will not be contaminated by the substrate. More important, the solvent is loaded into the machine through a closed plastic reservoir, making the tool compatible with volatile organic solvents. The volume of the droplet is determined by the size of the orifice (typically 20-80 µm), applied voltage to the jetting device, and the viscosity of the solvent. By changing the surface chemistry and temperature of the substrate, the size of the drop that lands on the substrate can be controlled. Figure 3.3 depicts a 3 by 3 array of delivered solutions drops onto a silicon substrate. Excellent drop size uniformity and accurate control of positioning are clearly observed.

The second challenge is the unwanted effects of temperature variation and other environmental influences as well as any drift in the wavelength of the interrogating laser source. This issue can be alleviated by including an on-chip reference resonator in the vicinity of the sensing microresonators. As is shown in Figure 3.3 (b), the reference resonator is covered by an inert and impermeable layer of SU8-2005 to compensate for the adverse environmental effects.

3.3 Fabrication of the multiplexed gas sensor

The flow of fabrication steps is illustrated in Figure 3.4. Similar to the previously studied integrated SOI resonators, the fabrication started from an SOI wafer, with a 250 nm thick Si layer and 3 μm thick buried oxide layer underneath. Electron beam lithography was applied to define the pattern using HSQ (6%, Dow Corning) as the resist. A Cl_2 reactive ion etching dry etching step using plasma therm ICP was then performed to transfer the pattern to the silicon.

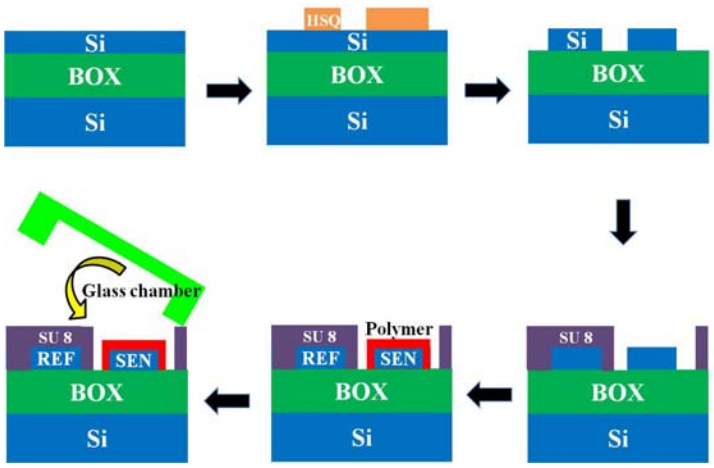

Figure 3.4 Fabrication process of the multiplexed sensor

SU8-2005 was then spun coated on the sample at 3000 rpm for 1 min, leading roughly 6 μm thick SU8 polymer on top. The dosage to pattern the openings for sensing resonators is ~ 120 mJ/cm2 (MA6 mask aligner, Karl Suss). After developing the sample

for 1 min, the sample was treated in oxygen plasma for 2 mins (Yes-R1 plasma cleaner) to remove the residual SU8 polymers on the sensing resonators.

The most critical step of fabricating this multiplexed gas sensor is the selective coating of different polymers on the sensing resonators. While the use of the JetlabII inkjet printer enables selective coating in a small area, it also limits the available solutions that can be adopted in the experiment. Specifically, three popular organic solvents, tetrahydrofuran (THF), chloroform, and dichloromethane (DCM), are not compatible with the equipment. After tests of polymer solubility (Table 3.1) and jetting repeatability, dimethyl sulfoxide (DMSO, Sigma Aldrich) and N-Methyl-2-pyrrolidone (NMP, Sigma Aldrich) proved to be better solvents in this work. All the polymers listed in this table were purchased from Sigma Aldrich and used without further purification. It is worth noting that the polymer solubility test was done at room temperature and without ultrasonic bath. The polymer should be well dissolved under this condition, otherwise it is very likely to clog the jetting device and prevent reliable and repeatable droplet formation.

Table 3.1 Solubility test at room temperature

	Water	Ethanol	Ethyl acetate	NMP	DMSO
polyvinylidene fluoride (PVF)	--	--	--	+-	+-
polycaprolactone (PCL)	--	--	--	--	++
poly 4-vinyl phenol (PVP)	--	++	++	++	++
polysulfone (PSF)	--	--	+-	--	+-
polyvinyl acetate (PVA)	--	--	++	++	++
poly ethylene-co-vinyl acetate (PEA)	--	--	--	+-	+-
poly ethyl oxide (PEO)	+-	--	--	--	--
Polyacrylonitrile (PAT)	--	--	--	+-	++

However, only solving the solubility issue by choosing polymer/solvent pair that is compatible with the equipment was not enough. As is shown in Fig 3.5(a), as soon as the DMSO droplet contacted the silicon substrate, it spread and formed a coffee-ring-like shape after the evaporation. There are two drawbacks for this pattern. First, this spreading of the droplet leads to a large area covered by the solidified polymer, making it very challenging to coat devices where neighboring sensors are close to each other without cross contamination. Second, during the formation of this coffee-ring profile, the polymer will gradually diffuse from center region to the rim of the ring. Consequently, the polymer thickness at the rim of the ring shape is much larger than that at the center, where in future the microring resonator will be located. As a result, one needs to apply a large number drops to the resonator for the desired polymer thickness. This will dramatically increase the process time needed to finish coating a single microring resonator and thus reduce the process reliability (It is required to wait until the previous drop is completely dry before applying the next drop. Increasing the number of this cycles would practically increase the probability of clogging the jetting device).

To address this issue, the sample was treated with a fluorosilane layer ((tridecafluoro-1,1,2,2-tetrahydrooctyl)1-dimethylchlorosilane, United Chemical Technologies) before the final polymer coating. To apply the fluorosilane layer, the sample first needs to be put into water saturated hexane solution after thorough cleaning (oxygen plasma treatment). Then put one drop of the silane into the solution and incubate the sample for one hour. After rinsing the sample with hexane, methanol and deionized (DI) water, bake the sample at 100 degree C for 20 mins. Figure 3.6 illustrates the difference induced by the silanization of the sample before polymer coating. The previous coffee-ring profile (3.6(a)) is replaced by the nice dome-like profile whose thickness achieves its maximum at the center region. This shape is the optimal for the microring resonator coating. Furthermore, this silanization step prevents the potential

problem that is caused by the different surface chemistries between SU8 and silicon. The diameter of the orifice used in the test was 50 μm.

Among the various tested polymers, four polymers were eventually chosen to coat on the substrate: polycarprolactone (PCL), polyvinylphenol (PVP), polyvinyl acetate (PVA), and polyacrylonitrile (PAT). They were dissolved in DMSO at a concentration of ~ 0.2 % (2 mg/ml). At such low concentration, it is necessary to apply multiple (~ 20-30) drops so that the microring resonator can be fully covered by the polymers, as is shown in Figure 3.7. Then the sample was enclosed by a glass cell made from a borosilicate square

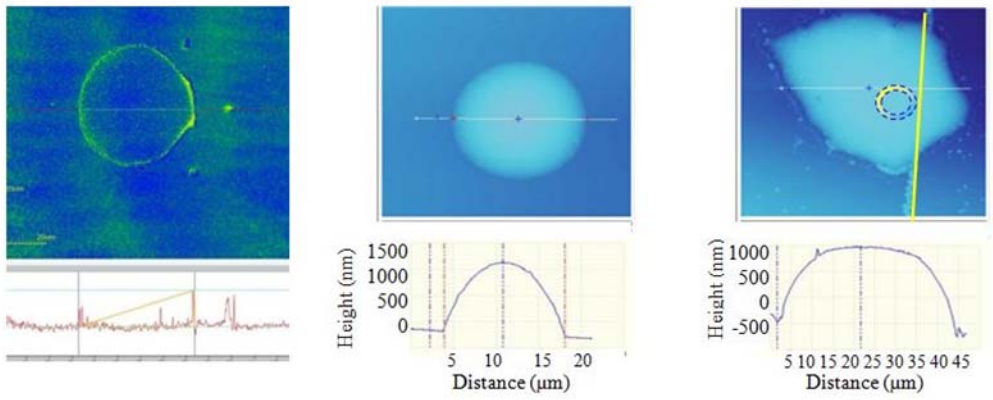

(a) (b) (c)

Figure 3.6 (a) Confocal microscopic image of a solidified PVP after a single drop onto the silicon substrate without silanization; (b) solidified PVA after a single drop on the fluorosilanized substrate; (c) solidified PVP after multiple drops to cover the optical resonator.

tubing (I.D. is 5 mm, inner wall 0.7 mm). A hole in the bottom was made before attaching the glass cell to the sample, such that the sensor was exposed to the gas analytes delivered from the input tubing. Figure 3.7 (a) is a picture showing the glass-cell-attached sample sitting on the stage before running a test.

The gas analytes at varying concentrations were prepared by mixing high purity nitrogen (UHP, Airgas) with saturated VOCs, as is shown in Figure 3.7 (b). The flow rate of the nitrogen was maintained at 100 ml/min using a flowmeter with high-resolution valve (Cole Parmer). The flow rate of incoming VOC was controlled by a syringe pump

(Harvard PHD 2000). The analyte concentration is determined by the ratio of the flow rate for nitrogen K_n and VOCs Kv, based on the following equation:

$$C = \frac{P_v}{P_A} \cdot \frac{K_v}{K_v + K_n} \quad (3\text{-}1)$$

where Pv is the saturated vapor pressure of the testing VOC for the experiment temperature, P_A is the atmospheric pressure (760 Torr). The test was run at room temperature.

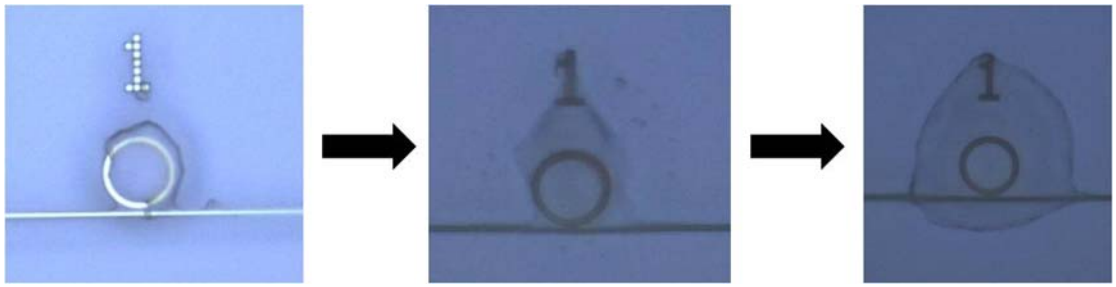

(a) (b) (c)

Figure 3.7 Confocal microscopic images of solidified PVP on a flurosilanized surface after (a) 1 drop; (b) 3 drops; (c) 20 drops

(a)

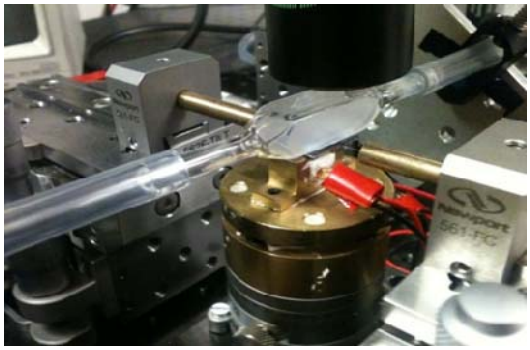

(b)

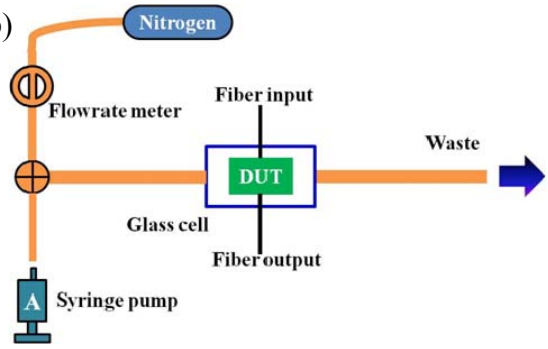

Figure 3.8 (a) Picture of the gas sensor sitting on the thermal stage after integrated with the glass gas cell; (b) Schematic of the gas analyte delivery system.

3.4 Gas sensing experiment

Figure 3.9 (a) is the micrograph of a fabricated multiplexed gas sensor consisting of six microring resonators. Four of them (#1, #3, #4, #6) are coated with different polymers, while resonators #2 and #5 are covered by SU-8 to serve as on-chip references. The diameter of the SU-8 openings is 100 μm, with a 200 μm pitch size. Figure 3.9 (b) shows the SEM of the cross section of the optical waveguide covered by thick SU-8 top cladding. The thicknesses of the silicon waveguide and SU-8 layers are 250 nm and 7 μm, respectively. The width of the waveguide is tapered down from 500 nm to 150 nm for better butt coupling coefficient from the access fiber.

The transmission spectrum of the gas sensor is shown in Figure 3.10 (a). Each resonance is labeled with its corresponding resonator number. To ensure correct mapping

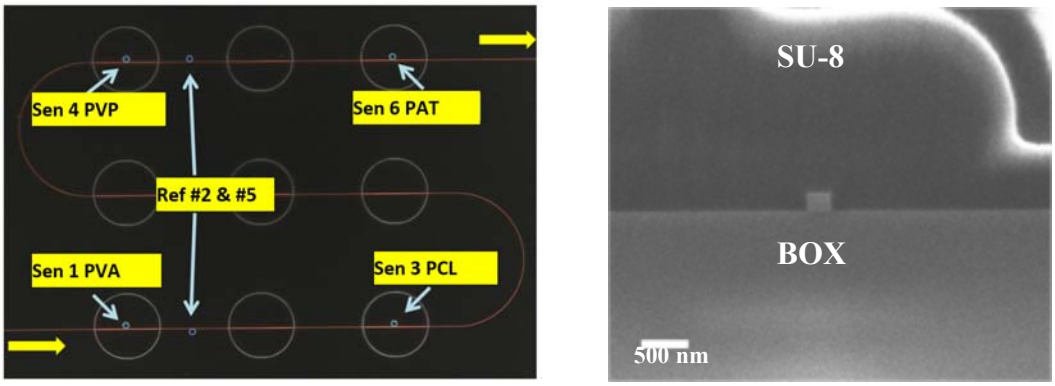

(a) (b)

Figure 3.9 (a) Micrograph of the multiplexed gas sensor; (b) SEM of the cross section of the sensor.

between each resonance in the spectrum and its corresponding resonator in the sensor, operating wavelength was tuned manually at each dip in Figure 3.10(a) to find which resonator is at resonance. As is mentioned earlier, tesonators #2 and #5 were used as on chip reference resonators to neutralize the temperature and other environmental effects. Figs. 3.11(a) and (b) are the varying resonance wavelengths of the two individual reference resonators (#2 and #5) measured at different times and conditions. It can be seen that a variation of up to 50 pm in the resonance wavelength can be observed in practice, which will significantly contribute to the measurement error. This variation was

largely due to the temperature drift during the span of testing. However, the subtraction of the two responses results into an average wavelength difference of ~ 4.60 nm, which agrees well with the design value (Note that the radius difference between resonators #2 and #5 is 9 nm, corresponding to a resonance wavelength difference of ~ 4.50 nm in theory). More importantly, a variation of only ~ ±1 pm is observed at the same period of time, as is shown in Fig. 3.11(c). This demonstrates that by using the two reference resonators #2 and #5, a measurement accuracy of ±1 pm is achievable.

Due to the different refractive indices, absorption coefficients, and even the solidified profiles of the four polymers, it is challenging to predict the Q factors and extinction ratios of the four polymer coated resonators. However, to work as a multiplexed gas sensor, the main focus is to make sure that the resonances from different sensing resonators do not overlap with each other. Figure 3.10(b)-(e) present the transmission spectrums of the four sensing resonators, all of which exhibiting high Q-factor (> 20,000) with decent extinction ratio.

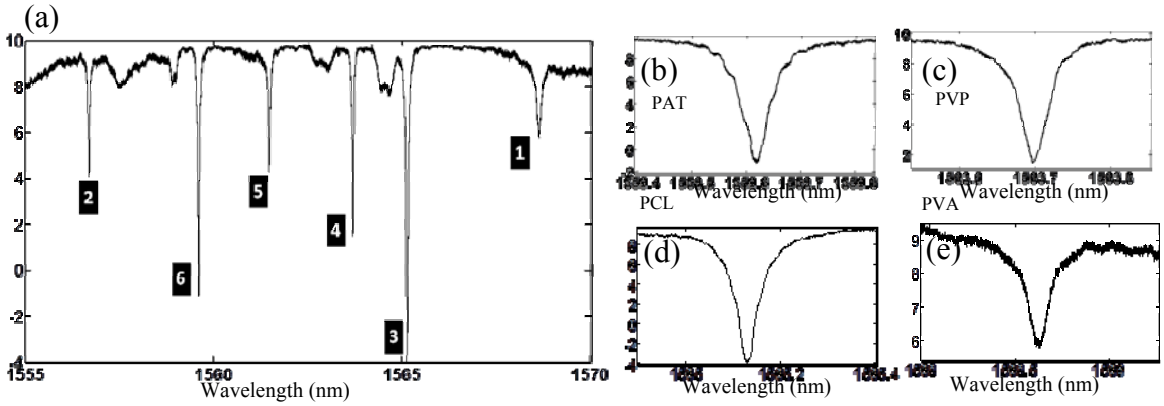

Figure 3.10 (a) Transmission spectrum of the gas sensor; (b) close-up resonance dip of the PAT coated resonator; (c) close-up resonance dip of the PVP coated resonator; (d) close-up resonance dip of the PCL coated resonator; (e) close-up resonance dip of the PVA coated resonator.

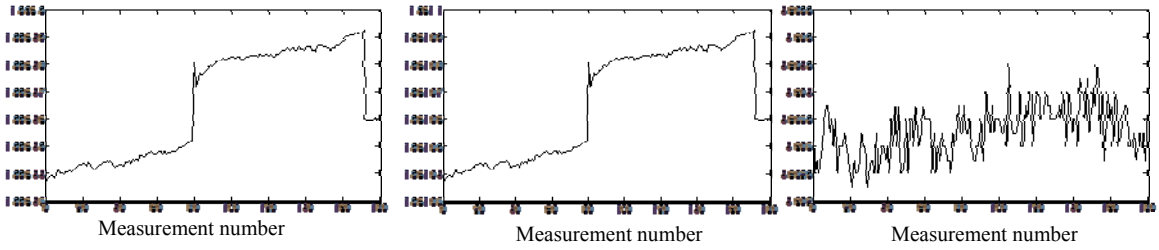

(a) (b) (c)

resonance wavelengths of reference resonators #2 and #5, respectively, varying at different times and conditions. X-axis is the measurement number. (c) The resonance wavelength difference between the two resonators, showing the cancellation of the environmental (e.g., temperature) variations.

The sensor was then integrated with a customized glass chamber before testing with gas analytes. Four volatile organic vapors, i.e., 2-pentanol, isopropanol, benzene, and toluene, were mixed with nitrogen for various concentrations and injected to the chamber. Single vapor analyte at varying concentrations was firstly injected to obtain the response pattern from the sensor. As is seen in Figure 3.12, the shift of the resonance wavelength grows proportionally with increasing analyte concentrations in all four vapors. The

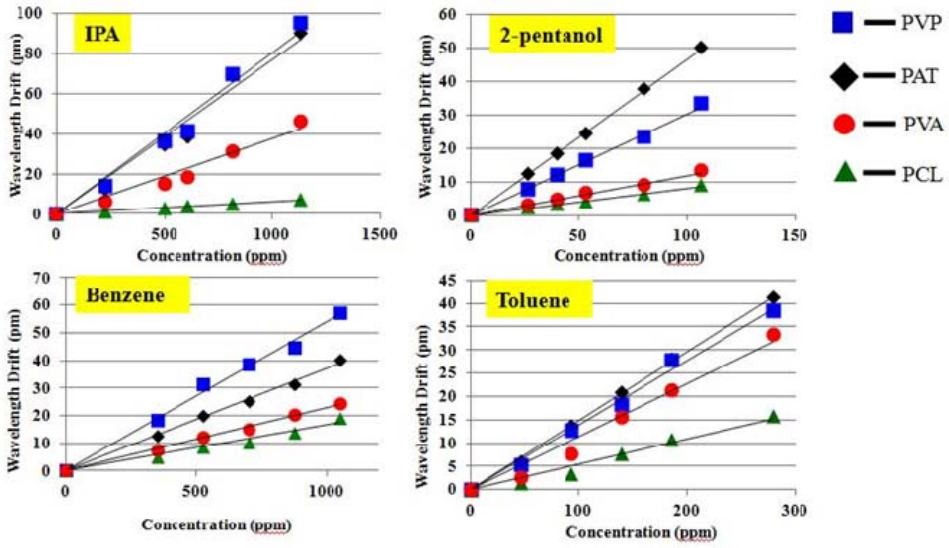

Figure 3.12 Wavelength drift of the four sensing resonators exposed to four VOCs at varying concentrations.Figure 3.11 (a) and (b) Measured

response is linear for the anlayte concentrations of interest. With the spectral resolution assumed to be 1 pm, the limits of detection are 2.1 ppm, 6.8 ppm, 11.3 ppm, and 18.3 ppm for 2-pentanol, toluene, IPA and benzene, respectively (Table 3.2).

Table 3.2 Limit of detections for four VOC vapors with four polymers

Detection limit	IPA (ppm)	2-Pentanol (ppm)	Benzene (ppm)	Toluene (ppm)
PVP	12.5	3.3	18.9	6.8
PAT	13.1	2.1	27.0	7.2
PVA	27.0	8.4	45.5	8.8
PCL	166.7	12.3	62.5	18.5

.

Figure 3.13 is the response pattern of the four vapors in terms of the normalized sensitivities, illustrating the diversity of the sensor. PVP shows the largest sensitivity for three of the incoming vapors, i.e., IPA, Benzene, and Toluene, while PAT leads to the largest sensitivity toward 2-pentanol. The response patterns of various incoming VOCs are clearly different, leading to the desired selectivity.

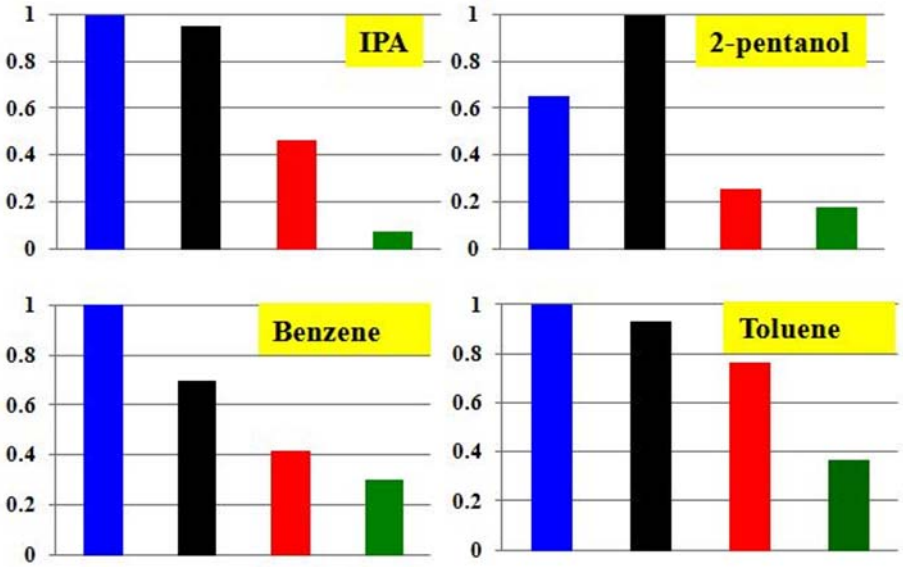

Figure 3.13 Response patterns of the four vapor analytes normalized by the maximal sensitivity. (Blue-PVP, Black-PAT, Red-PVA, Green-PCL)

Furthermore, vapor mixtures were then sent into the gas chamber with nitrogen as the carrier gas. The dash lines in Figure 3.14 are the predicted response based on the calibration data, which agree well the experiment results shown in solid circles, meaning that the linearity and superposition nature of the sensor is confirmed. In this test, 225 ppm of IPA was first injected into the glass cell, followed by an addition of 525 ppm of Benzene. The resonance wavelengths of all the four polymer coated resonators were all redshifted accordingly. Good reversibility was observed when Benzene and IPA were stopped in the process, and the resonance wavelengths of all the resonators returned to their baseline. Afterwards, a combination of 500 ppm IPA and 53 ppm of 2-pentanol was injected. Again, excellent linearity and superposition property were observed.

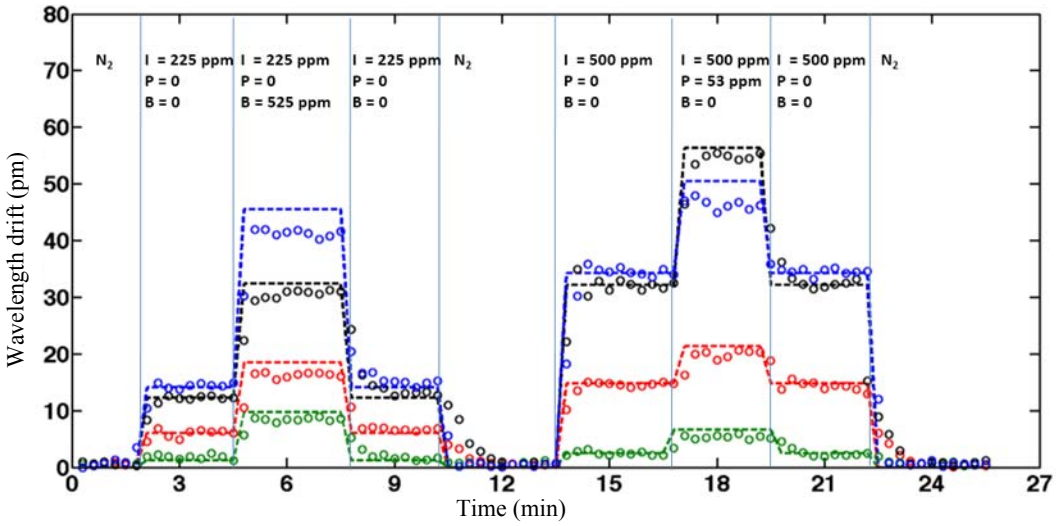

Figure 3.14 Time evolution of the sensor wavelength drift when vapor mixtures are injected into the gas chamber. (Blue-PVP, Black-PAT, Red-PVA, Green-PCL) Dash line indicates the expected value based on calibration data, while solid circles are experimental results.

CHAPTER 4

ON-CHIP SPECTROMETER WITH ARRAYED SOI MICRODONUT RESONATORS

In this chapter, a miniaturized on-chip spectrometer is demonstrated on an SOI platform. By using an array of microdonut resonators, high resolution and large operating bandwidth are obtained simultaneously. The design, fabrication and characterization of the device are presented.

4.1 Motivation

Integrated photonic sensors have received considerable attention in recent years due to their inherent advantages, including high sensitivity, low cost of fabrication, versatility, compactness, and low power consumption. The progress of integrated photonic sensors has reached the point that requires integration of different system components together for an overall efficient sensing system. One of the major building blocks for such lab-on-a-chip sensing systems is an integrated spectrometer that enables on-chip spectral analysis.

An ideal on-chip spectrometer needs to following requirements: 1) high spectral resolution; 2) broad operating bandwidth; 3) small footprint; 4) ease of integration; and 5) low power consumption.As is mentioned in Chapter 1, there has been significant progress in the realization of integrated microspectrometers in different configurations over the past few decades, including arrayed-waveguide gratings, grating spectrometers, and superprism-based spectrometers. Their dependence on the dispersive component leads to a trade-off between the size of the structure and the spectral resolution. That is, long length (on the order of cm) of optical waveguides are needed to achieve high spectral resolution.

Meanwhile, travelling-wave microresonators have been known for providing high Q factor, and thus excellent spectral resolution. The operating bandwidth is determined by the FSR of the device, which needs to be miniaturized to achieve large FSR. Therefore, by careful design and fabrication, they can be great candidates for building an on-chip microspectrometer. In this thesis, I propose a new microspectrometer architecture based on a large array of compact microdonut resonators to address the challenges of existing on-chip spectrometers. The key building element used to construct the microspectrometer is a miniaturized microdonut resonator [112] offering single mode operation with a high Q factor and a large FSR. While the high Q factor enables the high spectral resolution, the large FSR leads to broad operating bandwidth.

The proposed spectrometer employs a filter array of microdonut resonators, which is coupled to an input bus waveguide, as is schematically shown in Figure 4.1(a). The microdonut resonators are carefully designed such that each of the resonators only taps a small portion of the incoming spectrum that overlaps with its resonance lineshape, as is shown in Figure 4.1(b). In this architecture, each resonator corresponds to a unique spectral channel. The input signal power in each spectral channel can be coupled to a separate output waveguide or directly coupled out of plane through the resonator. By imaging the output power of different spectral channels using a detector array or a charge-coupled detector (CCD) chip on top of the resonator array device, the entire input signal spectrum can be measured in real time. This on-chip spectrometer is fabricated using CMOS-compatible manufacturing techniques and thus can be readily integrated with integrated sensors, optoelectronics, microelectronics and microfluidic channels. This enables the realization of a system-on-a-chip suitable for several applications in biological, chemical, medical, and pharmaceutical industries.

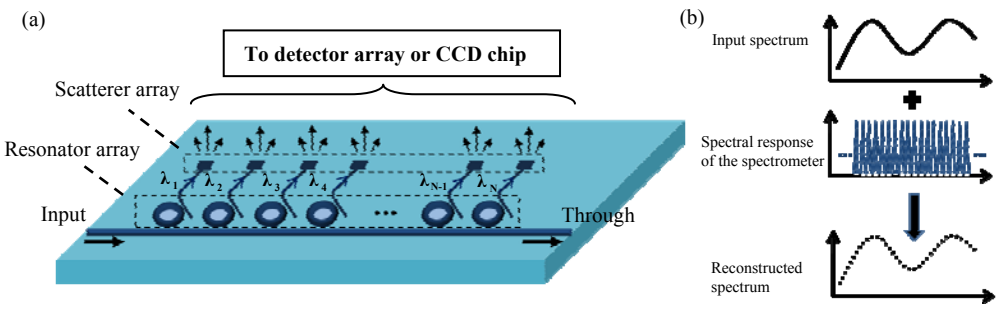

Figure 4.1 (a) Configuration of the resonator-array spectrometer: a 1-D array of small microdonut resonators samples different spectral channels of the input signal propagating in the bus waveguide. Each spectral channel is coupled by one resonator to a corresponding drop waveguide and then scattered out-of-plane in an arrangement prepared for a detector array on top of the structure. (b) Working principle of the resonator-array spectrometer: the unknown input spectrum is sampled by the series of resonances provided by the resonators in the array followed by data processing to obtain the reconstructed spectrum of the input signal.

4.2 Microdonut resonators

To simultaneously achieve a high Q factor and a large FSR, a miniaturized microdonut resonator is used. As shown in Figure 4.2(a), a microdonut resonator is essentially a microdisk with an inner hole perforated at the center. In this configuration, the fundamental radial mode of the resonator is mostly confined around the outer perimeter of the microdonut (see Figure 4.2(c)) while the higher-order radial modes are pushed into the leaky zone, leading to a single-mode operation. The major difference between the microdonut resonator and the miniaturized microring resonator is that by adjusting the radius of the inner hole, the fundamental radial mode of a microdonut resonator interacts only with the outer sidewall of the resonator, while such a mode always interacts with two sidewalls in microring resonators. Consequently, a higher quality factor for the fundamental mode is expected when using microdonut resonators. Figure 4.2(a) shows the scanning electron microscope (SEM) image of an add/drop filter based on the compact microdonut resonator with a radius of ~ 2 μm and an oxide cladding. A linewidth of ~ 50 pm is measured from the drop port transmission for TE

polarization (i.e., electric field confined in the plane of the device) (see Figure 4.2(b)), leading to a loaded Q factor (Q_L) of ~ 30,000 (corresponding to an intrinsic Q factor of Q_i ~ 80,000). This Q_i is twice that achieved with microring resonator with a similar diameter. Figure 4.2(c) confirms the single-mode operation of the miniaturized microdonut resonator with an FSR of ~ 57 nm.

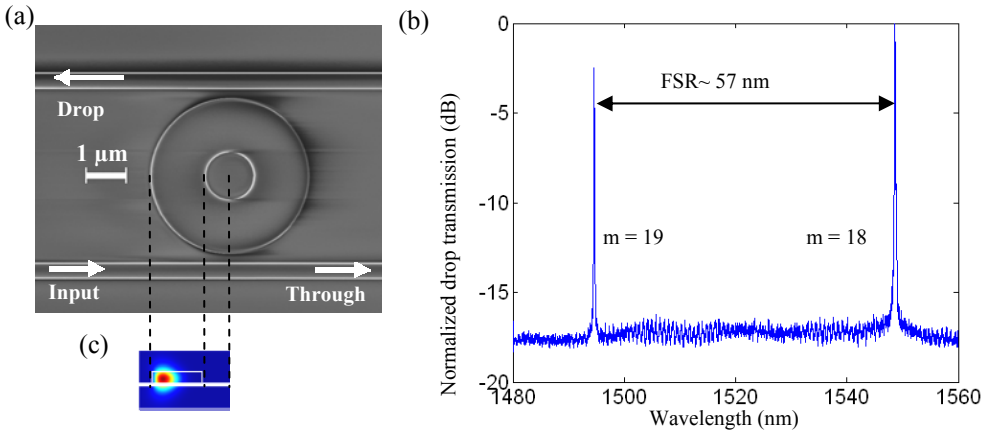

Figure 4.2 (a) The SEM image of a microdonut resonator in an add/drop configuration: the width and thickness for both waveguides are 400 nm and 230 nm, respectively. The outer radius of the microdonut resonator is r_{out} = 1.97 μm with a center hole with a radius of r_{in} = 0.6 μm. The gap between the waveguide and the resonator is 240 nm. The microdonut resonator has a 2 μm thick oxide cladding layer. (b) The experimental transmission spectrum of the drop port of the resonator in Part (a) for TE polarization showing two resonances belonging to the fundamental radial modes with different azimuth mode numbers (m) specified in the figure. The measured linewidth is ~ 50 pm and the FSR is ~ 57 nm. (c) Simulated fundamental TE mode profile of the microdonut resonator with m=18, indicating a majority of light is confined at the outer perimeter of the resonator.

By engineering the geometry of the microdonut resonator (i.e., the outer and inner radii), its resonance wavelength can be adjusted. Because of the small mode volume and high field intensity of the resonant mode at the outer perimeter (see Figure 4. 2(c)), the resonance is very sensitive to the variations of the outer radius. Simulations using three-dimensional finite element method (3D FEM) show that every 1 nm variation in the outer radius of a microdonut with a radius of r_{out} ~ 2 μm and a thickness of 230 nm corresponds

to a 0.6 nm change in its resonance wavelength near 1550 nm. Meanwhile, the fine-tuning of the resonance (better than 10 pm wavelength accuracy) can be achieved by adjusting the inner radius of the microdonut resonator. The spectral linewidth of the resonance (and thus its Q_L) is controlled by engineering the coupling between the bus waveguide and the microdonut resonator. Therefore, combined with the high Q_i and large FSR, the ability to independently tune the resonance location and spectral resolution makes the microdonut resonator an excellent building-block device to construct a large-scale resonator array suitable for on-chip spectroscopy.

4. 3 Design and fabrication of on-chip spectrometer with microdonut resonators

The micrograph of an on-chip resonator-array spectrometer composed of an array of resonators side coupled to a bus waveguide is shown in Figure 4.3(a) [113]. The spectrometer is designed to work with TE polarization. The input light signal (with a target spectrum to be detected) is coupled through the bus waveguide from the lower left in Figure 4.3(a). Each of the resonators filters the input signal in a narrow spectral window and sends it via its corresponding side coupled drop waveguide to a scatterer located at the end of the drop waveguide. In this architecture, each resonator, its drop waveguide and the corresponding scatterer describe a spectral channel that measures a unique spectral portion of the target spectrum. The response of each spectral channel is indicated by the out-of-plane radiation from the scatterer of that channel, and it is measured by imaging the signal from the scatterer array onto a detector array, as shown in Figures 4.3(b)-(d).

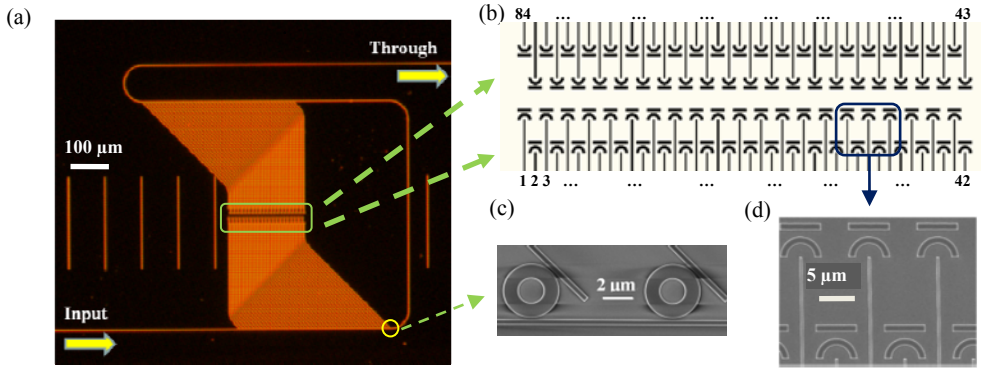

Fig. 4.3. (a) Micrograph of the proposed spectrometer: incoming light is coupled to the structure through the input waveguide on the lower left of the figure. Each of the resonators is side coupled to the input waveguide from one side and to a drop waveguide from the other side to filter the input signal in a narrow spectral window. The filtered signal is scattered out of the chip by a scatterer at the end of the drop waveguide. (b) The 2-D array of the scatterers with channel numbers labeled. (c) The SEM image of two microdonut resonators coupled to the input waveguide and their corresponding drop waveguides. The center-to-center distance between the two adjacent microdonut resonators is 10.0 µm, the gap between the microdonut and each waveguide is 130 nm, and the widths of the input and bus waveguides are 400 nm. (d) The SEM image of a portion of the 2-D array of the scatterers.

The number of the resonators in the array and their resonance wavelengths and linewidths are adjusted to cover one full FSR of a single resonator. Tuning of the resonance wavelength is achieved by varying the outer radius (initially ~ 2 µm) with 1 nm steps, while keeping the inner radius fixed at 0.9 µm to ensure the single-mode operation at around 1550 nm. This leads to a ~ 0.6 nm increment in the resonance wavelengths of adjacent spectral channels as calculated from 3D FEM in the COMSOL environment. Considering an FSR of ~ 60 nm, the operating bandwidth is designed to be ~ 50 nm to avoid the interference of resonances from different azimuthal modes. A total number of 84 microdonut resonators are needed to cover the operating bandwidth without too much overlap among the neighboring resonances. The outer radii of the resonators are chosen ranging from 1.950 µm to 2.033 µm.

The resonance linewidth of the resonators is set to be ~ 0.3 nm, corresponding to a Q_L ~ 5000. This linewidth is achieved by setting the gap size between the resonators and the bus waveguide to 130 nm. According to 3D FEM calculations, the effective coupling Q factor of Q_C is ~ 10,000. (Figure 4.4) Considering the two coupling regions (corresponding to the input and the drop ports) as well as the much higher intrinsic quality factor Q_i of the microdonut resonator, the estimated loaded Q_L would be ~5000 ($1/Q_L = 2/Q_C + 1/Q_i \approx 2/Q_C$). In this configuration, the spectrometer samples the incoming target spectrum with 84 sharp Lorentzian-like peaks with a constant spacing of ~ 0.6 nm as schematically shown in Figure 4.1(a). The width of the straight waveguide is chosen to be 400 nm to ensure single mode operation at the wavelength region of 1500 nm-1640 nm. The drop waveguides are designed to uniformly and efficiently transmit the spectrum channel light energy to the scatterers. To ensure that all the scatterers fall within the field-of-view of the CCD, the drop waveguides and their scatterers are packed in the center (from the top and bottom) of the device as shown in Figures 4.3(a) and 4.3(b). This leads to a small size for the 84-element scatterers array (~ 200 μm by 50 μm in total) that can be readily imaged within the field-of-view of the CCD using a 20x objective lens. The scatterers are placed in a 2D array, where the scatterers with different parities are located in different rows, as shown in Figure 4.3(b). Therefore, one scatter of a certain channel is always placed in a different row from both of its immediate neighbor channels. This helps to lower the crosstalk among the neighboring channels and to easily identify the channel number in the spectrum estimation.

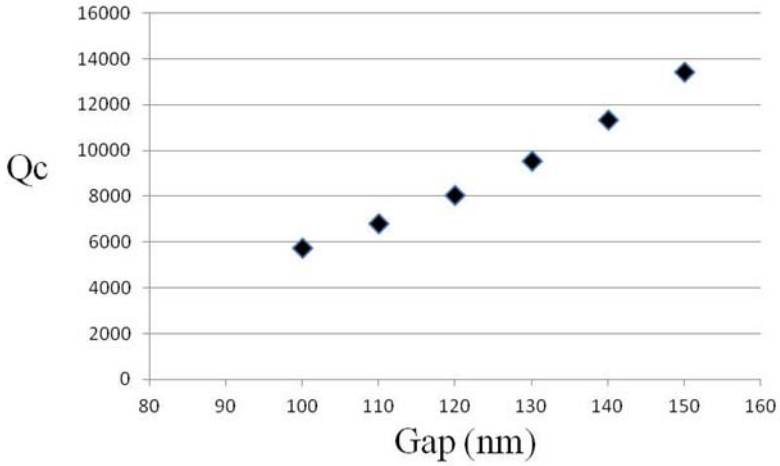

Figure 4.4 Coupling Q-factor as a function of the gap size between the microdonut resonator and the straight waveguide.

The spectrometer structure was fabricated on an SOI wafer with a Si layer thickness of 230 nm on top of a 1μm buried oxide layer (Figure 4.5). The device was patterned using a JBX-9300FS electron beam lithography (EBL) system with 6% dilute hydrogen silsesquioxane (HSQ) negative electron resist and etched in an inductively-coupled plasma etching system with Cl_2 chemistry. The dosage for the HSQ writing is ~ 3650 μc/cm^2. A 1 μm thick layer of SiO_2 is subsequently deposited on top of the structure using plasma enhanced chemical vapor deposition (PECVD) as the cladding and passivation layer.

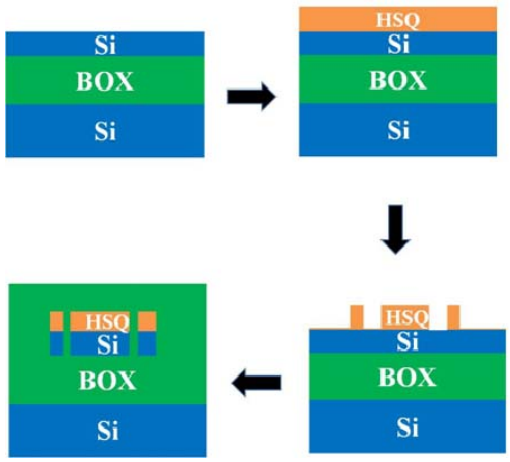

Figure 4.5 Fabrication flow of the on chip spectrometer

4.4 Experimental results

The characterization of the spectrometer is first conducted by coupling light from a tunable laser (81640A, Agilent Technologies) to the input bus waveguide via a tapered fiber. The output power of the through port is collected by a photodetector (Thorlabs PDB 150C) through another tapered fiber. The measured transmission spectrum from the through port (see Figure 4.3(a)) waveguide is shown in Figure 4.6 (a). The FSR of the

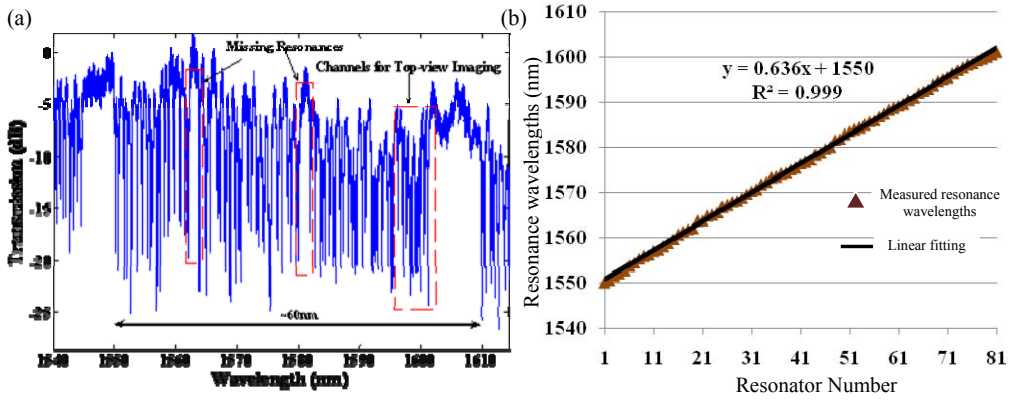

Figure 4.6 (a) Transmission spectrum measured from the through port waveguide, indicating an FSR of ~ 60 nm. (b) Plot of the measured resonance wavelengths of different resonators (vertical axis, y) versus their resonator number in the resonator array (horizontal axis, x, x=1-81, which only include the working 81 resonators with observed resonances). The inset formula shows the linear functions fitted to the measured resonance wavelengths. The correlation between the measured data points and the fitted linear model (R^2) is 0.999.

smallest microdonut resonator (outer radius ~ 1.950 μm) is measured to be ~ 60 nm, which corresponds to the resonance wavelength spacing between the azimuth modes m=17 and m=18 of the fundamental radial TE mode. The resonances of the resonator array densely fill up the FSR, indicating the capability of sampling a target spectrum. However, among the total 84 microdonut resonators in the array, three of the designed resonances are missing and a total of 81 resonances are observed in both the through port transmission and the top view IR camera imaging that will be discussed later. For the functioning 81 channels, the typical value of the measured loaded Q is Q_L ~ 5000, which

is in good agreement with the original design. Figure 4.6(b) plots the measured resonances of the resonator array obtained directly from Figure 4.6(a), showing the channel-to-channel uniformity of the 81 resonances. The measured resonance spacing varies between ~ 0.2 nm and ~ 1.0 nm, due to the high sensitivity of the resonance wavelength to changes in the outer radius of the microdonut resonators, the imperfections in the device fabrication, and possibly the thickness variation of the wafer. The solid line and the inset formula in Figure 4.6 (b) show the linear regression model obtained by the measured data points. The shift of the measured resonances from their projected values with the linear fitting model is depicted by the standard error of ~ 0.400 nm. The good linearity with an average resonance spacing of ~ 0.636 nm agrees well with the design value of ~ 0.6 nm.

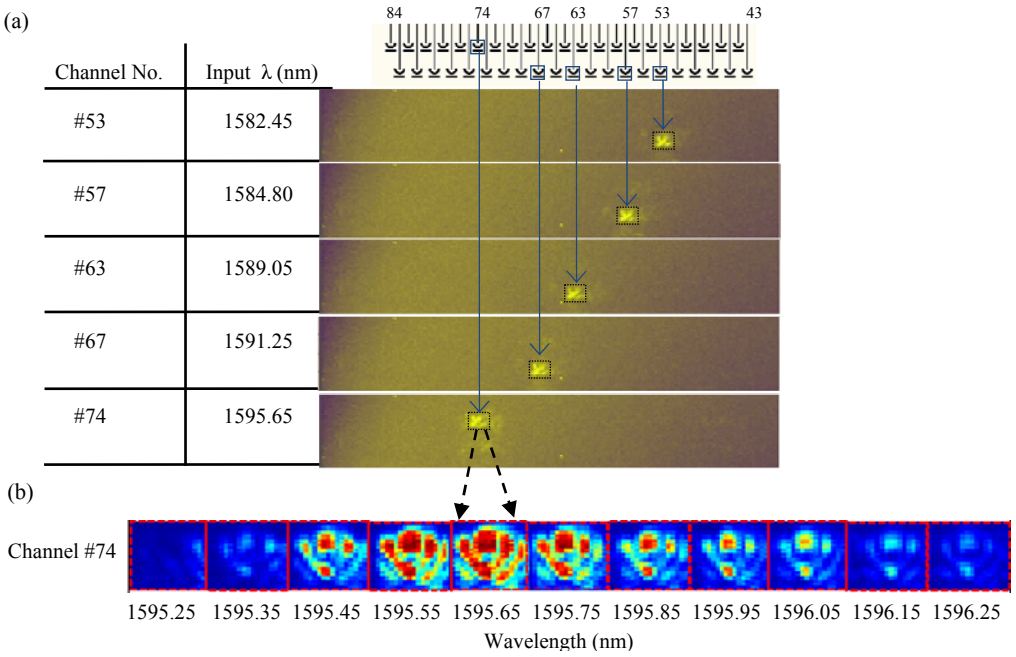

Figure 4.7 (a) Real time images captured by the IR camera showing different channel responses at five different input wavelengths (nm): 1582.45, 1584.80, 1589.05, 1591.25, and 1595.65, when the input spectrum falls within channel numbers 53, 57, 63, 67, 74, respectively. Note that this figure only shows the upper portion of the scatterer array. (b) Post-processed light pattern scattered by channel #74 at different input wavelengths around its resonance.

The response of the spectrometer is then characterized by capturing the out-of-plane radiation of the scatterer array with an IR camera (Sensors Unlimited SU128-1.7RT, 128 by 128 pixels with pixel size of 60 μm^2), while varying the input wavelength using a tunable laser (81640A, Agilent Technologies) at 500 μw output power. During the full wavelength scan over one FSR from 1550 nm to 1610 nm at a step of 0.05 nm, 81 out the total 84 scatterers turned on (with strong out-of-plane radiation observed in the real time imaging). The remaining three resonators are not observed either in the transmission or in the out of plane image. With the transmission spectrum and the location of the scatterers that failed to turn on, the defective channels were identified with resonator numbers #20, #21, and #50. This can be due to the large shift of the resonance of these three channels as a result of fabrication imperfection causing them to overlap with adjacent resonances; it can also be due to unwanted large imperfection resulting in low intrinsic *Q*s for these three resonators. Figure 4.7(a) shows the top images of the upper portion of the scatterer array at different input wavelengths, corresponding to the designed channels #43 - #84. The top image of the scatterer corresponding to the spectral channel #74 for different input wavelengths is shown in Fig. 4.7(b). We can clearly see the total scattered power peaks at 1595.65 nm, which corresponds to the assigned center resonance wavelength for this channel. Good extinction ratio is also observed within ~ 0.5 nm from the center wavelength as shown in Figure 4.7(b). By integrating the amplitudes of the CCD pixels for each channel at different input wavelengths, the spectral response of each spectral channel of the spectrometer can be obtained and used for the calibration purpose. Figure 4.8(a) is the calibrated spectral response of the 13 channels (#72 - #84). In this figure, the output of each channel has been normalized to its peak value. The variation of the peaks of the 13 channels is measured to be within ~ 1.5 dB, showing good power uniformity among different channels of the spectrometer. The nonlinear response of the IR camera to different values of the light intensity is not corrected in Figure 4.8(a). Therefore, the spectral line shape of each spectral channel is a little broadened in this figure.

The comparison between the extracted resonances from the calibration spectrum and those obtained directly from the through port transmission measurement is shown in Figure 4.8(b). A good agreement is observed over the 13 channels under discussion, verifying the reliability of the post-processing method. By fitting the data with a linear function, the average deviation of the cavity resonances from the designed values for this short wavelength range of the 13 adjacent channels is ~ 0.176 nm, a value much smaller than the ~ 0.400 nm obtained for the whole FSR covering 81 channels. We believe the smaller local variation in the resonances of these 13 adjacent spectrum channels is mainly caused by the fabrication imperfections, while the thickness variations of the device layer in the SOI substrate contribute to the larger deviation measured in the long range shown in Figure 4.8(b).

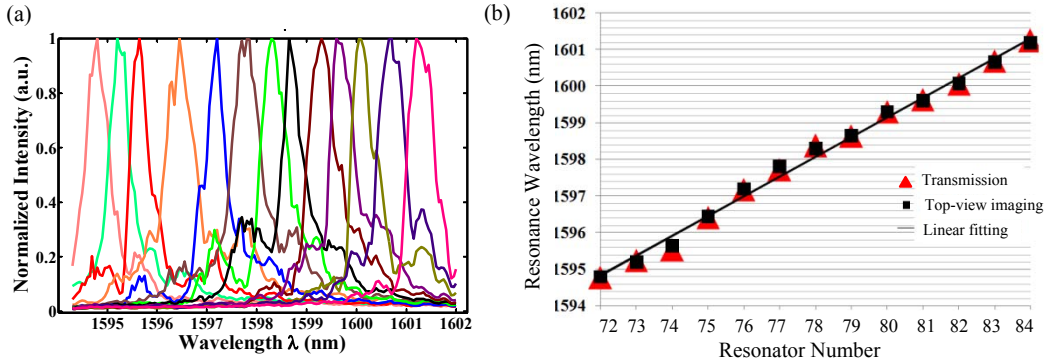

Figure 4.8 (a) Calibration spectrum of the 13 channels covering the wavelength range from 1594.30 nm to 1602.00 nm; (b) comparison of resonances obtained by the through port spectrum (triangles) and the calibration spectrum based on the top-view images (squares). A linear model is fitted to the measured resonance wavelengths. The standard deviation of the resonance wavelengths from the linear model is only 176 pm.

The demonstrated high resolution (~ 0.6 nm) microspectrometer can be very compact thanks to the small size of the miniaturized microdonut resonators and the scatterers. Although the current footprint of this spectrometer is ~ 1 mm^2, a large portion of the real estate on-chip is occupied by the passive waveguides, which transport the filtered spectral channel signals from the drop port to the scatterer array. Therefore, the

size of the spectrometer could be further reduced through suitable optimized device designs for the scatterer array and the drop port waveguides.

One key advantage of the demonstrated spectrometer is the capability of independently controlling and configuring the resolution and the operating bandwidth of each channel of the microspectrometer for different applications. The resolution is well controlled by engineering the coupling between the resonator and the bus waveguide. By implementing different sets of resonator arrays in parallel, the operating bandwidth can be extended to more than one FSR. Ultimately, the spectral range of operation of this microspectrometer is limited by the material absorption of Si as the device layer and SiO_2 as the cladding and buffer layer. Therefore, the proposed spectrometer can cover a wide range of wavelengths from ~1.1μm to ~3 μm. The main limitation on the spectral resolution is the degree of control on the radii of microdonut resonators. Since the intrinsic Q factor is very high (~ 80,000 for a 2 μm radius) and can be further improved by fabrication optimization, the ultimate limit on resolution (assuming full control on the resonator sizes) is very high. This makes the proposed spectrometer a unique device for a wide range of practical applications.

The low insertion loss in this structure not only enables efficient use of the incident optical power, but also maintains uniform power distribution of the signal among different channels, which has been verified by the measured power variation of ~ 1.5 dB. The main challenges are the shift of the resonances due to the variation of the thickness in the wafer scale and the fabrication imperfections. The former can be solved by further reducing the area of the device, while the latter could be addressed by post-fabrication trimming. Moreover, unlike the case in wavelength demultiplexers, data processing techniques used in the spectrum reconstruction can relax the requirements for the spectral response of the spectrometer. The compatibility of the fabrication processes to the CMOS process enables the integration of these spectrometers with microelectronic and

microfluidic circuitry to develop integrated sensing systems for various applications in biological, chemical, medical, and pharmaceutical industries.

CHAPTER 5

CONCLUSIONS

The final chapter concludes my research works in developing essential building blocks for a photonic lab-on-a chip system on a SOI platform. Section 5.1 summarizes the technical contributions. Future research directions related to this work are presented in Section 5.2.

5.1 Technical Contributions

This dissertation studies several material platforms and new device designs to improve sensitivity and selectivity. The contributions are summarized as follows.

5.1.1 Sensitivity enhancement by incorporating porous materials

a. Develop and optimize a reliable process to integrate magnesiothermic reduction based pSi with the SOI platform to achieve 6-fold sensitivity enhancement without sacrificing the spectral resolution of the sensor. Therefore, the overall limit of detection is significantly improved.
b. Demonstrate the integration of PAAM based pSi with an SOI platform, enabling better flexibility in terms of pore size and porosity while maintaining the high sensitivity. This device is able to be tailored for the detection of bioanalytes with various sizes.
c. Demonstrate a porous titania clad SiN microresonator sensor showing excellent sensitivity.

5.1.2 Multiplexed gas sensors on an SOI platform

Improvement of selectivity by the demonstration of a miniaturized, multiplexed gas sensor by developing a reliable process for high precision and selective drop coating

of various polymers onto SOI substrates. Four polymers have been multiplexed for four VOC analytes.

5.1.3 High resolution on-chip spectrometer

Demonstration of an 81 channel on-chip spectrometer with high spectral resolution (0.6 nm) and large bandwidth (60 nm) on the SOI platform.

5.2 Future research directions

5.2.1 Highly sensitive microring resonators at visible wavelength

Since titania and silicon can both work at visible wavelength. The demonstration of integration between porous titania and silicon nitride microresonators has paved a way for the development of a similar device operating at visible wavelengths, where many low cost light sources and detectors are currently available.

5.2.2 pSi clad silicon nitride resonators for high sensitivity detection

Although all the pSi clad sensors are demonstrated on an SOI platform, our approach of integrating the pSi films does not only apply to an SOI substrate. In fact, both the magnesiothermic reduction based pSi realized via FOx and the PAAM based pSi can be readily applied to a silicon nitride platform with better thermal stability than the current SOI platform.

5.2.3 Highly selective integrated gas sensor

What has been demonstrated in this work is a successful process that paves the way to develop an integrated gas sensor that can be equipped with more than ten functional polymers to significantly improve the selectivity of the device. We envision that an extensive research on polymer-gas interaction would lead to an optimal selection of the polymer set that can be tailored to different applications.

5.2.4 On-chip spectrometer with higher resolution, larger operating bandwidth and better uniformity

We envision that by careful design and extensive research on post fabrication trimming techniques, on-chip spectrometers with larger bandwidth and better uniformity are well within reach.

REFERENCES

1. C. D. Chin, V. Linder, and S. K. Sia, "Lab-on-a-chip devices for global health: past studies and future opportunities," Lab Chip **7**, 41-57 (2007).
2. A. Rios, M. Zougagh, and M. Avila, "Miniaturization through lab-on-a-chip: Utopia or reality for routine laboratories? A review," Anal Chim Acta **740**, 1-11 (2012).
3. Z. X. Xia, Y. Chen, and Z. P. Zhou, "Dual waveguide coupled microring resonator sensor based on intensity detection," Ieee J Quantum Elect **44**, 100-107 (2008).
4. H. C. Morris, M. Damon, J. Maule, L. A. Monaco, and N. Wainwright, "Rapid culture-independent microbial analysis aboard the international space station (ISS) stage two: quantifying three microbial biomarkers," Astrobiology **12**, 830-840 (2012).
5. G. M. Whitesides, "The origins and the future of microfluidics," Nature **442**, 368-373 (2006).
6. S. Haeberle, and R. Zengerle, "Microfluidic platforms for lab-on-a-chip applications," Lab Chip **7**, 1094-1110 (2007).
7. K. Ren, J. Zhou, and H. Wu, "Materials for microfluidic chip fabrication," Accounts of Chemical Research **46**, 2396-2406 (2013).
8. A. L. Washburn, and R. C. Bailey, "Photonics-on-a-chip: recent advances in integrated waveguides as enabling detection elements for real-world, lab-on-a-chip biosensing applications," Analyst **136**, 227-236 (2011).
9. O. S. Wolfbels, "Fiber-optic chemical sensors and biosensors," Anal Chem **80**, 4269-4283 (2008).
10. N. Jokerst, M. Royal, S. Palit, L. Luan, S. Dhar, and T. Tyler, "Chip scale integrated microresonator sensing systems," Journal of Biophotonics **2**, 212-226 (2009).
11. J. F. Song, X. S. Luo, J. S. Kee, K. Han, C. Li, M. K. Park, X. G. Tu, H. J. Zhang, Q. Fang, L. X. Jia, Y. J. Yoon, T. Y. Liow, M. B. Yu, and G. Q. Lo, "Silicon-based optoelectronic integrated circuit for label-free bio/chemical sensor," Opt Express **21**, 17931-17940 (2013).
12. J. F. Liu, D. Pan, S. Jongthammanurak, K. Wada, L. C. Kimerling, and J. Michel, "Design of monolithically integrated GeSi electro-absorption modulators and photodetectors on an SOI platform," Opt Express **15**, 623-628 (2007).
13. M. Lipson, "Guiding, modulating, and emitting light on silicon - Challenges and opportunities," J Lightwave Technol **23**, 4222-4238 (2005).
14. M. Baaske, and F. Vollmer, "Optical resonator biosensors: molecular diagnostic and nanoparticle detection on an integrated platform," Chemphyschem **13**, 427-436 (2012).
15. M. S. Luchansky, and R. C. Bailey, "High-Q optical sensors for chemical and biological analysis," Anal Chem **84**, 793-821 (2012).
16. C. Y. Chao, and L. J. Guo, "Design and optimization of microring resonators in biochemical sensing applications," J Lightwave Technol **24**, 1395-1402 (2006).
17. I. M. White, and X. D. Fan, "On the performance quantification of resonant refractive index sensors," Opt Express **16**, 1020-1028 (2008).
18. M. E. Germain, and M. J. Knapp, "Optical explosives detection: from color changes to fluorescence turn-on," Chemical Society Reviews **38**, 2543-2555 (2009).
19. M. Schaferling, "The art of fluorescence imaging with chemical sensors," Angew Chem Int Edit **51**, 3532-3554 (2012).

20. F. Vollmer, S. Arnold, D. Braun, I. Teraoka, and A. Libchaber, "Multiplexed DNA quanti. cation by spectroscopic shift of two microsphere cavities," Biophys J **85**, 1974-1979 (2003).
21. H. C. Ren, F. Vollmer, S. Arnold, and A. Libchaber, "High-Q microsphere biosensor - analysis for adsorption of rodlike bacteria," Opt Express **15**, 17410-17423 (2007).
22. N. M. Hanumegowda, C. J. Stica, B. C. Patel, I. White, and X. D. Fan, "Refractometric sensors based on microsphere resonators," Appl Phys Lett **87**, 3 (2005).
23. X. M. Zhang, and A. M. Armani, "Silica microtoroid resonator sensor with monolithically integrated waveguides," Opt Express **21**, 23592-23603 (2013).
24. A. M. Armani, R. P. Kulkarni, S. E. Fraser, R. C. Flagan, and K. J. Vahala, "Label-free, single-molecule detection with optical microcavities," Science **317**, 783-787 (2007).
25. R. W. Boyd, and J. E. Heebner, "Sensitive disk resonator photonic biosensor," Appl Optics **40**, 5742-5747 (2001).
26. S. Lee, S. C. Eom, J. S. Chang, C. Huh, G. Y. Sung, and J. H. Shin, "Label-free optical biosensing using a horizontal air-slot SiNx microdisk resonator," Opt Express **18**, 20638-20644 (2010).
27. M. Ostrowski, P. Pignalosa, H. Smith, and Y. Yi, "Higher-order optical resonance node detection of integrated disk microresonator," Opt Lett **36**, 3042-3044 (2011).
28. J. T. Robinson, L. Chen, and M. Lipson, "On-chip gas detection in silicon optical microcavities," Opt Express **16**, 4296-4301 (2008).
29. K. De Vos, J. Girones, S. Popelka, E. Schacht, R. Baets, and P. Bienstman, "SOI optical microring resonator with poly(ethylene glycol) polymer brush for label-free biosensor applications," Biosens Bioelectron **24**, 2528-2533 (2009).
30. M. Iqbal, M. A. Gleeson, B. Spaugh, F. Tybor, W. G. Gunn, M. Hochberg, T. Baehr-Jones, R. C. Bailey, and L. C. Gunn, "Label-Free Biosensor Arrays Based on Silicon Ring Resonators and High-Speed Optical Scanning Instrumentation," Ieee J Sel Top Quant **16**, 654-661 (2010).
31. D. X. Xu, M. Vachon, A. Densmore, R. Ma, A. Delage, S. Janz, J. Lapointe, Y. Li, G. Lopinski, D. Zhang, Q. Y. Liu, P. Cheben, and J. H. Schmid, "Label-free biosensor array based on silicon-on-insulator ring resonators addressed using a WDM approach," Opt Lett **35**, 2771-2773 (2010).
32. Z. Xia, H. Yi, Y. Chen, and Z. Zhou, "Sensitivity and detection limit of dual-waveguide coupled microring resonator biosensors," Chinese Optics Letters **7**, 598-600 (2009).
33. K. De Vos, I. Bartolozzi, E. Schacht, P. Bienstman, and R. Baets, "Silicon-on-Insulator microring resonator for sensitive and label-free biosensing," Opt Express **15**, 7610-7615 (2007).
34. C. Delezoide, M. Salsac, J. Lautru, H. Leh, C. Nogues, J. Zyss, M. Buckle, I. Ledoux-Rak, and C. T. Nguyen, "Vertically coupled polymer microracetrack resonators for label-free biochemical sensors," Ieee Photonic Tech L **24**, 270-272 (2012).
35. P. Dumon, W. Bogaerts, R. Baets, J. M. Fedeli, and L. Fulbert, "Towards foundry approach for silicon photonics: silicon photonics platform ePIXfab," Electron Lett **45**, 581-U582 (2009).

36. C. Qiu, J. Chen, and Q. Xu, "Ultraprecise measurement of resonance shift for sensing applications," Opt Lett **37**, 5012-5014 (2012).
37. M.-J. Banuls, R. Puchades, and A. Maquieira, "Chemical surface modifications for the development of silicon-based label-free integrated optical (IO) biosensors: A review," Anal Chim Acta **777**, 1-16 (2013).
38. O. Parriaux, and G. J. Veldhuis, "Normalized analysis for the sensitivity optimization of integrated optical evanescent-wave sensors," J Lightwave Technol **16**, 573-582 (1998).
39. C. F. Carlborg, K. B. Gylfason, A. Kazmierczak, F. Dortu, M. J. Banuls Polo, A. Maquieira Catala, G. M. Kresbach, H. Sohlstrom, T. Moh, L. Vivien, J. Popplewell, G. Ronan, C. A. Barrios, G. Stemme, and W. van der Wijngaart, "A packaged optical slot-waveguide ring resonator sensor array for multiplex label-free assays in labs-on-chips," Lab Chip **10**, 281-290 (2010).
40. T. Claes, J. Girones Molera, K. De Vos, E. Schacht, R. Baets, and P. Bienstman, "Label-free biosensing with a slot-waveguide-based ring resonator in silicon on insulator," Ieee Photonics J **1**, 197-204 (2009).
41. M. Mancuso, J. M. Goddard, and D. Erickson, "Nanoporous polymer ring resonators for biosensing," Opt Express **20**, 245-255 (2012).
42. G. Rong, A. Najmaie, J. E. Sipe, and S. M. Weiss, "Nanoscale porous silicon waveguide for label-free DNA sensing," Biosens. Bioelectron. **23**, 1572-1576 (2008).
43. M. M. Orosco, C. Pacholski, and M. J. Sailor, "Real-time monitoring of enzyme activity in a mesoporous silicon double layer," Nature Nanotechnology **4**, 255-258 (2009).
44. A. M. Rossi, L. Wang, V. Reipa, and T. E. Murphy, "Porous silicon biosensor for detection of viruses," Biosensors & bioelectronics **23**, 741-745 (2007).
45. S. Chan, S. R. Horner, P. M. Fauchet, and B. L. Miller, "Identification of gram negative bacteria using nanoscale silicon microcavities," Journal of the American Chemical Society **123**, 11797-11798 (2001).
46. P. A. Snow, E. K. Squire, P. S. J. Russell, and L. T. Canham, "Vapor sensing using the optical properties of porous silicon Bragg mirrors," J Appl Phys **86**, 1781-1784 (1999).
47. G. Korotcenkov, and B. K. Cho, "Silicon Porosification: State of the Art," Crit Rev Solid State **35**, 153-260 (2010).
48. J. W. Mares, X. Wei, and S. M. Weiss, "Porous materials for optical detection of chemicals, biological molecules, and high energy radiation," in *Photonic Microdevices/Microstructures for Sensing Iv*, X. Fan, H. Xiao, and A. Wang, eds. (2012).
49. J. J. Saarinen, S. M. Weiss, P. M. Fauchet, and J. E. Sipe, "Reflectance analysis of a multilayer one-dimensional porous silicon structure: Theory and experiment," J Appl Phys **104** (2008).
50. M. Ghulinyan, C. J. Oton, G. Bonetti, Z. Gaburro, and L. Pavesi, "Free-standing porous silicon single and multiple optical cavities," J Appl Phys **93**, 9724-9729 (2003).
51. K. A. Kilian, T. Boecking, and J. J. Gooding, "The importance of surface chemistry in mesoporous materials: lessons from porous silicon biosensors," Chemical Communications, 630-640 (2009).
52. P. J. Reece, G. Lerondel, W. H. Zheng, and M. Gal, "Optical microcavities with subnanometer linewidths based on porous silicon," Appl Phys Lett **81**, 4895-4897 (2002).

53. Z. Bao, M. R. Weatherspoon, S. Shian, Y. Cai, P. D. Graham, S. M. Allan, G. Ahmad, M. B. Dickerson, B. C. Church, Z. Kang, H. W. Abernathy, III, C. J. Summers, M. Liu, and K. H. Sandhage, "Chemical reduction of three-dimensional silica micro-assemblies into microporous silicon replicas," Nature **446**, 172-175 (2007).
54. M. S. Haluska, R. L. Snyder, K. H. Sandhage, and S. T. Misture, "Closed, heated reaction chamber design for dynamic high-temperature x-ray-diffraction analyses of gas/solid displacement reactions," Rev. Sci. Instrum. **76**, 4 (2005).
55. M. S. Haluska, I. C. Dragomir, K. H. Sandhage, and R. L. Snyder, "X-ray diffraction analyses of 3D MgO-based replicas of diatom microshells synthesized by a low-temperature gas/solid displacement reaction," Powder Diffr. **20**, 306-310 (2005).
56. V. Bertagna, R. Erre, M. L. Saboungi, S. Petitdidier, D. Levy, and A. Menelle, "Neutron reflectivity study of ultrathin SiO2 on Si," Appl Phys Lett **84**, 3816-3818 (2004).
57. O. Scheler, J. T. Kindt, A. J. Qavi, L. Kaplinski, B. Glynn, T. Barry, A. Kurg, and R. C. Bailey, "Label-free, multiplexed detection of bacterial tmRNA using silicon photonic microring resonators," Biosens Bioelectron **36**, 56-61 (2012).
58. K. De Vos, J. Girones, T. Claes, Y. De Koninck, S. Popelka, E. Schacht, R. Baets, and P. Bienstman, "Multiplexed Antibody Detection With an Array of Silicon-on-Insulator Microring Resonators," Ieee Photonics J **1**, 225-235 (2009).
59. A. L. Washburn, M. S. Luchansky, A. L. Bowman, and R. C. Bailey, "Quantitative, Label-Free Detection of Five Protein Biomarkers Using Multiplexed Arrays of Silicon Photonic Microring Resonators," Anal Chem **82**, 69-72 (2010).
60. B. Pejcic, P. Eadington, and A. Ross, "Environmental monitoring of hydrocarbons: A chemical sensor perspective," Environmental Science & Technology **41**, 6333-6342 (2007).
61. K. J. Albert, N. S. Lewis, C. L. Schauer, G. A. Sotzing, S. E. Stitzel, T. P. Vaid, and D. R. Walt, "Cross-reactive chemical sensor arrays," Chem Rev **100**, 2595-2626 (2000).
62. F. Roeck, N. Barsan, and U. Weimar, "Electronic nose: Current status and future trends," Chem Rev **108**, 705-725 (2008).
63. B. Adhikari, and S. Majumdar, "Polymers in sensor applications," Progress in Polymer Science **29**, 699-766 (2004).
64. N. Barsan, D. Koziej, and U. Weimar, "Metal oxide-based gas sensor research: How to?," Sensor Actuat B-Chem **121**, 18-35 (2007).
65. H.-J. Kim, and J.-H. Lee, "Highly sensitive and selective gas sensors using p-type oxide semiconductors: Overview," Sensor Actuat B-Chem **192**, 607-627 (2014).
66. N. Ramgir, N. Datta, M. Kaur, S. Kailasaganapathi, A. K. Debnath, D. K. Aswal, and S. K. Gupta, "Metal oxide nanowires for chemiresistive gas sensors: Issues, challenges and prospects," Colloids and Surfaces a-Physicochemical and Engineering Aspects **439**, 101-116 (2013).
67. B. Derby, "Inkjet Printing of Functional and Structural Materials: Fluid Property Requirements, Feature Stability, and Resolution," in *Annu Rev Mater Res*, D. R. Clarke, M. Ruhle, and F. Zok, eds. (2010), pp. 395-414.
68. T. Fukazawa, F. Ohno, and T. Baba, "Very compact arrayed-waveguide-grating demultiplexer using Si photonic wire waveguides," Japanese Journal of Applied Physics Part 2-Letters & Express Letters **43**, L673-L675 (2004).

69. K. Kodate, and Y. Komai, "Compact spectroscopic sensor using an arrayed waveguide grating," J. Opt. A-Pure Appl. Opt. **10**, 7 (2008).
70. F. Horst, W. M. J. Green, B. J. Offrein, and Y. A. Vlasov, "Silicon-on-Insulator Echelle Grating WDM Demultiplexers With Two Stigmatic Points," Ieee Photonic Tech L **21**, 1743-1745 (2009).
71. S. Janz, A. Balakrishnan, S. Charbonneau, P. Cheben, M. Cloutier, A. Delage, K. Dossou, L. Erickson, M. Gao, P. A. Krug, B. Lamontagne, M. Packirisamy, M. Pearson, and D. X. Xu, "Planar waveguide echelle gratings in silica-on-silicon," Ieee Photonic Tech L **16**, 503-505 (2004).
72. J. Song, and N. Zhu, "Design and fabrication of compact etched diffraction grating demultiplexers based on alpha-Si nanowire technology," Electron Lett, 43-45 (2009).
73. B. Momeni, M. Chamanzar, E. S. Hosseini, M. Askari, M. Soltani, and A. Adibi, "Strong angular dispersion using higher bands of planar silicon photonic crystals," Opt Express **16**, 14213-14220 (2008).
74. B. Momeni, E. S. Hosseini, M. Askari, M. Soltani, and A. Adibi, "Integrated photonic crystal spectrometers for sensing applications," Opt Commun **282**, 3168-3171 (2009).
75. B. B. C. Kyotoku, L. Chen, and M. Lipson, "Sub-nm resolution cavity enhanced microspectrometer," Opt Express **18**, 102-107 (2010).
76. R. F. Wolffenbuttel, "State-of-the-art in integrated optical microspectrometers," Ieee T Instrum Meas **53**, 197-202 (2004).
77. S.-W. Wang, C. Xia, X. Chen, W. Lu, M. Li, H. Wang, W. Zheng, and T. Zhang, "Concept of a high-resolution miniature spectrometer using an integrated filter array," Opt Lett **32**, 632-634 (2007).
78. M. Soltani, Q. Li, S. Yegnanarayanan, and A. Adibi, "Toward ultimate miniaturization of high Q silicon traveling-wave microresonators," Opt Express **18** (2010).
79. R. Liu, T. A. Schmedake, Y. Y. Li, M. J. Sailor, and Y. Fainman, "Novel porous silicon vapor sensor based on polarization interferometry," Sensor Actuat B-Chem **87**, 58-62 (2002).
80. Z. Xia, S. C. Davis, A. A. Eftekhar, A. S. Gordin, M. Askari, Q. Li, F. Ghasemi, K. H. Sandhage, and A. Adibi, "Magnesiothermically Formed Porous Silicon Thin Films on Silicon ‐ on ‐ Insulator Optical Microresonators for High ‐ Sensitivity Detection," Advanced Optical Materials **2**, 235-239 (2014).
81. R. K. Franks, and Robertso.Jb, "MAGNESIUM AS A DONOR IMPURITY IN SILICON," Solid State Communications **5**, 479-& (1967).
82. X. Wei, and S. M. Weiss, "Guided mode biosensor based on grating coupled porous silicon waveguide," Opt Express **19**, 11330-11339 (2011).
83. E. T. Vandenberg, L. Bertilsson, B. Liedberg, K. Uvdal, R. Erlandsson, H. Elwing, and I. Lundstrom, "Structure of 3-Aminopropyl Triethoxy Silane on Silicon-Oxide," J Colloid Interf Sci **147**, 103-118 (1991).
84. Y. Jiao, and S. M. Weiss, "Design parameters and sensitivity analysis of polymer-cladded porous silicon waveguides for small molecule detection," Biosensors & bioelectronics **25**, 1535-1538 (2010).

85. A. Yalcin, K. C. Popat, J. C. Aldridge, T. A. Desai, J. Hryniewicz, N. Chbouki, B. E. Little, O. King, V. Van, S. Chu, D. Gill, M. Anthes-Washburn, and M. S. Unlu, "Optical sensing of biomolecules using microring resonators," Ieee J Sel Top Quant **12**, 148-155 (2006).
86. J. L. Lawrie, J. Yang, and S. M. Weiss, "Size-Dependent Infiltration and Optical Detection of Nucleic Acids in Nanoscale Pores," Nanotechnology, IEEE Transactions on **9**, 596-602 (2010).
87. N. A. Yebo, P. Lommens, Z. Hens, and R. Baets, "An integrated optic ethanol vapor sensor based on a silicon-on-insulator microring resonator coated with a porous ZnO film," Opt Express **18**, 11859-11866 (2010).
88. F. Dell'Olio, and V. M. Passaro, "Optical sensing by optimized silicon slot waveguides," Opt Express **15**, 4977-4993 (2007).
89. A. Yin, M. Tzolov, D. Cardimona, L. Guo, and J. Xu, "Fabrication of highly ordered anodic aluminium oxide templates on silicon substrates," Iet Circ Device Syst **1**, 205-209 (2007).
90. A. Kisner, M. Heggen, W. Fischer, K. Tillmann, A. Offenhausser, L. T. Kubota, and Y. Mourzina, "In situ fabrication of ultrathin porous alumina and its application for nanopatterning Au nanocrystals on the surface of ion-sensitive field-effect transistors," Nanotechnology **23** (2012).
91. D. Crouse, Y. H. Lo, A. E. Miller, and M. Crouse, "Self-ordered pore structure of anodized aluminum on silicon and pattern transfer," Appl Phys Lett **76**, 49-51 (2000).
92. M. M. Braun, and L. Pilon, "Effective optical properties of non-absorbing nanoporous thin films," Thin Solid Films **496**, 505-514 (2006).
93. H. Zhang, Z. Jia, X. Lv, J. Zhou, L. Chen, R. Liu, and J. Ma, "Porous silicon optical microcavity biosensor on silicon-on-insulator wafer for sensitive DNA detection," Biosens Bioelectron **44**, 89-94 (2013).
94. K.-S. Mun, S. D. Alvarez, W.-Y. Choi, and M. J. Sailor, "A Stable, Label-free Optical Interferometric Biosensor Based on TiO2 Nanotube Arrays," Acs Nano **4**, 2070-2076 (2010).
95. X. M. Wang, J. Y. Zhang, F. Pan, W. C. Hao, and T. M. Wang, "Preparation and characterization of nanosized titania sensing film," Rare Metal Mat Eng **35**, 200-202 (2006).
96. P. Xiao, B. B. Garcia, Q. Guo, D. W. Liu, and G. Z. Cao, "TiO2 nanotube arrays fabricated by anodization in different electrolytes for biosensing," Electrochem Commun **9**, 2441-2447 (2007).
97. S. D. Alvarez, C.-P. Li, C. E. Chiang, I. K. Schuller, and M. J. Sailor, "A Label-Free Porous Alumina Interferometric Immunosensor," Acs Nano **3**, 3301-3307 (2009).
98. S. Pan, and L. J. Rothberg, "Interferometric Sensing of Biomolecular Binding Using Nanoporous Aluminum Oxide Templates," Nano Lett **3**, 811-814 (2003).
99. K.-P. S. Dancil, D. P. Greiner, and M. J. Sailor, "A Porous Silicon Optical Biosensor: Detection of Reversible Binding of IgG to a Protein A-Modified Surface," J Am Chem Soc **121**, 7925-7930 (1999).
100. Y. Paz, "Self-assembled monolayers and titanium dioxide: From surface patterning to potential applications," Beilstein Journal of Nanotechnology **2**, 845-861 (2011).

101. R. R. Unocic, F. M. Zalar, P. M. Sarosi, Y. Cai, and K. H. Sandhage, "Anatase assemblies from algae: coupling biological self-assembly of 3-D nanoparticle structures with synthetic reaction chemistry," Chem Commun, 796-797 (2004).
102. J. D. Berrigan, T. McLachlan, J. R. Deneault, Y. Cai, T.-S. Kang, M. F. Durstock, and K. H. Sandhage, "Conversion of porous anodic Al2O3 into freestanding, uniformly aligned, multi-wall TiO2 nanotube arrays for electrode applications," Journal of Materials Chemistry A **1**, 128-134 (2013).
103. Y. Jiang, D. Yang, L. Zhang, L. Li, Q. Sun, Y. Zhang, J. Li, and Z. Jiang, "Biomimetic synthesis of titania nanoparticles induced by protamine," Dalton transactions (Cambridge, England : 2003), 4165-4171 (2008).
104. Y. Fang, Q. Wu, M. B. Dickerson, Y. Cai, S. Shian, J. D. Berrigan, N. Poulsen, N. Kröger, and K. H. Sandhage, "Protein-Mediated Layer-by-Layer Syntheses of Freestanding Microscale Titania Structures with Biologically Assembled 3-D Morphologies," Chemistry of Materials **21**, 5704-5710 (2009).
105. G. Rong, and S. M. Weiss, "Biomolecule size-dependent sensitivity of porous silicon sensors," physica status solidi (a) **206**, 1365-1368 (2009).
106. Q. Li, A. A. Eftekhar, M. Sodagar, Z. Xia, A. H. Atabaki, and A. Adibi, "Vertical integration of high-Q silicon nitride microresonators into silicon-on-insulator platform," Opt Express **21**, 18236-18248 (2013).
107. "http://www.sigmaaldrich.com/."
108. K. Luke, A. Dutt, C. B. Poitras, and M. Lipson, "Overcoming Si3N4 film stress limitations for high quality factor ring resonators," Opt Express **21**, 22829-22833 (2013).
109. M.-C. Tien, J. F. Bauters, M. J. R. Heck, D. T. Spencer, D. J. Blumenthal, and J. E. Bowers, "Ultra-high quality factor planar Si3N4 ring resonators on Si substrates," Opt Express **19**, 13551-13556 (2011).
110. P. C. Jurs, G. A. Bakken, and H. E. McClelland, "Computational methods for the analysis of chemical sensor array data from volatile analytes," Chem Rev **100**, 2649-2678 (2000).
111. K. Reddy, Y. B. Guo, J. Liu, W. Lee, M. K. K. Oo, and X. D. Fan, "Rapid, sensitive, and multiplexed on-chip optical sensors for micro-gas chromatography," Lab Chip **12**, 901-905 (2012).
112. M. Soltani, Q. Li, S. Yegnanarayanan, and A. Adibi, "Toward ultimate miniaturization of high Q silicon traveling-wave microresonators," Opt Express **18**, 19541-19557 (2010).
113. Z. Xia, A. A. Eftekhar, M. Soltani, B. Momeni, Q. Li, M. Chamanzar, S. Yegnanarayanan, and A. Adibi, "High resolution on-chip spectroscopy based on miniaturized microdonut resonators," Opt Express **19**, 12356-12364 (2011).